2000-05-12

Determination of Average Lift of a Rapidly Pitching Airfoil

Anthony Blane Linn
Worcester Polytechnic Institute

DETERMINATION OF AVERAGE LIFT OF A RAPIDLY PITCHING AIRFOIL

By

Anthony Blane Linn

A Thesis

Submitted to the Faculty

of the

WORCESTER POLYTECHNIC INSTITUTE

In partial fulfillment of the requirements for the

Degree of Master of Science

in

Mechanical Engineering

October 1999

Approved:

Dr. William W. Durgin, Thesis Advisor, Dean of Graduate Studies

Dr. Hamid Johari

Dr. David J. Olinger

Dr. James C. Hermanson, Graduate Committee Representative

1 Exordium

Abstract

Dynamic stall characteristics of an NACA–0012 was investigated to assess the possibility of augmented lift during sinusoidal angle of attack motion. Tests were conducted over a range of Reynolds numbers from $2.0x10^5$ to $5.0x10^5$ and reduced frequencies from 0.02 to 0.3. The data were recorded and plotted in a series of lift coefficient vs. angle of attack diagrams. These diagrams exhibited a hysteresis curve for the dynamic stall cycle similar to the results of previous investigators but without a large peak at high angles of attack. The data were also plotted as lift coefficient vs. angular cycle position. The average lift coefficient was computed for each set of test conditions and plotted with average lift coefficient vs. reduced frequency for each value of Reynolds number. The summary data indicate an increase of average lift coefficient with increased reduced frequency, and increased Reynolds number, although the increase was not monotonic over either Reynolds Number or reduced frequency.

Exordium

Acknowledgements

I would like to thank all those who have helped me with this project. It has been a very long ordeal that has tested the patience of all of those involved. My special thanks go to Dean Durgin for his assistance and incredible patience during long delays. Todd Billings deserves special thanks for tolerating my presence in his shop space for over a year. My wife Valerie and children, Shannon and Eric deserve awards for patience and tolerance as well. Extra special thanks go to Valerie for her support and assistance and editorial skill.

Exordium

Table of Contents

Exordium

Exordium

Exordium

Exordium

Exordium

Exordium

Exordium

List of Figures

Exordium

Exordium

Exordium

List of Symbols

In the alphabetical order

AOA	angle of attack
AR	aspect ratio
C	Test section area
C	Chord of airfoil
c	Chord
h	Height of test section
k	Reduced frequency
K	Reduced pitch rate
L	Lift
q	Dynamic pressure
Re	Reynolds number
r	Radius
S	Wing planform area
u	Free-stream velocity scalar
v	Velocity scalar, blade element
V	Free-stream velocity vector
α	Angle of attack
δ	Boundary layer thickness
Γ	Circulation
μ	Viscosity
ρ	Density
v	Kinematic viscosity

Exordium

List of symbols continued.

ω	Angular velocity
A_{L}	Lift augmentation factor
c_{du}	Uncorrected drag coefficient
C_{l}	Steady state lift coefficient
C_{lavg}	Average lift coefficient
$C_{l\max}$	Max steady state lift coefficient
c_{lu}	Uncorrected lift coefficient
$c_{m1/4u}$	Uncorrected moment coefficient at _ chord
K_1	Constant for solid blockage
m_0	Slope of lift section curve
M_∞	Free stream Mach number
V_∞	Free-stream velocity scalar
α_0	Initial angle of attack, dynamic
α_{avg}	Average angle of attack, dynamic
$\alpha_{\max}$	Max angle of attack, dynamic
α_u	Uncorrected angle of attack
δ_2	Momentum boundary layer
	Total blockage correction factor
$_{sb}$	Solid blockage correction factor
$_{wb}$	Wake blockage correction factor

Exordium

List of Photo Images

2 Dynamic Stall

Introduction

Interest in the effects of dynamic stall is widespread. Dynamic stall can occur in devices such as aircraft and turbomachinery. Dynamic flow effects are vastly different from their steady flow counterparts and can cause performance vastly different than that predicted by steady-state airfoil data.

Dynamic stall is a phenomenon where the lift produced by an airfoil during a rapid increase in angle of attack significantly exceeds the lift of an airfoil subject to steady angle of attack conditions. W.S. Farren,[1] in England, first measured this phenomenon in 1933, confirming the suspicions of many aerodynamicists. Further study has been conducted mostly since the early 1970's. The experiment, which is the subject of this paper, is closely related to the work of Graham and Islam,[2] and the work of McAlister[3]. G. M. Graham and M. Islam, evaluated the average lift of an NACA 0012 airfoil subjected to a periodic "triangular wave" angle of attack trajectory in an experiment conducted in 1990. McAlister, examined the lift coefficient versus angle of attack (AOA) curves for an NACA 0012 airfoil subject to sinusoidal AOA oscillation in an experiment conducted in 1978.

Dynamic Stall

The objective of the tests conducted in this project was to determine if an airfoil subject to a sinusoidal angle of attack (AOA) trajectory would demonstrate an increase or decrease of time averaged lift, when compared to the same airfoil subject to steady state conditions. Tests were conducted on a NACA 0012 section, throughout an array of Reynolds Numbers and reduced frequencies. Each data point in the array was then evaluated and compared with the performance of the same airfoil at static lift conditions.

The apparatus provides for sinusoidal AOA motion of the airfoil using a crank and linkage. One end of the linkage was attached to the crank pin and the other end was attached to the perimeter of a rotating window. The rotating window supported one end of the airfoil and a stationary window supported the other end of the airfoil. This arrangement permitted flow observations during testing using smoke or other visualization means. The airfoil lift was determined from measurements of static pressure at the tunnel walls. This type of lift instrumentation allowed the airfoil being tested to be free of any pressure ports or internal plumbing. This also allowed the airfoil to be unencumbered by wires or tubes that normally would be connected to external pressure transducers. Further it allowed multiple airfoil shapes to be machined as solid sections, and tested

without changing the instrumentation from test to test, thus allowing a direct comparison of test results.

Objective of the experiment

The objective of this experiment was to determine if an airfoil subject to a sinusoidal angle of attack (AOA) trajectory would demonstrate an increase in time averaged lift, when compared to the same airfoil subject to steady state conditions.

Background

The phenomenon of Dynamic Stall

Stall, in the aerodynamic sense, is the loss of airfoil lift. This occurs because of flow separation over the airfoil as a result of high angles of attack. The mechanism of stall is best understood by first understanding the mechanism of lift in steady state conditions.

Dynamic Stall

Circulation, Lift and the Kutta Joukowski Theorem (Steady State)

Circulation may be illustrated with the aid of the diagram below. Each infinitesimal element ***dl*** along the curve C is a vector of magnitude dl and direction tangent to the curve C.

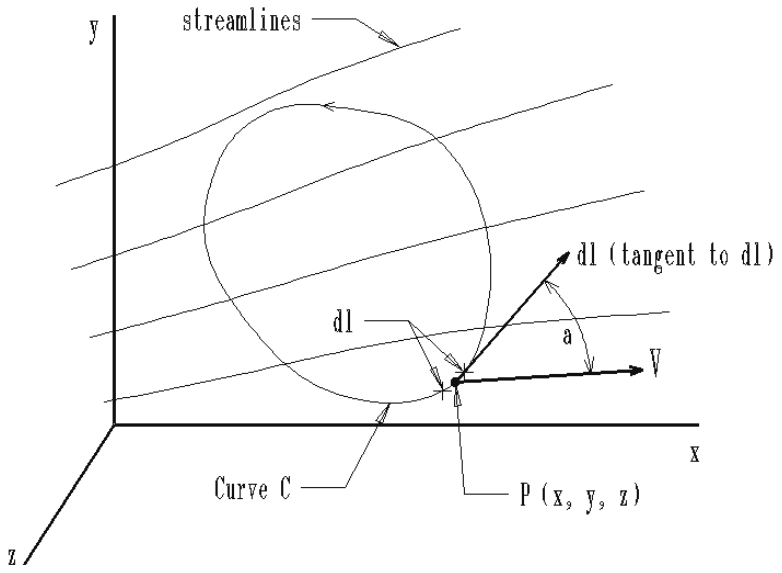

Figure 1, Circulation diagram

Circulation Γ is defined as the line integral of the scalar product $V \cdot dl$ around the closed curve C:

$$\Gamma \equiv \oint_C V \cdot dl \quad .$$

If circulation about an airfoil is being evaluated, curve C may be selected over any arbitrary path that encloses the airfoil and does not pass through a solid boundary such as a wind tunnel wall.

Dynamic Stall

The Kutta-Joukowski theorem states that the force exerted on a body subject to a uniform stream of fluid is equal to the product of the stream velocity, the circulation and the fluid density and is perpendicular to the flow direction. Hence lift per unit span L, can be expressed as:

$$L = \rho V \Gamma \quad .$$

The Kutta condition

The Kutta-Joukowski Theorem (KJT) describes lift as a result of flow about an arbitrary shape. All that is required to create lift, is flow about a body, and circulation. However, the KJT does not provide a means to determine the circulation when the boundaries of the body and the flow velocity are specified. The Kutta condition overcomes this problem. The Kutta condition comes from an empirical observation of flow about bodies with sharp trailing edges.[4] Experiments show that for flow about a body with a sharp trailing edge, the rear stagnation point will move to the trailing edge shortly after steady flow is attained. This phenomenon sets a value for the circulation about the airfoil. The Kutta condition may be stated as follows:

A body with a sharp trailing edge, which is moving through a fluid, will create about itself a circulation of sufficient strength to hold the rear stagnation point at the trailing edge.[5]

Dynamic Stall

The effect of circulation on flow about an airfoil can be illustrated by examining the following diagrams.[6] Flow about an airfoil without circulation is shown in Fig. 2.

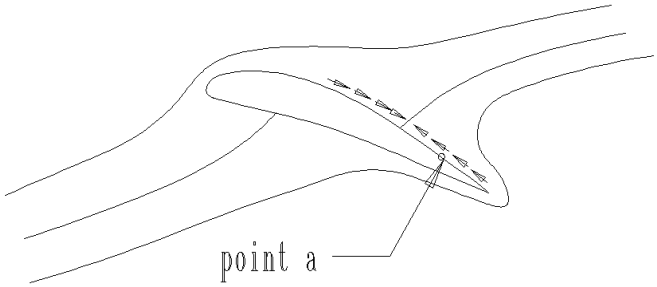

Figure 2, Airfoil without circulation, point *a* shown rearward of stagnation point.

If the flow velocity is measured at point '*a*' in the above figure, then a pure circulation is placed about the same airfoil with a strength sufficient to provide a velocity at '*a*' exactly opposite the value for flow resulting from flow past the airfoil in Fig. 3.

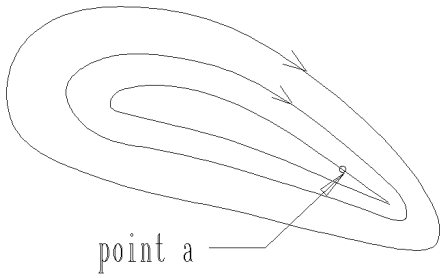

Figure 3, Airfoil with circulation only, providing velocity at '*a*' opposite that shown in figure 2 above.

Dynamic Stall

Superimposing the circulation flow (Fig. 3) onto the flow past the airfoil (Fig. 2) the velocity at point '*a*' will be zero. Therefore point '*a*' becomes the stagnation point. The addition of circulation has moved the stagnation point toward the trailing edge.

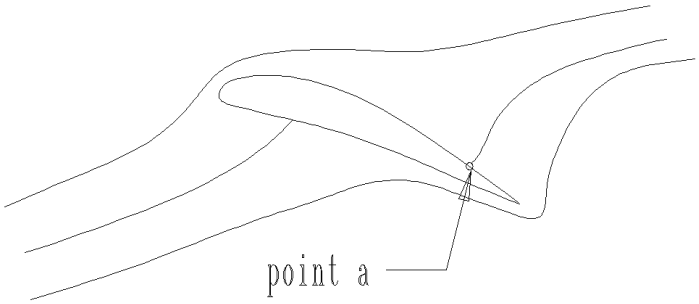

Figure 4, Airfoil with stagnation point relocated to point *a.*

It is apparent that a value of circulation exists that will move the stagnation point to the trailing edge of the airfoil. According to the Kutta condition this value is unique.

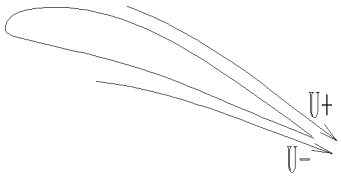

Figure 5, Airfoil trailing edge where u+ = u-

Another way to illustrate the Kutta condition is to consider the condition where the stagnation point does not occur at the trailing edge. See Fig. 5 above. This

then implies flow in opposite directions at the trailing edge. If it is assumed that there cannot be a discontinuity in flow at the trailing edge then the Kutta condition is satisfied.

Stalls

Steady state stalls

Steady state stall is the form of stall that is most familiar to aviators. This occurs when the AOA gradually exceeds the critical AOA for the airfoil. At this point the flow about the airfoil described above no longer follows the contour of the airfoil surface but separates from the surface causing circulation to diminish and lift to dramatically decrease. The mechanism of this type of stall is discussed further in the section 3.

Dynamic stalls:

Dynamic stall occurs during a rapid increase in AOA that extends beyond the critical AOA. The overall effect of dynamic stall is to extend the lift producing range of the airfoil beyond the critical angle of attack. Lift coefficients of 150%-200% of static lift coefficients are realized. Also present is a dramatic fluctuation in pitching moment. These effects are short lived since the flow that supports this level of lift coefficient breaks down very quickly. Airfoils subject to dynamic lift

due to sinusoidal oscillation are exposed to high AOA only briefly. Further discussion of the mechanism of dynamic stall is discussed in section 3.

Related work:

Early work done by W. S. Farren[1], 1933

In the 1930's, aerodynamicists in Great Britain suspected that airfoils were capable of lift in excess of that measured in static wind tunnel testing. Aircraft landing tests had indicated more than expected lift during rapid nose up maneuvers.

In 1935 W. S. Farren[1] constructed an experimental apparatus to measure the effects of dynamic stall. This device was a very sensitive mechanical force balance with a high natural frequency. Force data was recorded on photographic paper by reflecting a beam of light off of a small mirror attached to a spring supporting the airfoil. This mechanical arrangement had excellent dynamic sensitivity due to the low mass of the mirror spring assembly. The balance was able to record force data both normal to and parallel to the centerline of the tunnel, therefore providing both lift and drag data.

Dynamic Stall

Farren was able to obtain data that exhibited the dramatic increase in lift coefficient that is characteristic of the dynamic stall phenomenon. His tests included evaluations of the dynamic behavior of a number of airfoil sections that were in use during the 1930's in Great Britain. Although Farren was reluctant to claim that the dynamic stall effect was necessarily applicable to full-scale aircraft, his work spurred interest by a number of other research agencies to carry forward with other aspects of dynamic stall.

Additional work was done by a number of investigators conclusively demonstrating the nature of dynamic stall. The use of dynamic stall to augment lift was a logical extension of this work.

Work done by G. M. Graham and M. Islam[2] (1990)

Graham and Islam conducted an experiment that utilized the increased coefficient of lift resulting from dynamic stall. In this experiment they simulated an airfoil in forward flight as it would function as part of an "augmented lift vehicle" (ALV). The ALV had a wing pivoted at the fuselage that allowed rapid changes in AOA while the attitude of the fuselage remained constant. The ALV wing was pivoted at the _ chord point. The AOA trajectory was a linear increase in AOA followed by an immediate linear decrease in AOA, essentially a triangular waveform. The assumption was that the ALV wing could be reduced in size compared to the wing

Dynamic Stall

of a conventional vehicle (CV) because of the increased average lift coefficient. Both the ALV and CV wings were assumed to be NACA 0012 sections, and the following relationship for wings of finite span was used for sizing the wings of the ALV:

$$\frac{A_l C_{L\max} q S_{ALV}}{(1 + m_0 / \pi AR_{ALV})} = \frac{0.8 C_{L\max} q S_{CV}}{(1 + m_0 / \pi AR_{CV})}$$

where: C_L = maximum steady state lift coefficient

q = is the dynamic pressure

S = is the wing planform area

m_0 = is the slope of the section lift curve

AR = is the aspect ratio .

The constant of 0.8 on the right side of the above expression is included because the CV utilized only 80% of the maximum static lift.

Graham and Islam defined average lift as:

$$C_{Lavg} = \frac{1}{\tau_2 - \tau_1} \int_{\tau_1}^{\tau_2} C_L(\xi) d\xi$$

where ξ is time.

And defined the "dynamic augmentation factor" A_L as:

Dynamic Stall

$$A_L = \frac{C_{Lavg}}{C_{L\max}} \ .$$

Tests were conducted at pitch rates of K = 0.05, 0.1, and 0.2, where:

$$K = \dot{\alpha} C / 2U_\infty \ .$$

The initial angle of attack α_0, was evaluated at 0 degrees and 10 degrees and the max angle of attack $\alpha_{\max}$, was evaluated at 15 degrees through 65 degrees.

Their experiment demonstrated that the ALV could expect to have an A_L of 1.5. A mission analysis of the ALV with an A_L of 1.5 indicated a probable range increase of 20% for a flight vehicle employing lift augmentation. This was because a smaller wing could be used which provided reduced drag in cruise flight.

The Graham & Islam experiment was conducted in a tow tank, using a NACA 0012 airfoil with a 6-inch chord. The tank was 30 ft. long, 12 ft, wide and 4 ft. deep. The airfoil was moved in pitch by a stepper motor controlled by a computer.

Dynamic Stall

Work of McCroskey et al.[7] (1976)

McCroskey et al investigated unsteady lift and dynamic stall of an NACA-0012 airfoil subject to large sinusoidal oscillations in pitch. The basic NACA-0012 airfoil along with several leading edge variations was tested. The experiment instrumentation included hot wire measurements, pressure taps, and flow visualization with oil smoke. The leading edge variations included a larger leading edge radius, smaller leading edge radius, an ONERA leading edge which is a drooped leading edge form and a leading edge boundary layer trip in the from of a serrated strip. All of these modifications were made to the basic NACA-0012 section. From this work McCroskey et al. were able to identify three mechanisms for the onset of dynamic stall. The mechanisms were; 1) Trailing edge stall, where flow reversal started at the trailing-edge and progressed forward until complete flow breakdown occurred. 2) Leading-edge stall caused by an abrupt breakdown of flow at the leading edge followed by a flow reversal starting from the trailing edge and moving forward. And 3) two forms of leading edge stall which occurred due to the leading edge laminar separation bubble bursting, or due to the leading edge laminar separation bubble becoming a turbulent bubble and reattaching, then failing to reattach. The leading edge bubble bursting was discovered to be a special case. Regardless of the type of separation the overall results are essentially the same. A large vortex is generated at the leading edge

and is shed from the airfoil causing dramatic increases in lift coefficient and pitching moment.

Work of McAlister et al.[3] 1978:

McAlister et al. continued the work described above, in an experiment concentrating on the NACA-0012 airfoil at a single Reynolds number of $2.5x10^6$ and at Mach 0.09. Only two modifications to the leading edge, a boundary layer trip and a serrated leading edge strip. Instrumentation was similar to the previous experiment. Tests were conducted over a wide range of reduced frequencies, mean angle of attack and amplitudes. From these tests McAlister concluded that under the conditions tested the leading edge bubble had little or no direct effect on the stall process and could be seen to remain even after the onset of suction collapse over the leading edge region. Pressure measurements at the leading edge were sufficient to determine the presence and severity of moment stall. The strength of the stall vortex seemed dependant on the strength of the circulation on the airfoil at the time the vortex is formed. A definite sequence of stall events was determined to be; 1) a positive surge in normal force, 2) negative moment growth, 3) maximum negative chord force, 4) maximum leading edge suction, 5) suction wave appears, 6) negative roll-off in pitching moment, 7) maximum normal force. 8) maximum negative pitching moment.

Dynamic Stall

Work of McCroskey et al.[8] 1982

McCroskey et all conducted an experiment with apparatus similar to the above experiment but including eight airfoils over a wide range of Reynolds numbers, reduced frequencies and amplitudes. The airfoils selected were representative of the airfoils used by a number of helicopter manufacturers. The NACA-0012 airfoil was selected as a standard reference and a fixed wing supercritical airfoil as a reference to dynamic tests done in other tunnels. Flow conditions were Reynolds numbers up to $4x10^6$ and Mach numbers up to 0.30. The objectives of the experiment were to provide a set of standard dynamic information for modern rotor blade sections, to provide data for the dynamic performance of sections subject to roughness due to erosion or icing, and to provide a means of determining the dynamic performance of future airfoil designs. This experiment was very broad in scope covering some 600 different tests. From these tests McCroskey concluded that although the proprietary airfoils provided improved performance over the NACA-0012 section, the primary factors affecting airfoil behavior were the flow conditions leading up to dynamic stall. In many cases the data from different proprietary airfoils were indistinguishable after tunnel uncertainties were taken into account. The mechanism of dynamic stall remained as described above.

Dynamic Stall

Discussion of devices affected by Dynamic Lift

The airfoils of some aircraft components are regularly subject to rapid periodic changes of AOA while operating in specific regions of the aircraft operating envelop. Helicopter rotors that are heavily loaded and at high forward speeds may experience these effects. Similarly, the propellers on airplanes flying at very high attitudes or aircraft that employ tilting rotors or propellers may be subject to the effects of dynamic stall. The potential for dynamic stall is common to all of these devices because flow enters the rotor or propeller at an angle to the axis of rotation. The airfoil is subject to a change in relative direction of free stream flow as it rotates about its axis. In fig. 6a below, free stream flow enters the rotor parallel to the axis of rotation, dynamic effects will not be present. In Fig. 6b flow is inclined to the axis of rotation. Figure 6c depicts a blade element on the farside of the rotor in Fig. 6b where the effect is to decrease the relative velocity at the airfoil. Figure 6d depicts a blade element on the nearside of the rotor where the effect is to increase the relative velocity.

Dynamic Stall

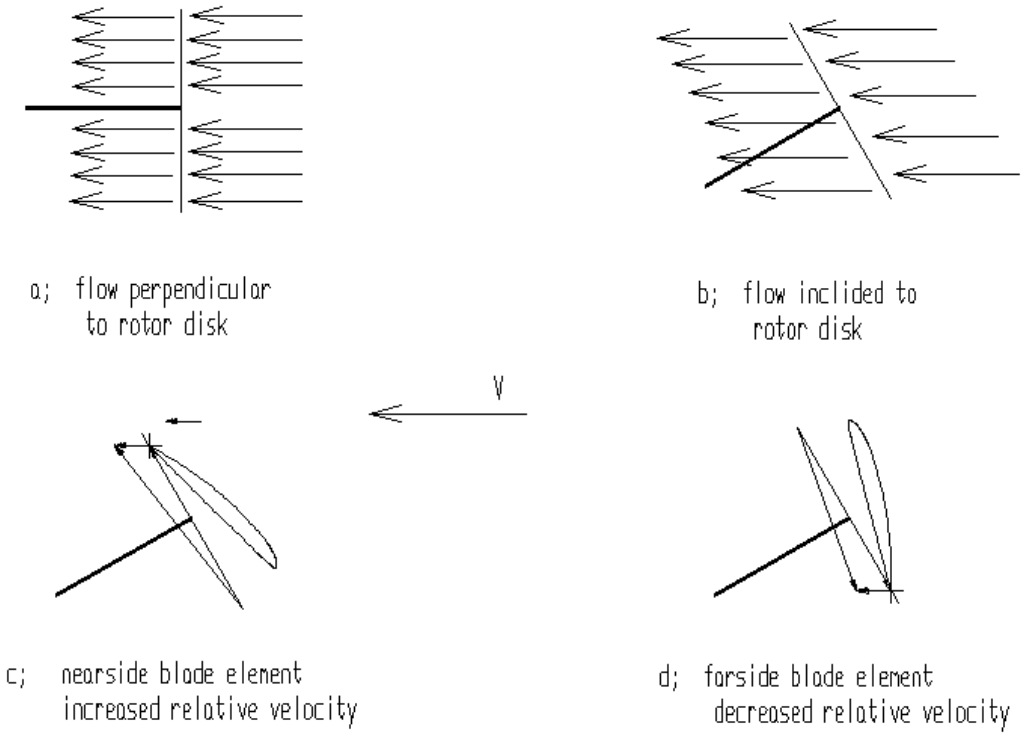

Figure 6, Rotors and propellers a, b, c, d

In this example the changes in AOA are periodic and approach sinusoidal motion. The most dramatic example sinusoidal AOA variation is the helicopter rotor in forward flight, which is discussed below.

Dynamic Stall

Helicopter rotor

The helicopter rotor develops lift by changing the momentum of the air moving downward through the rotor. In hovering flight the flow from above the rotor is induced and is axisymmetric to the rotor plane.

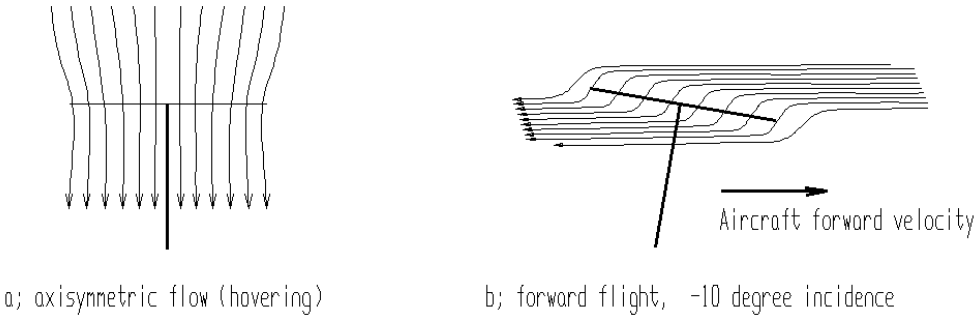

Figure 7, Helicopter rotor, axisymmetric flow (hovering) a, forward flight b

As the helicopter moves in forward flight the flow through the rotor is changed by the presence of the free stream flow superimposed on the induced flow. The resultant flow is inclined to the plane of the rotor. Induced flow, which is flow through the rotor, becomes very small in forward flight. In forward flight the helicopter flies with the rotor tip path plane at a negative AOA. The AOA is the angle at which flow enters the tip path plane of the rotor. The AOA of the tip path plane is independent of the AOA of the blades of that make up the rotor.

Dynamic Stall

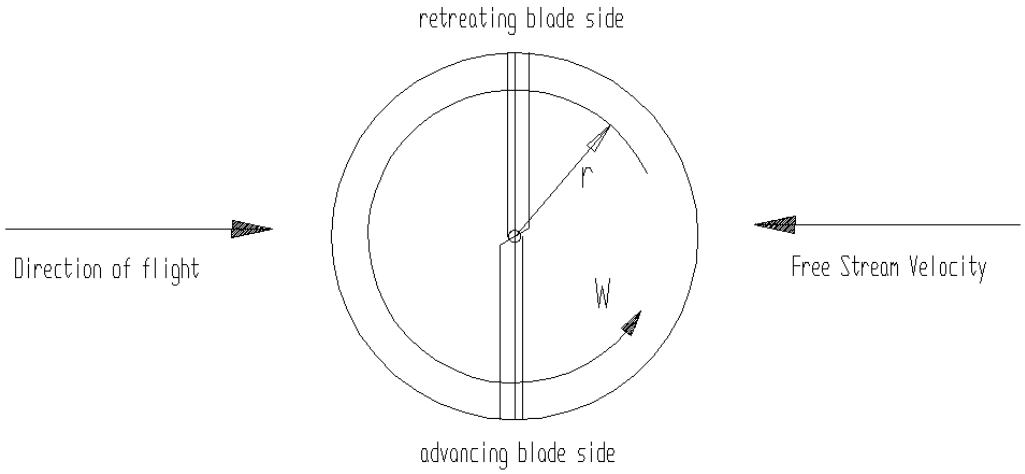

Figure 8, Plan view of rotor

Forward flight effects the aerodynamics of the rotor, causing asymmetrical rotor effects. The portion of the rotor moving in the direction of flight (advancing blade) is subject to the flow caused by rotor rotation summed with the flow caused by forward flight.

$$v = r(w) + u$$

The portion of the rotor moving opposite the direction of flight (retreating blade) is subject to the flow caused by rotor rotation less the flow caused by forward flight.

$$v = r(w) - u$$

The difference in relative velocity increases the lift generated on the advancing blade side of the rotor and decreases the lift generated on the retreating blade side. If this were not corrected the helicopter would roll toward the retreating blade side of the rotor (and crash). Cyclic pitch is used to correct the difference in lift

by changing the pitch of the rotor blade as it rotates. The cyclic pitch mechanism sinusoidally varies the pitch or AOA of the individual blades of the rotor as they rotate, increasing the pitch of each blade as it moves over the retreating blade region and decreasing the pitch of the blade as it moves over the advancing blade region. As the speed of forward flight increases the difference in blade pitch between the advancing and retreating blade regions of the rotor increases.

Figures 9 & 10 below show the blade angle of attack distribution for rotor in forward flight. In figure 9 & 10 the blank circle in the center of the rotor is the rotor hub. The shaded region near the center is the region where blades are exposed to reverse flow. Lines of equal AOA or iso-alpha lines are plotted throughout the remaining region of the rotor. In figure 9, iso-alpha lines are plotted for a rotor with twisted blades. In figure 10, iso-alpha lines are plotted for a rotor with blades without twist. Both figures show significantly higher blade AOA distributions on the retreating blade side than on the advancing blade side of the rotor.

Dynamic Stall

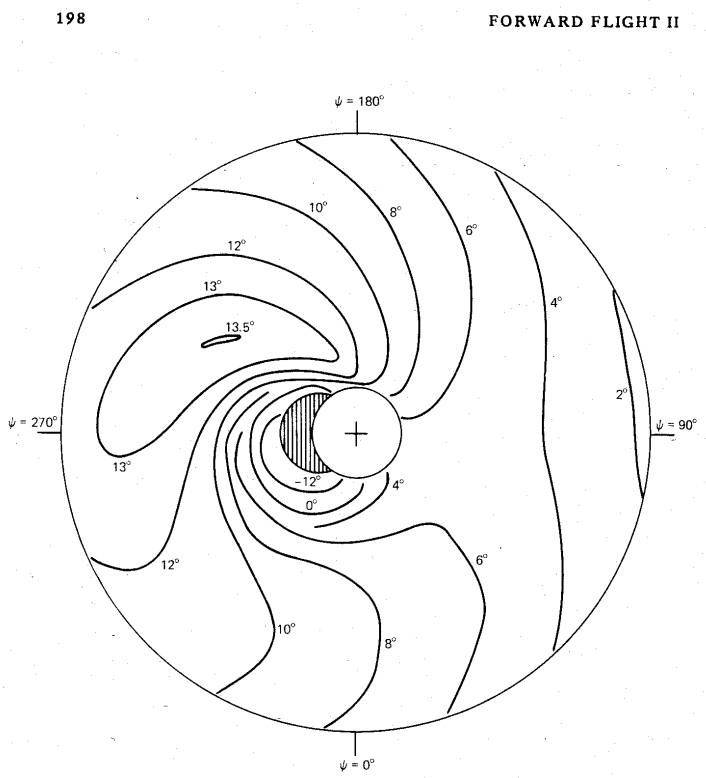

Figure 5.20 Blade angle-of-attack distribution (in degrees) at $\mu = 0.25$, for $C_T/\sigma = 0.12$, $f/A = 0.015$, and $\theta_{tw} = -8°$ (uniform inflow).

Figure 9, Blade angle of attack distribution for rotor with twisted blades in forward flight[9]

Dynamic Stall

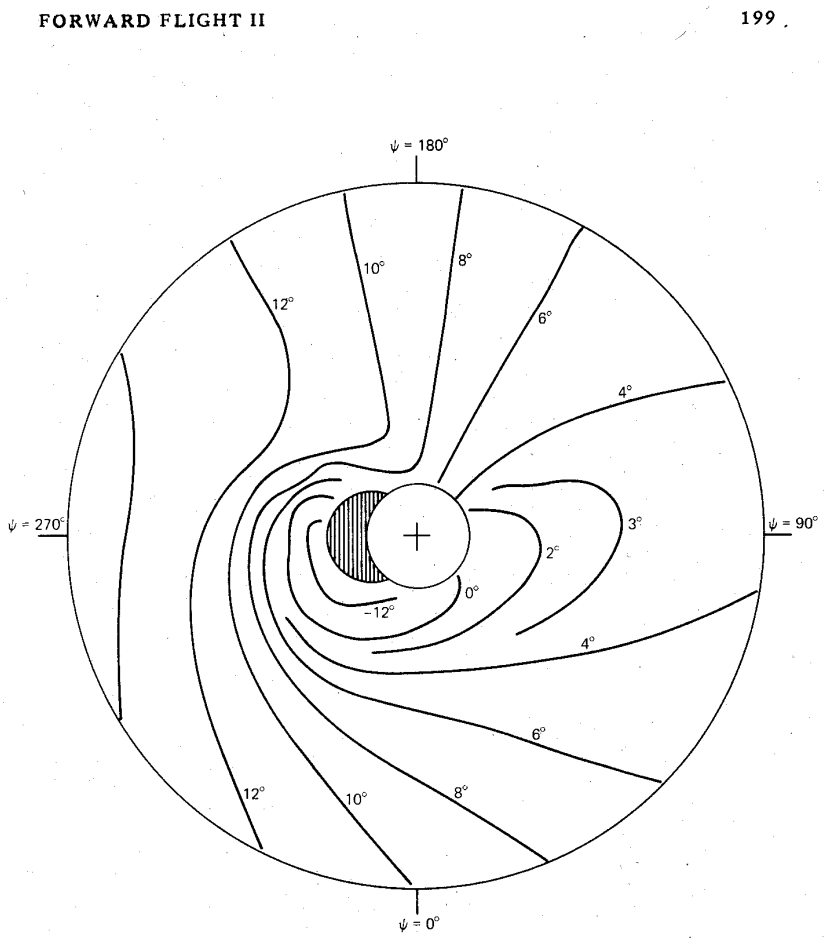

Figure 5.21 Blade angle-of-attack distribution (in degrees) at $\mu = 0.25$, for $C_T/\sigma = 0.12$, $f/A = 0.015$, and $\theta_{tw} = 0°$ uniform inflow).

Figure 10, Blade angle of attack distribution for rotor with untwisted blades in forward flight [9]

In figure 9, the rotor with twisted blades has a blade AOA distribution that exceeds 13 degrees over a portion of the retreating blade side of the rotor. The rotor with untwisted blades, in figure 10, has a very large region with a blade AOA in excess of 13 degrees. These regions of the rotor will experience dynamic

stall effects. As the rotor is more heavily loaded or the aircraft flies faster the area of the rotor subject to dynamic effects will increase.

Factors effecting dynamic stall

The analysis of dynamic stall is complicated by the large number of parameters that effect the phenomenon. McCroskey[10] summarized these factors which are discussed below:

Airfoil shape

Research of dynamic stall has been motivated mostly by the desire to improve helicopter performance. Most helicopter manufacturers design their own airfoils and therefore a relatively large number of airfoils have been available for comparison of dynamic stall effects. Considerable testing has been done on this group of airfoils normally used in helicopter rotor blades. In some cases experiments involving leading edge modifications have been successful in changing dynamic stall characteristics but not consistently. The most common airfoil specimen has been the NACA 0012 airfoil. The NACA 0012 is not a good airfoil for helicopter rotor use; however, tests conducted on this profile provide data that can be compared to other work.

Dynamic Stall

Mach Number

Mach number seems to have limited effects below $M_\infty \approx 0.2$:. The effects become more significant above $M_\infty \approx 0.2$.

Reynolds Number

The effects of Reynolds number are believed to be small at low Mach numbers, and unknown for high Mach numbers.

Reduced frequency

The effect of reduced frequency is predominant. Reduced frequency may have full control over dynamic stall if all other parameters are correct. At very low reduced frequencies, i.e. approaching steady state, dynamic effects disappear. Increasing the reduced frequency monotonically increases the effects of dynamic stall throughout the values tested to date.

Average Angle of Attack and amplitude of motion

Dynamic stall does not exist at angles of attack below the critical angle of attack. The average angle of attack and the amplitude of motion combined must cause the airfoil to exceed the critical angle of attack before dynamic stall effects are encountered. Generally the critical angle of attack must be exceeded by approximately a factor of two or more in order to reach the maximum attainable lift coefficient.

Dynamic Stall

Type of motion, angle of attack trajectory

The effects of dynamic stall are not restricted to sinusoidal angle of attack trajectories. The augmented lift vehicle (ALV) mentioned above used a linear increase in angle of attack followed by a linear decrease in angle of attack to produce dynamic lift effects. To date the effects of different types of motion have not been fully explored.

Origins of lift measurement technique

The lift measurement technique used in this experiment was first used by the NACA to make static lift measurements. With the advent of modern high-speed data acquisition equipment and very sensitive piezoresistive pressure transducers the technique can be used to measure dynamic lift characteristics.

In 1929, the then National Advisory Committee for Aeronautics[11] (NACA) set out to create and test a series of airfoils based on standardized features such as leading edge radius, thickness distribution, thickness/chord ratio as well as a series of mean camber lines and profiles.

These tests originally were done in general purpose facilities used to test scale aircraft, or components of aircraft such as semi-spans etc. Research showed that the performance of three-dimensional wings could be determined with the proper application of two dimensional airfoil section test data. Since two-dimensional

models were easier to construct and provided a more consistent means of comparison of airfoil performance a decision was made to develop a two dimensional test facility. The final facility completed about 1939 is known as the Langley Two-Dimensional Low Turbulence Pressure Tunnel[12]. This facility has a test section of 7.5 feet in height, 7.5 feet in length and 3 feet in width. The tunnel was constructed from heavy steel plate and was capable of being pressurized to 10 atmospheres or pulled down to near vacuum. The tunnel was capable of dynamic pressures in the order of 400-lb. force per square foot. Pressurization allowed adjustment of the air density, thus allowing greater control over Reynolds number, permitting manageable sized models to be used for testing full-scale conditions.

Models were almost exclusively supported by the tunnel walls. Models would span the test section, across the 3-foot dimension. The ends of the model were supported on pivots, which allow adjustment of the angle of attack and measurement of pitching moment. Lift was determined by measuring the pressure distribution on the floor and ceiling of the tunnel and then integrating the pressures. Drag was evaluated similarly, by measuring the pressure distribution of the model's wake and integrating the values. The wake rake is a relatively common device which is well understood, however, the lift measurement technique my need some explanation. Theoretically the pressure field

surrounding the airfoil extends to infinity both upstream and downstream. Obviously practical measurements are not made very far beyond the length of the test section. In the case of the Langley tunnel, pressure ports in the floor and ceiling extended over a length of 13 feet. A further discussion of the determination of lift by measurement of tunnel wall pressures is covered in section 3 Theory.

Actual integration of the pressure profile on the floor and ceiling of the tunnel was done using an integrating manometer.[12] This device and its principle of operation is described in appendix J

Rational for measuring lift by tunnel wall pressure distribution

Other factors than those stated in the introduction contributed to the decision to use tunnel wall pressure measurement s for lift determination. The airfoil was to be oscillated at frequencies up to 60 Hz. This presented the problem of de-coupling the acceleration forces from the lift forces if the airfoil lift were to be measured by force transducers at the airfoil pivot supports. If lift were measured using pressure taps on the surface of the airfoil connected to transducers with tubing, the required length of tubing to reach from the airfoil surface to the pressure transducers would preclude measurements at the rate required. Putting the transducers in the airfoil could solve the dynamics problem of measurement

but exposes the transducers to severe accelerations. The acceleration sensitivity of the transducers was not known. Furthermore, the wiring that would be required to reach the transducers would be susceptible to continuous damage and fatigue. Measuring lift from the tunnel walls has sidestepped all of these problems.

3 Theory

Kutta condition

Single Burbling Theory[13]

Polish aerodynamicist C. Witoszynski investigated the potential flow about a circle, i.e. 2D flow. In his investigation he began with the stream function for flow about a circle and then transformed the free-stream flow to be incident with a circle at a negative angle, simulating the angle of attack of an airfoil. When this transformed stream function was then again transformed to represent flow about an airfoil, a stream function similar to Fig. 4 resulted. The solution indicated an infinite velocity at the trailing edge, which of course could not exist. Experimental measurements had indicated that velocities just above and below the trailing edge, u+ and u-, (see Fig. 5,) were not necessarily the same. Motivated by this information Witoszynski developed a complimentary term for the above stream function complex potential to account for this discrepancy. This resulting function when evaluated for $\Psi = 0$ provided solutions for an incoming streamline and associated stagnation point and of course the basic circle. The function required that it be evaluated in the interval approaching the downstream stagnation point either over the top of the circle or around underneath the circle. These two intervals provide different solutions for the downstream streamline. Essentially saying that there are two downstream streamlines with different

velocity potentials and that the area between the streamlines did not have a unique solution.

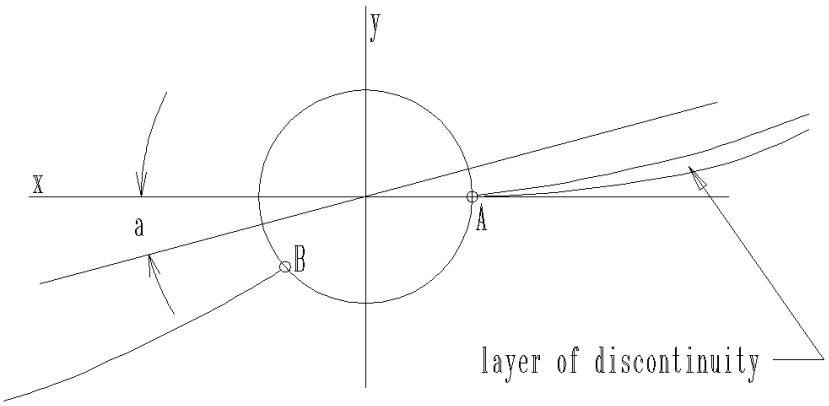

Figure 11, Single burbling theory

The downstream streamlines are coincident only at the primitive circle i. e. at the stagnation point and again at infinity. This suggests that the Kutta condition described above may only be a mathematical convenience.

The unsteady Kutta condition

Sears[14 15] reviewed the airfoil with sharp trailing edge and included the effects of boundary layers and unsteady flow on trailing edge vorticity and circulation. Contributing to the vorticity at the trailing edge is the vorticity from the upper and lower viscous boundary layers, which shed vorticity of opposite values. The rate of vortex shedding from the airfoil is related to the rate of change of circulation. The Kutta Joukowski Theorem may be restated: the pressure above and below the trailing edge must be equal. In the absence of wake shed vortices, the vortex at

the trailing edge must vanish, however, in the presence of a wake sheet, the strength of the airfoil and wake vortices must be equal at the trailing edge. If the vortex strengths are unequal then infinitely large velocities occur at the trailing edge. Although the strength of the trailing edge vorticity is not necessarily zero, the pressures on the top and bottom of the trailing edge remain equal because of the contributions of the velocity potential $\rho\partial\phi/\partial t$. The relationship between velocity potential and circulation is[14]

$$\left(\frac{\partial\phi}{\partial t}\right)_1 - \left(\frac{\partial\phi}{\partial t}\right)_2 = \frac{d\Gamma}{dt},$$

where the subscripts 1 and 2 denote upper and lower surfaces.

The strength of the bound vortex sheet represents the airfoil plus its boundary layers, and the shed vortex wake represents the vortical viscous wake behind the airfoil. The viscous and inviscid models of the unsteady airfoil are the same. Both models have a continuous flux of vorticity from the trailing edge into the wake and there is no discontinuity of vortex strength at the trailing edge. The circulation is the integral of the bound vortex strength.[14]

$$\Gamma = \int_{le}^{te} \gamma(x,t)dx$$

Total circulation is therefore the circulation of the airfoil plus the contribution of the vorticity of the boundary layers.

Theory

The airfoil in steady state conditions is a special case. Here vorticity is shed by the upper and lower boundary layers into the wake. The vortex flux strength from above and below the airfoil is equal and opposite and the vorticity on the airfoil at the trailing edge and in the wake is zero.[14] [13]

Mechanism of Stall

McCullough and Gault[16] studied the mechanism of stall. In a paper published by the NACA in 1951 they described three types of static stall:

Trailing edge stall

Trailing edge stall begins with flow separation at the trailing edge. As the AOA increases, the flow separation moves forward toward the leading edge of the airfoil. This forward movement continues with increasing AOA until flow about the airfoil is completely separated, at which point the airfoil is considered fully stalled.

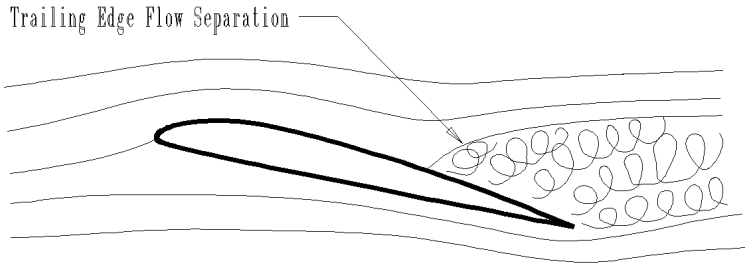

Figure 12, Trailing Edge Stall.

Theory

Thin airfoil stall

Thin airfoil stall occurs first with laminar flow separation that occurs near the leading edge. Initially the laminar flow separation bubble reattaches itself downstream either as laminar or turbulent flow. As AOA is increased the reattachment point moves downstream toward the trailing edge. The area described by the streamline extending from the flow bifurcation point to the reattach point is known as the long separation bubble. This bubble can extend the full chord length of the airfoil and as long as it reattaches, stall does not occur. Once the bubble fails to reattach, the airfoil will stall, usually very abruptly.

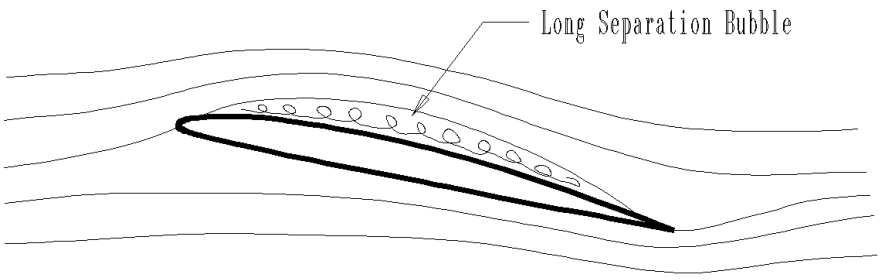

Figure 13, Thin Airfoil Stall with Long Separation Bubble.

Leading edge stall

Leading edge stall begins as a laminar leading edge separation bubble that reattaches upon transition to turbulent flow. Stall occurs when reattachment can no longer take place. At the point of stall, either the leading edge bubble bursts or massive separation of the boundary layer occurs. The separated flow may reattach if the vortex shed by the leading edge forces flow back to the airfoil

surface causing long bubble formation. If the flow establishes a cycle of repeated vortex shedding and flow reattachment the lift-stall cycle can become very violent. Leading edge stall is most prevalent on airfoils with maximum camber near the leading edge.

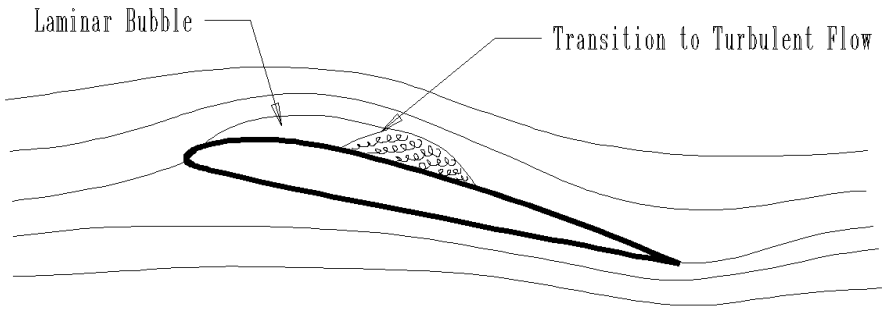

Figure 14, Leading Edge Stall with Transition to Turbulent Flow.

Mechanism of Dynamic Stall

McCroskey summarized the dynamic stall phenomenon in 1982. His description categorized dynamic stall into three phases, stall onset, light stall, and deep stall. McCroskey's descriptions are for an airfoil subject to sinusoidal pitching motion.

Stall onset

At stall onset the airfoil angle of attack is slightly above the critical angle of attack. Small separation begins. At this stage increased lift is present without the penalties of increased drag or increased moment. There is a slight hysteresis in the lift coefficient vs. angle of attack diagram.

Theory

Light stall

Light stall occurs as a slightly higher max AOA is attained. A separation bubble is present. Turbulent flow is prevalent after the bubble along with a thickening boundary layer. Trailing edge flow reversal is established. The viscous boundary layer at the trailing edge flow separation is about the thickness of the airfoil. The behavior of light stall is the most sensitive to the effects of airfoil shape, reduced frequency, and Reynolds number. These factors can influence the dominance of trailing edge or leading edge separation.

Deep stall

Deep stall occurs as the angle of attack greatly exceeds the static critical angle of attack. The deep stall is characterized by the creation of a strong vortex at the leading edge. The vortex is subsequently shed from the boundary layer and moves downstream over the upper surface of the airfoil. As the vortex moves over the airfoil upper surface, values of C_l, C_m, and C_D are dramatically increased over their static values. The viscous layer is now about the thickness of one chord length of the airfoil. As the vortex leaves the trailing edge a large increase in pitching moment known as moment stall and a sharp drop in lift take place. A large amount of hysteresis occurs during this part of the cycle.

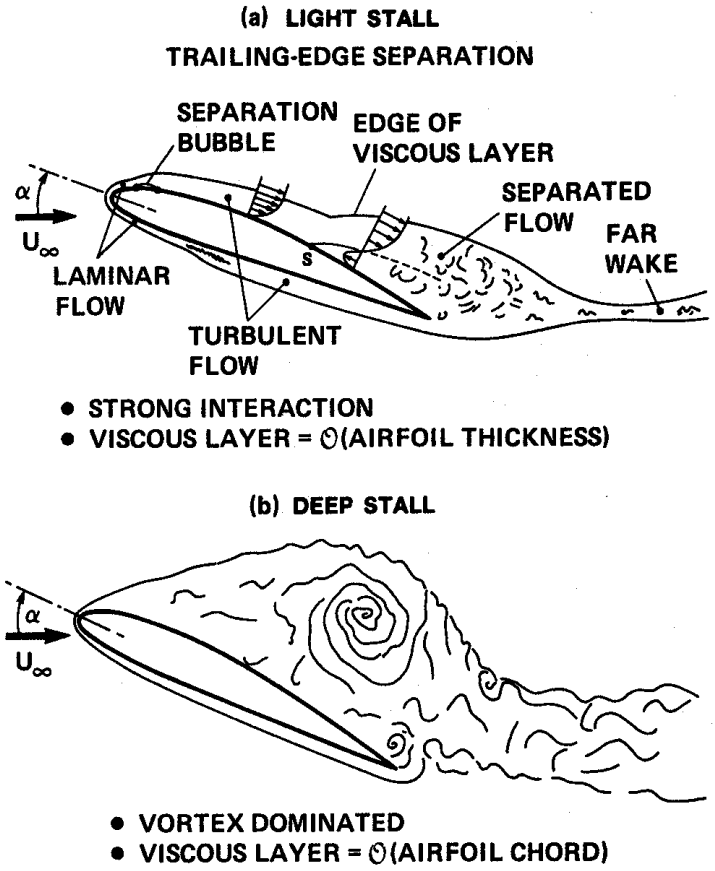

Figure 10 Sketches of flow fields during dynamic stall.

Figure 15, Light Stall and Deep Stall, from McCroskey, Annual Review of Fluid Mechanics, 1982[10]

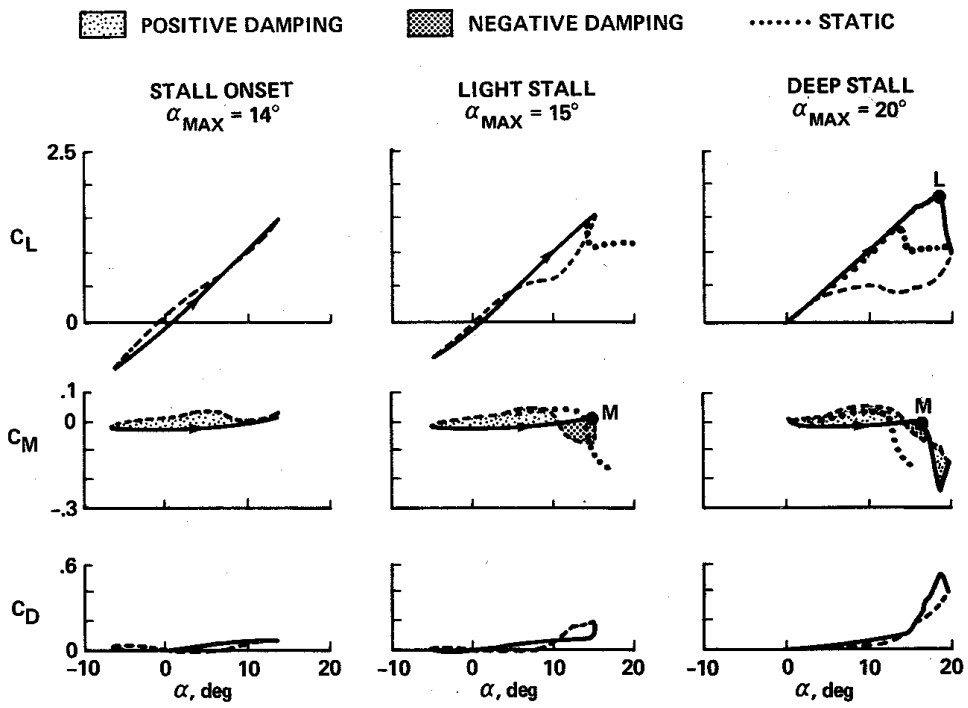

Figure 9 Unsteady forces and moments in three dynamic-stall regimes: $M_\infty = 0.3$, $\alpha = \alpha_0 + 10° \cos \omega t$, $k = 0.10$.

Figure 16 Three stall regimes, $M_\infty = 0.3,\ \alpha = \alpha_0 + 10^\circ \cos \omega t,\ k = 0.10$

McCroskey, Annual Review of Fluid Mechanics, 1982[10]

Theory

Momentum Theorem and the Measurement of Lift from Tunnel Wall Pressures

The ability to measure lift from tunnel wall pressure is based on the Momentum Theorem of Fluid Mechanics. The theorem may be stated as follows:[4]

The time rate of change of momentum of the fluid within a control volume R, plus the rate at which momentum is carried out of R through surface S, is equal in both magnitude and direction to the total force acting on the fluid.

The time rate of change of an element of fluid dR with density ρ and velocity $\mathbf{V}$ is:

$$\frac{d}{dt}\iiint_R \rho \mathbf{V} dR$$

The flux of momentum through an element of control volume surface is:

$$\iint_S \rho \mathbf{V}(\mathbf{V}\cdot\mathbf{n}) dS$$

The force $\mathbf{F}$ exerted on the fluid is divided into three parts, a force exerted on the fluid by a body in the fluid $\mathbf{F}_e$, a pressure force exerted by the fluid on the boundaries of the control volume,

$$\iint_S p\mathbf{n} dS$$

And a body-force exerted by a field such as gravity or electromagnetism,

$$\iiint_R \rho \mathbf{g} d R$$

The combined forces are:

$$\mathbf{F} = -\mathbf{F}_e - \iint_S p\mathbf{n} d S - \iiint_R \rho \mathbf{g} d R$$

Setting this equal to the change in momentum terms above we get:

$$\frac{d}{dt}\iiint_R \rho \mathbf{V} d R + \iint_S \rho \mathbf{V}(\mathbf{V} \cdot \mathbf{n}) d S = -\mathbf{F}_e - \iint_S p\mathbf{n} d S - \iiint_R \rho \mathbf{g} d R$$

Solving for the force exerted by the body:

$$\mathbf{F}_e = -\frac{d}{dt}\iiint_R \rho \mathbf{V} d R - \iint_S \rho \mathbf{V}(\mathbf{V} \cdot \mathbf{n}) d S_e - \iint_S p\mathbf{n} d S - \iiint_R \rho \mathbf{g} d R$$

In the above equation the 4th term on the RHS is the gravity body force which is small and will be ignored. The third term describes the pressure at the boundaries of the control volume. The second term describes the momentum leaving the control volume and the first term describes the change in momentum inside the control volume.

Theory

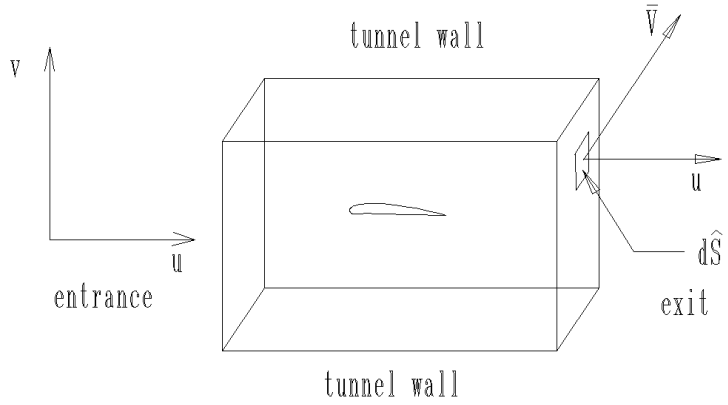

Figure 17, Control Volume of test section.

Since the lift was determined by measurement of the tunnel wall pressure, terms in the **v** direction must be considered.

$$\mathbf{F}_e = -\iint_S p(\mathbf{n}\cdot\ \mathbf{j})dS - \frac{d}{dt}\iiint_R \rho \mathbf{v} dR - \iint_S \rho \mathbf{V}(\mathbf{V}\cdot\ \mathbf{n})dS$$

The third term is rewritten to describe the flow of momentum in the *v* direction out of the right side of the control volume.

$$\mathbf{F}_e = -\iint_S p(\mathbf{n}\cdot\ \mathbf{j})dS - \frac{d}{dt}\iiint_R \rho \mathbf{v} dR - \iint_S \rho \mathbf{v}(\mathbf{V}\cdot\ \mathbf{i})dS$$

Finally, the force exerted by the body is $\mathbf{F}_e$, the first term on the RHS is the pressure force exerted on the control volume boundary of the fluid, in this case the tunnel walls. The second term is the change in momentum of the fluid inside

the control volume in the **v** direction. The last term describes the flow of momentum in the **v** direction out of the **j** side of the control volume or that momentum that escapes detection.

To be absolutely correct in determining lift by measurement of tunnel wall pressure the second and third term must be zero. The third term can only reach zero if the control volume extends to infinity but practically speaking the end of the tunnel test section is usually sufficient. The second term requires steady state conditions. This experiment was not conducted under steady state conditions. An approximation of the Bulk momentum and Unsteady terms is made below. Further discussion is located in Results and Conclusions.

Approximations of the Bulk Momentum and Unsteady Terms of the Momentum Equation

In order to assess the magnitude of the Bulk Momentum and Unsteady terms of the momentum equation and their effect on the lift measurements a simplified model is created below.

Theory

The Bulk Momentum term is;

$$\iint_S \rho \mathbf{V}(\mathbf{V} \cdot \mathbf{n}) dS$$

That portion of the term that describes flow leaving the control volume with some flow component in the *v* direction is of importance here. This term can be approximated by

$$\rho \mathbf{V}^2 A \sin\alpha$$

where;

ρ = fluid density ,

V = free stream velocity

A = area of effected flow

α = angle between effected flow and V

The average AOA for the trajectory used in this experiment is 15 degrees. The exit of the control volume is approximately 5 chord lengths from the model. Because of this distance the angle α will be greatly diminished from the airfoil AOA. A value of 5 degrees was assumed for the calculations below. Area of effected flow was chosen to be the product of span and _ chord of the model. Calculations indicate that the bulk momentum term is of the order of .0622 of the lift produced by the airfoil.

Theory

The Unsteady term is;

$$\frac{d}{dt}\iiint_R \rho \mathbf{v} d\,R$$

That portion of the term that describes acceleration of flow within the control volume with some flow component in the *v* direction is of importance here. This term can be approximated by

$$\frac{1}{\Delta t}\rho \mathbf{V} V \sin(\alpha_2 - \alpha_1)$$

where;

ρ = fluid density

V = free stream velocity

V = volume of effected flow

α = angle between effected flow and V

Δt = time between α_2 *and* α_1

This term accounts for the change in momentum of the flow in the *v* direction during oscillation of the airfoil. α_1 and α_2 are the angles of attack at the extremes of the oscillation cycle, 5 degrees and 25 degrees. The volume is determined from the area, product of span and _ chord, and the velocity. The results of these calculations indicate that the unsteady term is of the order of 24% of the lift produced by the airfoil.

Theory

The bulk momentum term, which may provide an error of approximately 6%, is typical of many tunnel discrepancies. The unsteady term which may contribute an error of approximately 24% is of concern and may preclude the use of this testing technique for unsteady flow lift measurements in the future

Vortex passage from control volume

During testing the airfoil creates circulation as it creates lift. During the course of dynamic stall cycle the airfoil sheds a large vortex as lift breaks down. The diameter of the vortex is approximately equal the chord of the airfoil and the strength of the vortex is equal to the circulation about the airfoil just before the vortex separates from the airfoil. The resulting vortex is bounded by the tunnel walls and is free to be transported down stream with the freestream flow. As the vortex leaves the test section, at some point, half of the vortex will be in the control volume and half will be outside of the control volume. At the time of passage there may be a significant change in momentum in the *v* direction within the test section control volume. In order to evaluate this effect, the function for the flow within a vortex is evaluated. The function for the vortex tangential velocity is combined with terms for density and $\cos(\theta)$ to provide the momentum contribution in the *v* direction only. The resulting function was integrated through one half of the circle of the vortex to obtain the contribution from only one side of the structure. The resulting expression is shown below.

Theory

$$\int_{-\frac{\pi}{2}}^{\frac{\pi}{2}} \int_{0}^{r} \rho \frac{\Gamma}{2\pi r} \cos(\theta) r dr d\theta$$

Integrating this expression yields

$$\frac{\rho \Gamma r}{\pi}$$

which has the dimensions of momentum per unit depth.

Evaluating the above expression using values that correspond to tunnel test conditions at 125 ft/sec.

$$\rho = 0.00238 \text{ slugs/ft}^3$$

$$\Gamma = 21 \text{ ft}^2/\text{seconds}$$

$$r = .1666 \text{ ft}$$

$$\Delta t = 0.00133 \text{ seconds}$$

The resulting value for momentum in one direction for one half of the vortex is 2.65E-3 ft-slugs/sec/ft. The change in momentum as the vortex passes through the exit of the control volume will be twice this value. The depth of the test section is 2 ft. Therefore (2)(2)(2.65E-3)=1.06E-2 ft-slugs/sec. Dividing by the time required for the vortex to pass through the exit of the test section provides the force resulting from this change in momentum.

$$2 \frac{\rho \Gamma r}{\pi} (depth) \frac{1}{\Delta t} = Force$$

The resulting value is 3.98 Lbf. This is a sizable value and approximately 30-40% of the measured value of lift.

The writer has some question regarding the validity of the above analysis. The vortex is a well-organized structure that balances centripetal acceleration with internal pressure. Although the internal velocities are high, the flow remains confined within the structure and there is there is little exchange with the flow outside the structure.

Lift Augmentation Factor

The Lift Augmentation Factor is used to compare the augmented lift resulting from dynamic effects with static lift or lift without dynamic effects. Average Dynamic Lift is the lift produced by an airfoil averaged over the period of the oscillation. The Lift Augmentation Factor is the Average Dynamic Lift Coefficient divided by the Static Lift Coefficient.

$$LAF = \frac{\text{Average Dynamic Lift Coefficient}}{\text{Static Lift Coefficient}}$$

Throughout this experiment the Average Dynamic Lift Coefficient is the integral of the lift coefficient over the period divided by the period, i.e. the average lift coefficient over the period of the oscillation. However the static lift coefficient used

for comparison may be the maximum static lift coefficient attainable by an airfoil or some fraction thereof. Another basis for the static lift coefficient is to use an average of a function generated by transforming the static lift curve to map over the oscillation cycle. Graham and Islam used the first approach in their work. Their augmented lift vehicle was compared to a conventional aircraft. Their rational was that the conventional aircraft would not normally be flown at a lift coefficient greater than 0.8 of the maximum static lift. They therefore chose to multiply their static lift coefficient by a factor of 0.8 times the maximum static lift coefficient.

The second approach, using the average of a function transformed over the oscillation cycle, provides a comparison to the theoretical maximum static lift averaged of the cycle. This approach is also used for comparison in this paper. The details are presented later in section 4 with a description of the calibration and validation procedure. This form of static coefficient lift will be called the Theoretical Average Static Lift Coefficient. In this experiment it has been determined to be 0.8519

4 Experiment

Apparatus

Wind tunnel

The wind tunnel used for this experiment was an open type or Eiffel wind tunnel. The tunnel entrance was fitted with a honeycomb flow straightener with triangular channels measuring approximately 0.50". Behind the honeycomb were four layers of wire mesh screens. The contraction entrance was 50" high x 62" wide. The contraction exit matched the size of the test section, which was 18" high, 24" wide and 36" long. A straight diffuser connected the test section to the fan assembly. A 75hp 3-phase induction motor driving an airfoil type blower through a multiple v-belt drive powered the tunnel. Tunnel airspeed control was accomplished by adjusting an annular damper that was located just before the inlet to the blower. This annular damper consisted of multiple pie shaped damper plates that were linked together to open simultaneously. The tunnel was fabricated from steel.

Tunnel test section

A removable test section was built to slide into the existing tunnel test section. This insert reduced the overall height of the test section from 18" to 6". The insert length was 36". The test section width remained at 24". The insert was supported on rails that were bolted to the support framework of the tunnel. Attach points were provided

at the top and bottom of the insert entrance and exit to fasten a contraction insert and a diffuser insert to adapt the reduced internal height of the insert to the internal height of the tunnel.

A two piece contraction insert was fabricated from fiberglass. One piece was attached to the top of the existing contraction and the other piece to the bottom of the contraction. The inserts matched the contraction exit to the lowered test section ceiling and to the raised test section floor. The leading edge of the insert was fastened to the contraction with through bolts. The trailing edge of the insert was fastened to the entrance of the test section insert with bolts.

The walls of the removable test section were made of Plexiglas. These fit tightly onto the sides of the test section and were hung on a track. During testing, low pressure inside the tunnel held these windows firmly in place. The windows supported the pressure transducers used for lift measurement.

Photo Images of the tunnel and test section are located in Appendix M and CAD drawings of the test section and contraction are located in Appendix N.

Experiment

Test airfoil

The test airfoil was a NACA 0012 section of 6” span and 4” chord, CNC machined from hard maple. Aluminum plates were screwed and glued to the ends of the airfoil to act as aerodynamic end plates and act as reinforcements for the support points machined into the ends of the airfoil. The airfoil was supported so that it may pivot at the _ chord point. The wooden surfaces have been sealed with spray acrylic varnish.

A photo image of the airfoil is located in Appendix M.

Oscillation mechanism

The test airfoil was supported at its ends by the upper and lower windows located on the ceiling and floor of the tunnel. The upper window was supported by bearings that allowed it to rotate. The lower window was fixed. Both windows had a hole in the center to support the test airfoil. The upper rotating window had an additional hole for a drive pin that engaged a hole in the end of the test airfoil.

A crank and connecting rod assembly oscillated the upper window. The connecting rod “small end” was connected to the perimeter of the window assembly with a small adapter plate. The “large end” of the connecting rod was attached to an adjustable throw crank assembly with a self-aligning roller bearing. The adjustable throw crank assembly permitted adjustment of the amplitude of the sinusoidal motion of the airfoil. The crank throw was adjusted by loosening the binding nut that holds the

bearing in position and sliding the bearing, shaft and binding nut to the appropriate location and tightening.

Photos images of the crank and connecting rod assembly are located in Appendix M.

Drive motor & Transmission

The transmission assembly was constructed of 0.75" aluminum plate, bolted together to form a long rectangular box that spanned the top longitudinal support members of the tunnel test section. The oscillating mechanism was driven by a 1.5 hp Baldor 56TC frame DC motor with an electronic variable speed drive. The motor was face mounted to a sliding plate to permit adjustment. Two cartridge type ball bearing assemblies supported the output shaft. The motor, through a timing belt drive, drove the output shaft. Timing belt pulleys and belts permitted the transmission to be assembled with a 1:2, 1:1, and 2:1 motor/output-shaft drive ratio. These ratios permitted the output shaft to turn at a rotational frequency range of 5-60 Hz.

Motor speed adjustment was made with the potentiometer that was part of the speed control unit. Rotation speed of the crankshaft was set and monitored by observing the output of the crank position transducer with an oscilloscope with frequency readout. Crankshaft rotational frequency could be set and remained constant within 2%. Photo images of the drive motor and transmission appears in Appendix M.

Experiment

Instrumentation

This experiment required instrumentation for lift, airspeed, and angular position.

Lift was measured by measuring the pressure along the tunnel walls. Two arrays of seven high sensitivity differential pressure piezoresistive transducers were used to measure pressure at both tunnel walls. The tunnel wall pressure transducers had a measurement range of 0-0.3 psi. Static side of the transducers was connected to the static port of the pitot static assemblies described below.

Tunnel free-stream velocity was measured with a high sensitivity, differential piezoresistive, transducer that was plumbed to two pitot static tube assemblies. The pitot static tube assemblies were located in opposite corners of the test section in order to average static pressure. The differential transducer used for free stream velocity had a range of 0-0.8 psi..

The piezoresistive devices were internally connected as a strain-bridge and required external excitation in order to function. Small constant current power supplies provided external excitation. These power supplies were constructed from integrated circuit operational amplifiers. The operational amps, zener diodes, and necessary trimpots were assembled onto a circuit board. Each circuit board had circuitry for

three transducers. Two 9-volt transistor batteries in series that were regulated to a constant 15-volt output provided power to the constant current power supplies.

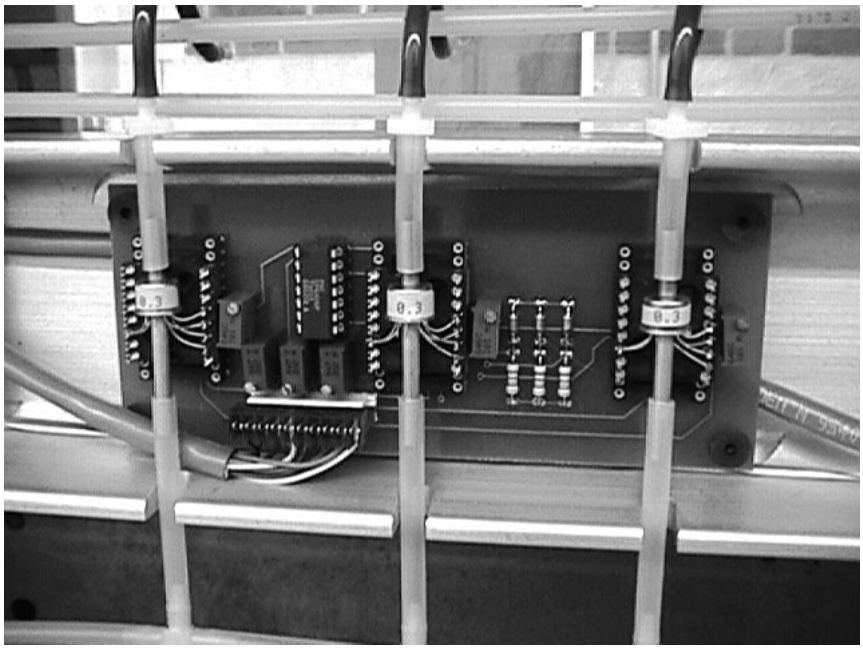

Image 1, Transducer circuit board

The piezoresistive transducers had a linearity of +/-0.5%. The absolute output varied considerably and each transducer required adjustment to the bias current to scale the transducer to a known differential pressure source. The differential pressure source used was a U tube manometer and a syringe. The current bias and zero point bias were adjusted with small potentiometers on the circuit board.

Three circuit board assemblies along with the necessary transducers and power supplies were mounted in an aluminum channel to form the transducer array or rail.

Experiment

A transducer rail assembly was mounted to each of the two windows on the test section.

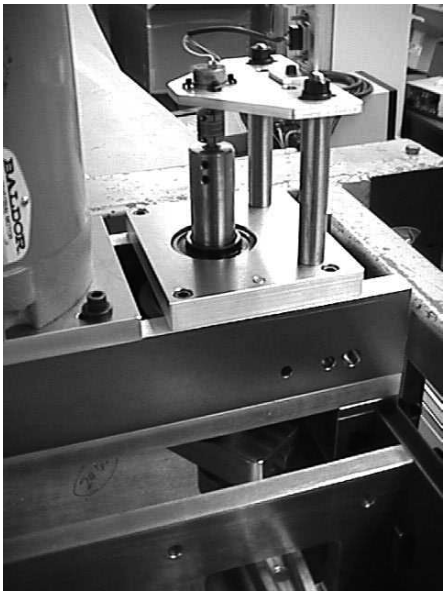

Image 2, Rotary transducer shown coupled to crankshaft.

Angular measurement of the airfoil position was accomplished using a 5k ohm precision potentiometer. The potentiometer was attached to the output shaft and made one revolution for each cycle. The potentiometer was biased using the same constant current power supply that was used for the piezoresistive transducers. Voltage information was converted to angular position by the data acquisition system.

Additional photos images are in Appendix M.

Schematics and Data sheets are located in Appendix G, H. and I

Experiment

Data Acquisition

The data acquisition system consisted of a National Instruments SCXI-1000 chassis, an SCXI 1200 multiplex module, an SCXI 1100 32-channel instrument amplifier module and an IBM compatible laptop computer. The SCXI 1200 module controlled the scan of modules in the chassis, as well as providing parallel port communication with a host computer.

The application that ran the SCXI system was Labview, by National Instruments Corp. The application controlled the actions of the SCXI-1200 scanner and provided a graphical interface of multiple controls and indicators that displayed the values for each of the inputs of the instrument amplifier. The graphical interface provided controls to start and stop data acquisition, as well as determine the data acquisition rate, number of samples to collect and the file path for data storage.

The data acquisition program was a Labview virtual instrument (VI). Running the VI first initialized the SCXI 1100 amplifier then started scanning the SCXI 1100 amplifier at the selected rate. The selected number of scans were executed and the data from each scan was held in the buffer contained in the SCXI 1200 control module. Once scanning was complete, the VI processed the information from the buffer. The main 'For Loop' of the VI accepted data from the buffer, one scan at a time. Each scan was a one-dimensional array of 32 values. The VI decoded the array

into the individual channels for tunnel wall pressures, free stream velocity and crankshaft position. From this data the VI computed lift, Lift coefficient, and angle of attack.

Lift was computed by integrating the pressures on the walls of the tunnel using a Riemann sum technique. Free-steam velocity was measured with a pitot static tube assembly and a differential pressure transducer. Transducer input was scaled to provide dynamic pressure to the VI. The lift coefficient was computed knowing dynamic pressure and lift. Density and airfoil area were entered into the VI front panel as constants. Crank angle was determined from the voltage input from a 350-degree precision potentiometer. Airfoil angle of attack was determined from crank angle with an algorithm running in the VI. Data was stored in a text file delimited as follows:

Crank angle Lift coefficient Angle of attack Lift coefficient

This arrangement facilitated further manipulation within the spreadsheet program.

A printout of the program is in Appendix E.

Experiment

Measurement Calibration and Validation

The locations for tunnel wall pressure ports were determined experimentally. Measurements of change in tunnel wall pressure were made at a number of locations along the tunnel wall, with the tunnel running and with a NACA 4412 airfoil of approximately 12” chord mounted vertically in the tunnel. A water-filled U tube manometer was used for pressure measurement. Pressure measurements were made while the airfoil AOA was adjusted through the range of zero lift to the critical AOA. The pressure at ports in the wall was then graphed. The results showed a pressure distribution similar to a gauss distribution curve. The point at which the pressure differential between max lift and zero lift was 0.1” water was the point chosen for the extreme most port location upstream and downstream of the center of the test section. The remaining port locations were chosen to best fit the curve with a trapezoidal approximation.

Individual transducers were calibrated using a U-tube manometer filled with water. Each piezoresistive differential pressure transducer was disconnected from its tunnel wall port and static connection. The transducer was then connected to both sides of the manometer. A tee connector was placed in line with the tube on one side of the manometer and connected to a plastic industrial syringe. The syringe could then be used to apply a pressure or vacuum to the transducer, which was concurrently measured with the manometer. The circuit for each transducer was first adjusted to

balance the transducer output to zero millivolts when zero differential pressure was applied. The constant current power supply was then adjusted to scale the output of each transducer so that all transducers were scaled alike. The zero offset or balance was again checked. If the balance had changed the process was repeated.

Once the transducers were calibrated the overall lift measurement system could be calibrated. The lift measurement system consisted of the transducers, SCXI instrument amplifier and the Labview program. Within Labview there were provisions for scaling the lift coefficient output of the program to correspond with published lift coefficient data for the NACA 0012 airfoil. Scaling was accomplished by testing the NACA 0012 airfoil at numerous values of AOA and plotting the coefficient of lift values vs. AOA to form a standard lift coefficient diagram. These tests were conducted at a Reynolds number of approximately 300,000. The slope and y-intercept of the linear portion of the curve were measured and compared with the NACA 0012 data. The gain and offset were adjusted within the Labview program so that slope and y-intercept agreed with the published data for the NACA 0012. The resulting lift coefficient vs. AOA diagram is shown below in figure 18 along with the NACA Data. A full size diagram is in appendix C Calibration Plot and the NACA Data is shown full size in appendix K.

Experiment

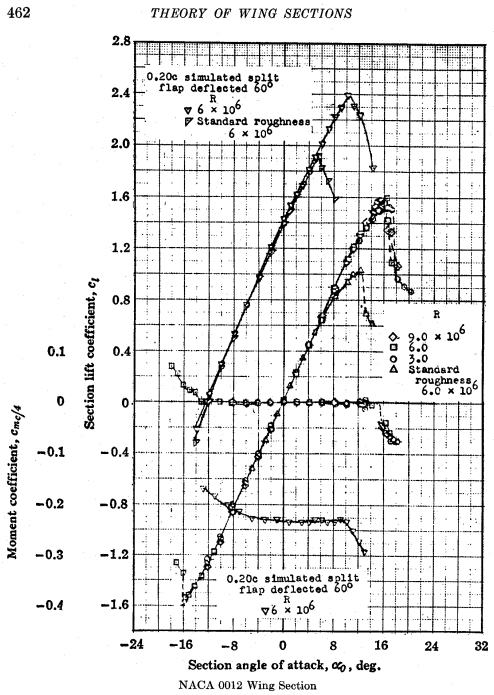

Error! Not a valid link.

Figure 18, Calibration Plot and Data for NACA-0012 Airfoil.

Test of Static Stall, generation of calibration plot

Prior to testing and recording dynamic data, a static test was run with the NACA 0012 airfoil at a Reynolds number of 300,000. This test was conducted by positioning the airfoil at 12 different AOA locations between 5 degrees and 20 degrees. At each value of AOA the lift coefficient of the airfoil was measured. The resulting graph plotted from the data was used to calibrate the tunnel data acquisition apparatus and to serve as a static lift reference for the dynamic tests. The plot of this test is in Appendix B. Unlike standard lift coefficient vs. AOA plots, which extend only a few degrees beyond the critical AOA, this plot extended to an AOA of 20 degrees or

about 8 degrees beyond the critical AOA. The region beyond stall and up to 20 degrees AOA exhibited a lift coefficient of approximately 0.8.

The static lift coefficient vs. AOA plot agree within 10% with published data for the NACA 0012 airfoil over the range common to both sets of data.

The maximum lift coefficient of 1.4 at 12 degrees is somewhat less that the published value of 1.5 at 15.5 degrees. The published data is for tests conducted at Reynolds numbers of 3.0x10^6 to 9.0x10^6. Data is not available for a direct comparison with the lift coefficient of the NACA 0012 airfoil at a Reynolds number of 300,000. Low Reynolds number testing was conducted on the NACA-0009 airfoil which, is a member of the same series as the NACA 0012. These airfoils differ in percent thickness while their thickness distributions remain the same. The tests on the NACA 0009 airfoil by Selig[17] indicate a maximum lift coefficient of 0.75 at a Reynolds number of 300,000 and an AOA of 10 degrees. The slope of the lift coefficient AOA curve at low values (Cl < 0.4)is the same as the slope of data from tests at higher Reynolds numbers, 0.105 Cl/deg AOA

Tests conducted by Selig et al were done using a very low turbulence tunnel. It is notable that for almost all of the sections tested by Selig, the critical AOA for those airfoils, where a critical AOA is apparent, was 10 degrees. Some airfoils had a

critical AOA approaching 11 degrees but this was rare. This is notable since the critical AOA of airfoils tested at higher Reynolds numbers and higher turbulence levels have critical AOAs that regularly approach 14-15 degrees.

The WPI open wind tunnel was not a low turbulence tunnel. Turbulence spectra and magnitude were not measured quantitatively, however the use of tufted probes indicated significant turbulence in the test section. Using a smoke generator and wand, the presence of a relatively strong vortex was detected that extends out through the flow straightening honeycomb at the entrance of the tunnel and down to the floor. It is believed that this vortex is a result of the action of the airfoil fan and speed control vanes that are mounted to the fan section. These flow conditions preclude any close quantitative comparisons between the results of this experiment and the results of the work by Selig.

Although direct quantitative comparisons with others was not possible the objective of this experiment was not to find quantitative lift data that can be correlated to the work of others but to determine the change in the average lift generated by an airfoil subject to dynamic stall conditions. The Calibration Plot shown in Appendix C is the baseline with which all dynamic data acquired in this experiment was compared.

Experiment

Test variables

The variables that were controlled in this experiment were the free stream velocity, oscillation frequency, oscillation amplitude, average angle of attack and the physical dimensions of the test model, chord and span. Variables that were functions of the above are Reynolds number, and the reduced frequency k

$$\mathrm{Re} = \rho \frac{Vl}{\mu}$$

$$k = \frac{wc}{2V_\infty}$$

where: w = rotational frequency, Hz.
c = chord of airfoil, feet .
V_∞ = free stream velocity, ft/se

Experiment

Experimental Procedure

Once the apparatus was installed and the model was secured the throw of the crank was adjusted to provide the correct variation in pitch and average pitch position. The crank position potentiometer was adjusted to insure alignment with the zero crank position. An oscilloscope with frequency readout was attached to the rotary transducer output. The Labview data acquisition software was started and the virtual instrument (VI) for this experiment was loaded. The path for file storage was designated. The wind tunnel was started and the velocity was set using a pitot static tube and a sensitive airspeed indicator. Once the tunnel velocity was set, the motor driving the oscillating window was started and adjusted to the correct frequency using the oscilloscope for a frequency and signal reference.

Once all parameters were adjusted, the virtual instrument was started. The VI set up the SCXI 1100 amplifier parameters and started taking data. Data was taken at a constant rate of 20 scans per second for 200 scans. The test was repeated until 1000 data measurements had been taken for each test point. After each test the data was appended to the data file. 1000 data points proved more than adequate to cover the test cycle. The data was then processed using a spread sheet program.

Experiment

Each scan of the SCXI 1100 multiplexed amplifier card sampled each of the selected analog channels. These channels provided analog data for tunnel wall pressure, tunnel free stream velocity, and crank angle.

Experiment

Experimental Errors

Wind tunnel boundary corrections

The primary goal of this experiment was to compare the dynamic test results of the test airfoil to the static test results of the same airfoil in the same tunnel. This fact should obviate the need for corrections. However, since correlation will be made to full scale devices such as airplane propellers and helicopter rotors a check of tunnel boundary corrections for Lift Coefficient and AOA are appropriate. This requires computing the solid blockage and wake blockage of the model in the tunnel test section.

An expression for solid blockage correction is given by Thom:[18]

$$_{sb} = (K_1(volume))/\ C^{3\ /}$$

where $K_1 = 0.52$

C = test section area .

An expression for wake blockage correction is also provide by Thom:[19]

$$_{wb} = \frac{c/\ h}{4} c_{du}$$

where c = airfoil model chord

h = height of test section .

c_{du} = uncorrected Drag coef.

Experiment

Total blockage is given by:[20]

$$= _{sb} + _{wb}.$$

Calculating total blockage, based on the NACA 0012 airfoil with 0.25' chord, 0.5' span, uncorrected drag coefficient of 0.01, test section height 2.0', model volume = 0.7(span)(thickness)(chord).

$$_{sb} = 0.0010237$$
$$_{wb} = 0.0003125 .$$

Total blockage is:

$$= 0.00133625 .$$

Corrections for AOA and Coefficient of Lift can be determined from the following equations. Values subscripted with u are uncorrected values.[20]

$$\alpha = \alpha_u + \frac{57.3\sigma}{2\pi}\left(c_{lu} + 4c_{m1/4}\right)$$

$$c_l = c_{lu}(1 - \sigma - 2)$$

where, $\sigma = \frac{\pi^2}{48}\left(\frac{c}{h}\right)^2$.

Experiment

Calculating the corrections based on the NACA 0012 airfoil with 0.25' chord, 0.5' span, test section height of 2.0'. Assuming an AOA of 10 degrees and moment coefficient =0

$$\alpha_u = 10.0$$
$$c_{lu} = 1.1$$
$$c_{m1/4u} = 0.0$$

$$\sigma = .003213$$

A corrected value for AOA and Coefficient of lift are found.

$$\alpha = 10.032229$$
$$c_l = 1.093529$$

These values are within 0.35% for α and within 0.6% for C_l the uncorrected values. Generally a deviation of less than several percent is considered acceptable and indicates that minimal boundary corrections are required to correlate the test data to full scale devices such as propellers and helicopter rotors blades.

Free stream velocity error due to varying blockage with oscillating airfoil

The corrections for solid blockage and wake blockage were less than 1%. These corrections were calculated for an AOA of 10 degrees. Corrections for varying blockage were unnecessary.

Experiment

Finite wing error

Finite wing error is the result of an airfoil having a finite length. For a finite airfoil, flow at the end of the airfoil is three-dimensional, and the effects reduce the lift produced by the airfoil. The airfoil in this experiment spanned the tunnel floor to ceiling, therefore finite wing effects were not present and did not need to be considered.

Because the finite airfoil was attached to the tunnel walls, the ends were subject to boundary layer flow. This had the effect of reducing the free stream velocity and lift. The boundary layer thickness is given by:

$$\delta \approx 5.0\sqrt{\frac{vx}{U_\infty}}$$

Where the boundary layer thickness is defined as the velocity at the edge of the boundary layer and is 99% of the free stream velocity. Evaluating the above expression for δ using:

Kinematic viscosity $v = 1.6x10^{4}$ at a temperature of $68\,\mathrm{F}^\circ$

Free stream velocity $U_\infty = 100$ ft/sec

Characteristic length $x = 6.0$ feet , for the distance from the contraction to the model.

Experiment

Gives $\delta = .185"$.

Similarly the momentum thickness which is the loss of momentum compared to the potential flow is defined by:

$$\delta_2 = 0.664\sqrt{\frac{vx}{U_\infty}}.$$

Which when evaluated using the above values yields:

$$\delta = 0.0246".$$

This value of momentum loss thickness was less than the thickness of the airfoil endplates. Boundary layer effects were negligible.

Experiment

Results

Test of Dynamic Stall

Twenty-six tests were conducted at values of reduced frequency ranging from 0.02 to 0.3 and Reynolds numbers ranging from 200,000 to 500,000. The test schedule is shown in appendix D. Data for each test was recorded in a file format exportable to a spreadsheet. Each data point included values for crank angle, AOA computed from crank angle and lift coefficient. Within the spreadsheet application the data were averaged over ten values. Data for each test were plotted in two different formats and included in appendix B. At the beginning of appendix B is a Test Summary Table .

For the twenty-six tests conducted, there are two plots for each set of test data. These plots are located in appendix B. For each test the upper diagram is a lift coefficient vs. AOA plot. This plot is useful in comparing the dynamic behavior of the airfoil with airfoil static behavior since most airfoil static performance data is presented in this format. The most notable difference between the dynamic and static performance is the presence of significant hysteresis in the cycle. During the cycle the AOA changes from 5 degrees to 25 degrees and back to 5 degrees. Data follows a primarily clockwise path around the loop as a function of time. In some cases the path loops across itself, generally near 5 degrees. The lower diagram is a plot of lift coefficient vs. crank angle. Note that the range of crank angle is 0-350 degrees. This

is a result of an electrical dead spot in the rotary potentiometer between 350-360 degrees. During each test the crankshaft was set at a fixed rotational speed, which makes crank angle a linear function of time. Crank angle data was most useful for finding the time average lift coefficient for each test. Since crank angle is a linear function of time, lift coefficient could be averaged over crank angle. The crank angle is a periodic function therefore integration need only be done over one period.

For each test an average lift coefficient was determined. The results are compared graphically in figure 19 below. Lift coefficient is plotted as a function of reduced frequency. Each line represents values of average lift coefficient at the same Reynolds number.

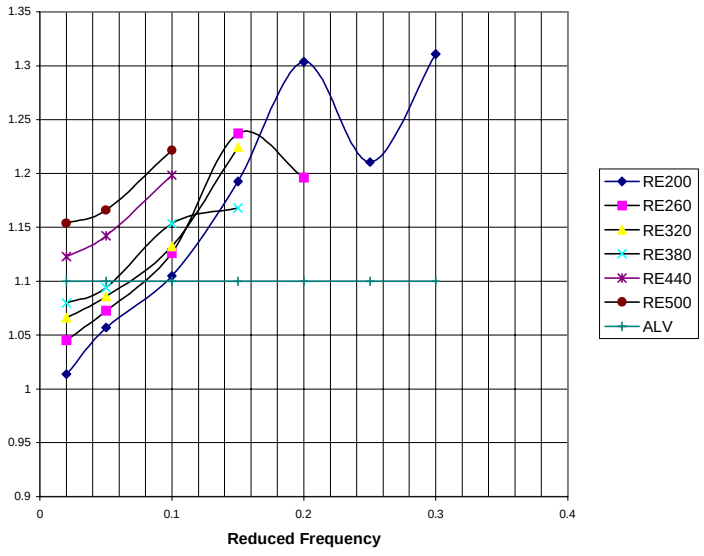

Figure 19, Summary Plot, Average Lift Coefficient vs. Reduced Frequency at constant values of Reynolds Number.

Experiment

It is notable that average lift coefficients generally increased with increasing Reynolds number. This trend corresponds with static lift coefficient data. Increasing reduced frequency produced increased average lift coefficients at lower frequencies. At higher reduced frequencies the average lift coefficient fluctuated. The fluctuation at higher reduced frequencies was only apparent for tests at Reynolds numbers of 200,000 and 260,000. Mechanical issues prevented the apparatus from reaching the higher reduced frequencies at higher Reynolds numbers.

The fluctuations in average lift coefficient at higher reduced frequencies are likely due to the effect of the vortex shed from the leading edge. It is believed that at certain frequencies the shed vortex has a more prolonged effect on lift coefficient. More investigation is required to verify this effect.

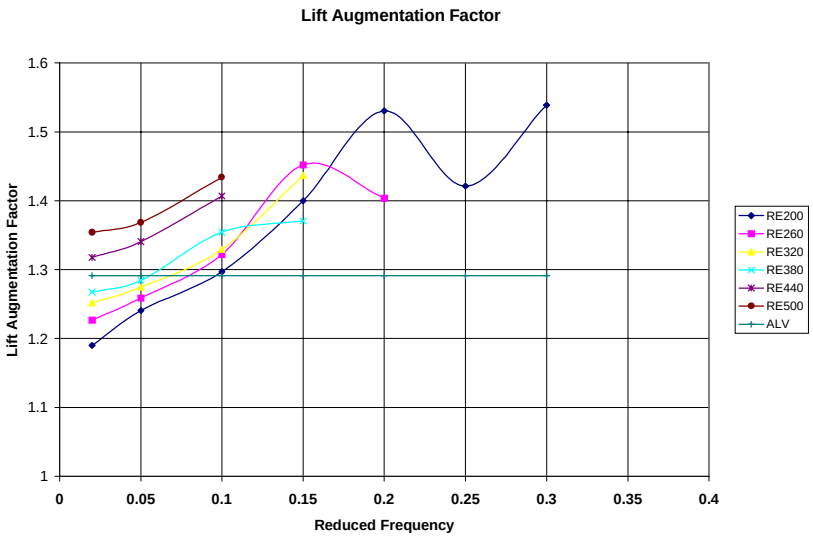

Figure 20, Summary Plot, Lift Augmentation Factor vs. Reduced Frequency.

Experiment

The results were again plotted using the Lift Augmentation Factor. While the shape of the lines is the same as shown in figure 19 above, the diagram shows how dramatic an increase is achieved in average lift.

In the diagram in figure 21 below, Lift Augmentation Factor was plotted against Reynolds Number with lines of equal reduced frequency. This shows a general trend towards increased LAF as Re is increased. There are several exceptions, at reduced frequencies of .15 and .2 the trend is not towards greater values of LAF. It is believed that Reynolds number has some effect on the behavior of the shed vortex similar to the reduced frequency but not as dominant.

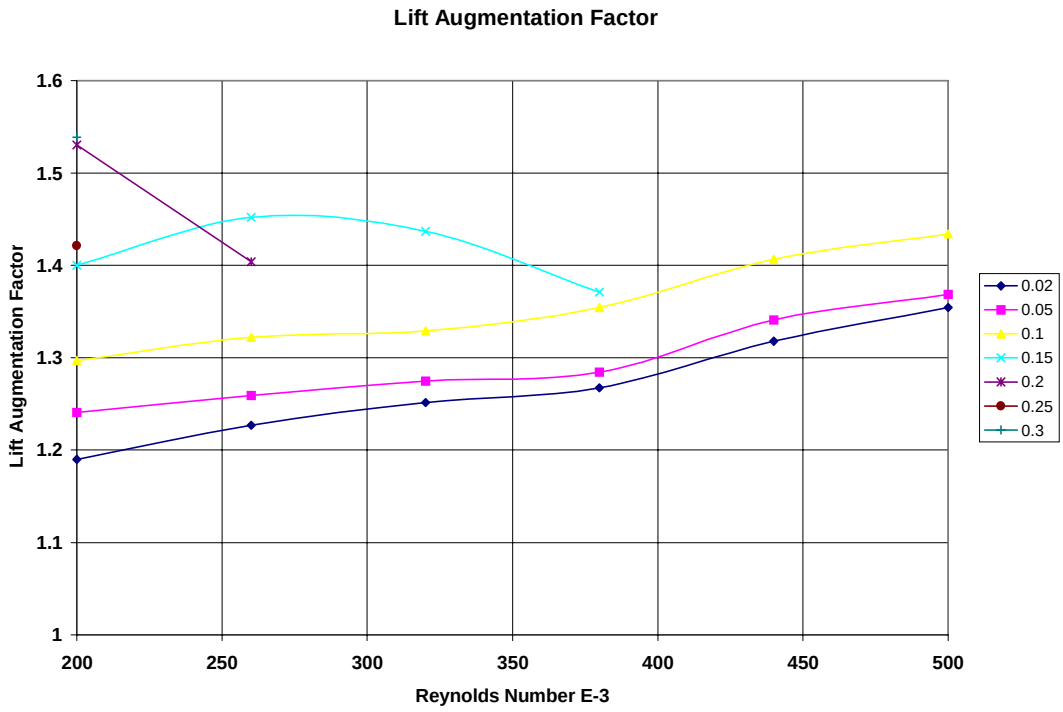

Figure 21, Summary Plot, Lift Augmentation Factor vs. Reynolds Number.

Experiment

McCrosky and McAllister had both indicated that Reynolds number had little or no effect on Dynamic Lift. Here it is apparent that there is an effect that is of the same order seen in static airfoil data.

Discussion of Test Data

In the following paragraphs individual tests data is reviewed. Several characteristic plots of Lift Coefficient vs. AOA are included for each test series. The complete sets of data plots are located in appendix B. Note that for each of the following diagrams the path of the function with respect to time is clockwise.

Test Series 2_200 through 2_500

This series of tests were conducted at the lowest reduced frequency of the experiment, k=0.02. No dynamic effects were detected at the lower Reynolds numbers. At Reynolds numbers of 440,000 and 500,000 there was a slight increase in lift coefficient beyond the critical angle of attack. Beyond the critical AOA the lift coefficient did not quite drop down to the static lift coefficient values.

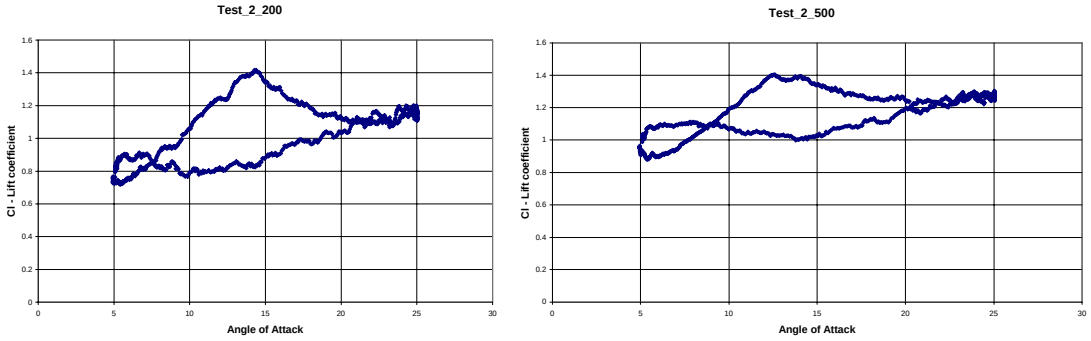

Figure 22, Lift Coefficient vs. AOA, Test 2-200, 2-500, k=.02, Re=200E3, 500E3.

Experiment

Minimal dynamic effects at k=0.02 is consistent with the findings of others.

Test Series 3_200 through 3_500

In this series of tests conducted at k=0.05 the dynamic effects were more pronounced. The results of the first of the series conducted at Re = 200,000 had dynamic effects characterized by the lift coefficient remaining at the maximum value past the critical AOA at approximately 14 degrees and remaining at this value to an AOA of 20 degrees. After 20 degrees the lift coefficient began to roll off. The plot of lift coefficient shown below in figure 23 showed significant unsteadiness after the critical AOA.

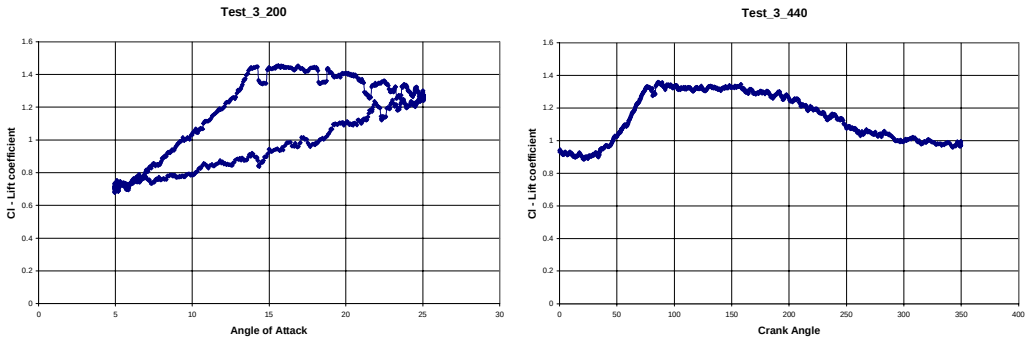

Figure 23, Lift Coefficient vs. AOA, Test 3-200, 3-440, k=.05, Re=200E3, 440E3.

This pattern remained very similar until reaching a Reynolds number of 440,000. Above this Reynolds number the lift coefficient reached the maximum at the critical AOA and remained at that value until reaching the maximum AOA of 25 degrees. The lift coefficient was also significantly smoother at these values. Note that the maximum lift coefficient is actually lower than shown in test 3-200, however the path

of the function while returning to 5 degrees remains much higher than in test 3-200 hence the average lift coefficient is greater. This phenomenon suggests an effect of the shed vortex somehow sustaining the lift coefficient at a higher value throughout the oscillation cycle.

Test Series 4_200 through 4_500

These tests were conducted at a reduced frequency of k=0.1. Dynamic effects in this series were evident throughout the full range of Reynolds number. The first test at Re=200k shows the lift coefficient continuing to gradually increase after reaching the critical AOA then leveling off at 20 degrees. See figure 24 below.

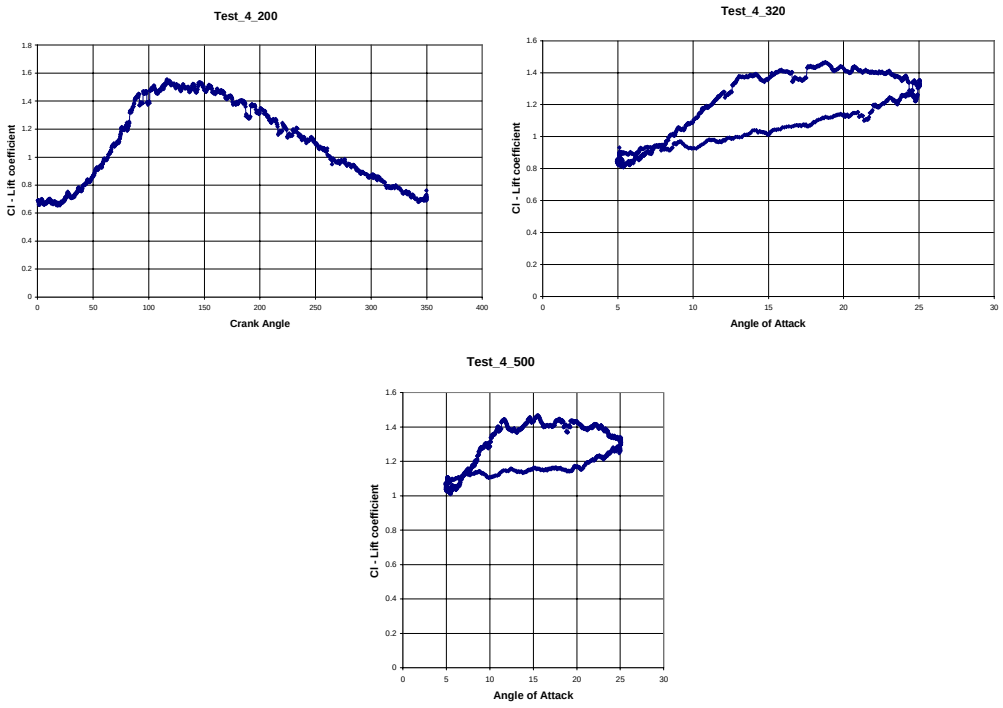

Figure 24, Lift Coefficient vs. AOA, Test 4-200, 4-320, 4-500, k=0.1, Re=200E3, 320E3 , 500E3.

Experiment

The critical AOA breakpoint, or the point at which the initial linear portion of the lift coefficient curve breaks, appears at about 14 degrees. At the maximum AOA of 25 degrees, the lift coefficient reverses abruptly then smoothly decreases as the AOA decreases to 5 degrees. In the 20 degree to 25 degree zone the lift coefficient showed considerable roughness both as the AOA was increasing and decreasing. As Reynolds number is increased, the critical AOA breakpoint moved from 14 degrees to about 12 degrees. The general shape of the lift coefficient curve remained the same throughout the series. The roughness between 20 and 25 degrees diminished after Re=320k but roughness returned at Re=500k with very large variations in lift coefficient between 12 degrees and 25 degrees.

There is no similar data with which to compare these results. The "roughness" at certain angles of attack of the CL vs. AOA diagram is of interest. The frequency of the oscillation probably precludes an explanation by the action of the shed vortex but more likely suggests some very rapid flow detachment-reattachment mechanism at some point on the airfoil.

Test Series 5_200 through 5_380

This series conducted at k=0.15 was limited to four tests due to mechanical limitations of the oscillation apparatus. Diagrams of these tests were similar to the tests of the series 4_200 – 4_500. Diagrams are shown below in figure 25.

Experiment

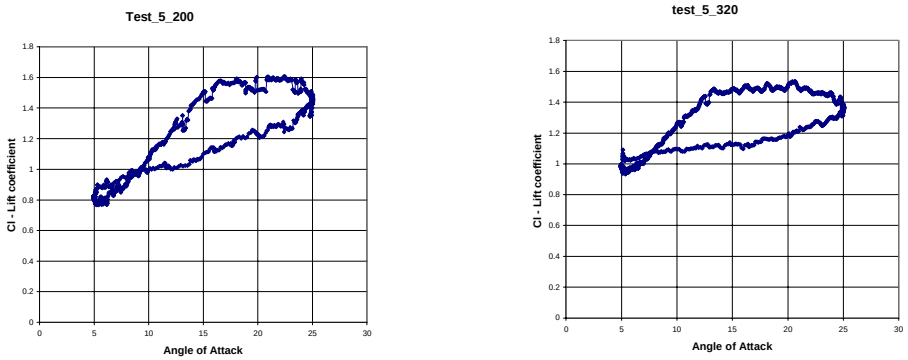

Figure 25, Lift Coefficient vs. AOA, Test 5-200, 5-320, k=.15, Re=200E3, 320E3

The critical AOA changed from 16 degrees at Re=200k to 12 degrees at Re=380k. The roughness present in the previous series was present only at Re=200k and Re=320k.

The roughness is consistent with that found in previous tests. The shift in critical AOA is not understood and has not been observed in the data from the work of others.

Test Series 6_200 through 6_260

This series conducted at k=0.2 was limited to two tests due to mechanical limitations in the oscillation apparatus. At Re=200k the critical AOA breakpoint was at approximately 17 degrees. Between 20 and 25 degrees AOA there were large fluctuations in lift coefficient. Increasing the Re to 260k the critical AOA breakpoint had become less distinct but appeared to be at about 14 degrees. Between 13 degrees and 20 degrees AOA there were significant fluctuations in lift coefficient. Both

diagrams show large hysteresis loops at AOA between 5 and 10 degrees. These diagrams are shown below in figure 26.

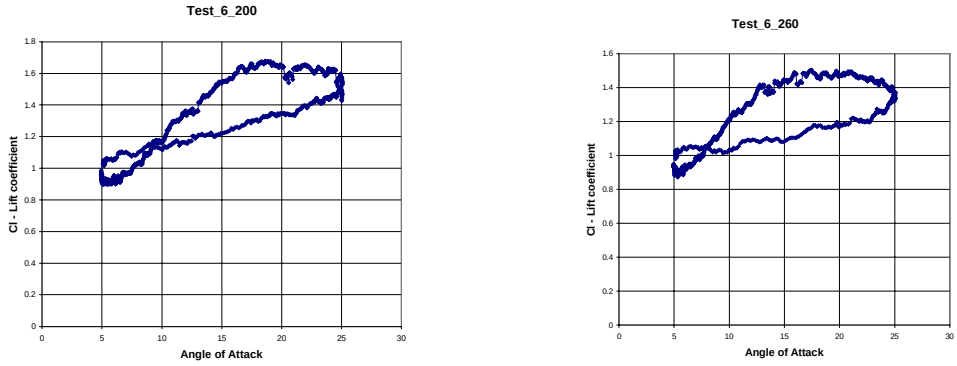

Figure 26, Lift Coefficient vs. AOA, Test 6-200, 6-260, k=0.2, Re=200E3, 260E3.

The results of this series are consistent with the previous tests. The same phenomenons appear again.

Test Series 7_200

This series consisted of only one test at Re=200k due to limitations of the oscillation apparatus. The resulting diagram shows a non-linear lift coefficient curve that rolls off slowly with a non-distinct critical AOA break at approximately 18 degrees. There is a significant dip in lift coefficient between 20 and 25 degrees. The two most notable differences in this diagram are the nonlinearity of the initial part of the diagram up to the critical AOA and that the maximum lift coefficient is at the critical AOA rather than continuing to increase after the critical AOA. Like many of the

other tests there was a sizable hysteresis loop between 5 and 10 degrees. The diagram is shown below in figure 27.

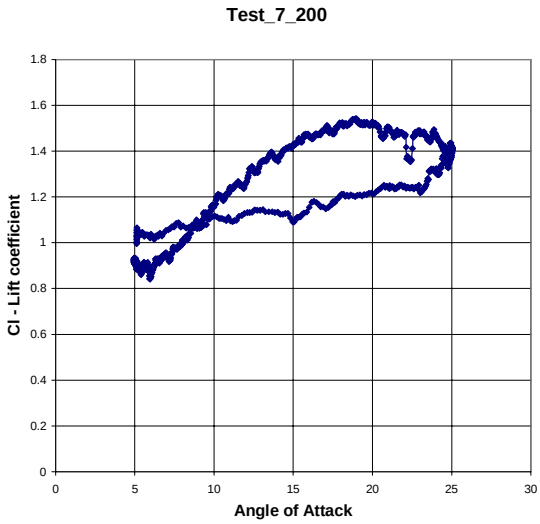

Figure 27, Lift Coefficient vs. AOA, Test 7-200, k=0.25, Re=200E3.

At higher values of reduced frequency the lift coefficient curve becomes non-linear. The reason for this phenomenon is not known. The very sharp notch in the curve at 22 degrees AOA is most likely from some recurring flow detachment/reattachment at that point in the cycle.

Test Series 8_200

With the reduced frequency at k=0.3 this test like the previous two was only conducted at Re=200k. The resulting diagram shows a non-linear initial portion of the curve that rolls off slowly. There is a non-distinct critical AOA at about 20 degrees. Throughout the range of 12 to 25 degrees there is significant unsteadiness which continues through the decreasing AOA part of the diagram to 15 degrees.

Experiment

There is a large hysteresis loop between 5 and 10 degrees. The diagram is shown below in figure 28.

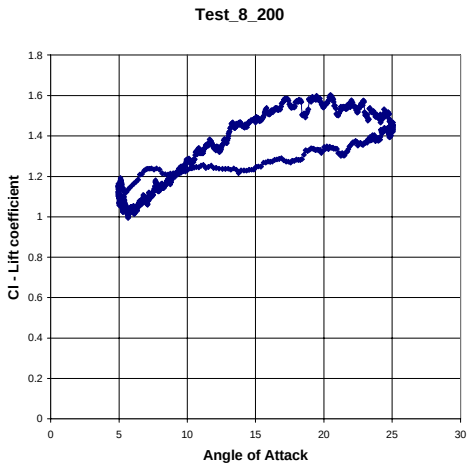

Figure 1, Lift Coefficient vs. AOA, Test 8-200, k=0.3, Re=200E3

This test was conducted at the highest reduced frequency throughout this experiment. The non-linear portion of the lift coefficient curve persists and significant roughness has reappeared. If the roughness is a result of a rapid detachment/reattachment cycle as hypothesized the conditions under which this occurs are not known at this time and will require further experimentation to determine.

Experiment

Comparison

Average lift coefficient results are compared with the results from the work of Graham and Islam and the Augmented Lift Vehicle. The average lift coefficient is then compared with the average lift coefficient determined from averaging the static lift coefficient calibration test. The results of the testing of the NACA-0012 airfoil at Reynolds number of 500,000 by McCroskey and McAlister are compared with the data from this experiment.

Comparison with Graham and Islam Augmented Lift Vehicle (ALV)

The ALV experiment by Graham and Islam used a different angle of attack trajectory and was conducted at higher Reynolds numbers. The ALV angle of attack trajectory was a linear increase in angle of attack described by the reduced pitch rate.

$$K = \dot{\alpha} C / 2U_{\infty}$$

The sinusoidal angle of attack trajectory is described by the reduced frequency.

$$k = \frac{wc}{2V_{\infty}}$$

Comparisons can be made between the two experiments. The overall lift augmentation performance of the ALV was compared to a value of 0.8 of the maximum lift coefficient for the NACA 0012 airfoil. This factor was applied so that comparisons would be made to a value of lift coefficient that would be reasonable for sustained flight. Aircraft are rarely flown with their lifting surfaces at sustained maximum lift coefficient. To operate an aircraft in these conditions is very strenuous

for the pilot and invites imminent loss of control since this requires continuous operation at the airfoil critical angle of attack. Comparing the lift coefficient performance of the ALV to 0.8 of the maximum lift coefficient, the ALV had an augmented lift factor of 1.5 or 1.5 times 0.8 of the maximum static lift coefficient of the NACA 0012 airfoil. Graham and Islam do not consider whether or not the ALV needs to be operated at 0.8 of the maximum dynamic lift coefficient. At this time no work has been done to determine the sensitivity of an augmented lift device to variations in average angle of attack, i.e. is there a critical average angle of attack when considering the effects of dynamic lift?

If the dynamic lift results of the experiment that is subject of this paper were evaluated using the same criteria used by Graham and Islam, the resulting lift augmentation factor would be 1.18. In this case the data used for comparison is the static lift coefficient calibration diagram where a maximum lift coefficient of 1.4 was measured. The summary data plot shown above has a line plotted at a lift coefficient of 1.1 corresponding to 0.8 times the maximum lift coefficient of 1.4. This line is marked ALV in the diagram legend.

Comparison with static lift diagram measurements

Perhaps the most accurate means for evaluating the effects of dynamic lift is to compare the average lift coefficient from the dynamic tests with the average static lift coefficient of the test conducted for calibration. To accomplish this the static lift data

must be digitized and modified to appear as a function of crank angle, then integrated over the period and divided by the period, i.e. averaged. This was accomplished by formulating the calibration diagram as a piecewise linear function which was characterized by slope and y intercept for each curve segment measured from the data shown in figure 29. A small computer program was written to calculate the lift coefficient as a function of angle of attack for values from 5-25 degrees. The resulting information was written to a text file and then plotted in a spreadsheet application. The resulting plot is shown below in figure 30.

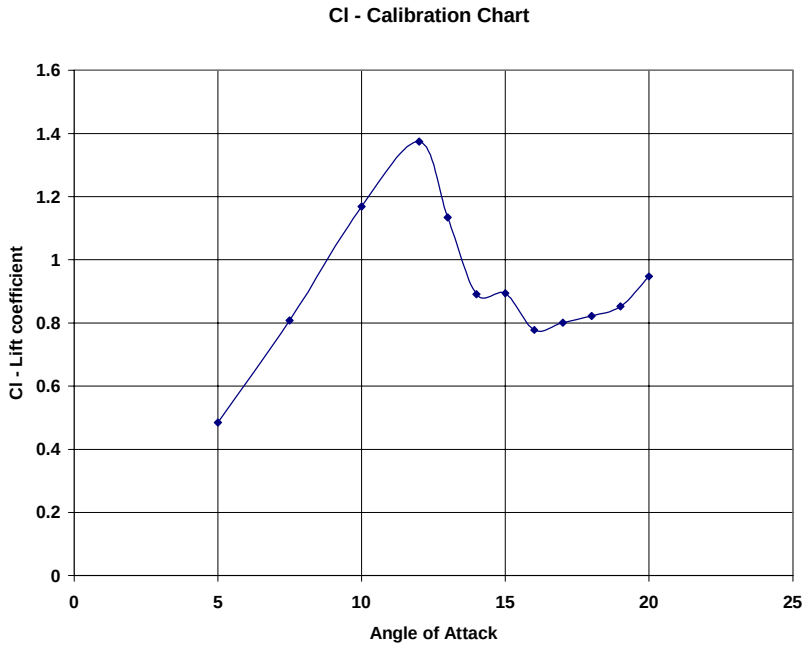

Figure 29, Calibration Plot, static lift conditions.

The crank angle algorithm described in appendix L was then added to the program. This function returns a value of angle of attack for a given crank angle.

Experiment

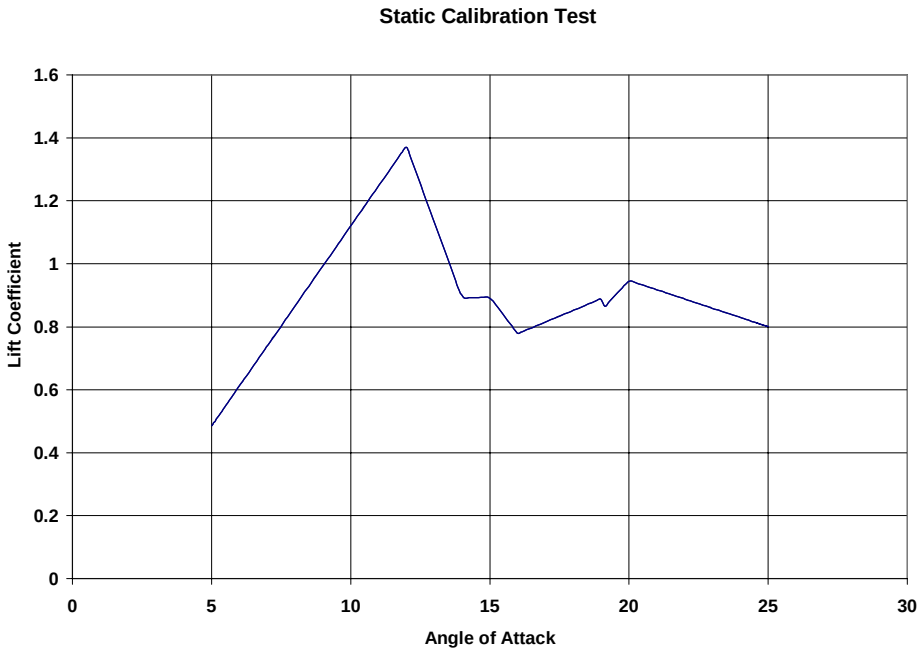

Figure 30, Piecewise, Static Calibration Plot

The crank angle function was then stepped through values of 0-360 degrees producing a value of angle of attack ranging from 5-25 degrees. The angle of attack determined by the crank angle function was then used to determine lift coefficient using the piecewise lift coefficient function. Values of lift coefficient were generated over a range of 0-360 degrees of simulated crank rotation. Data for lift coefficient corresponding to crank angle were recorded in a text file and plotted using a spreadsheet application. The resulting diagram is shown below in figure 31. Figure 31 is very similar to the diagram in figure 20 after being reflected at the 25 degree line.

Experiment

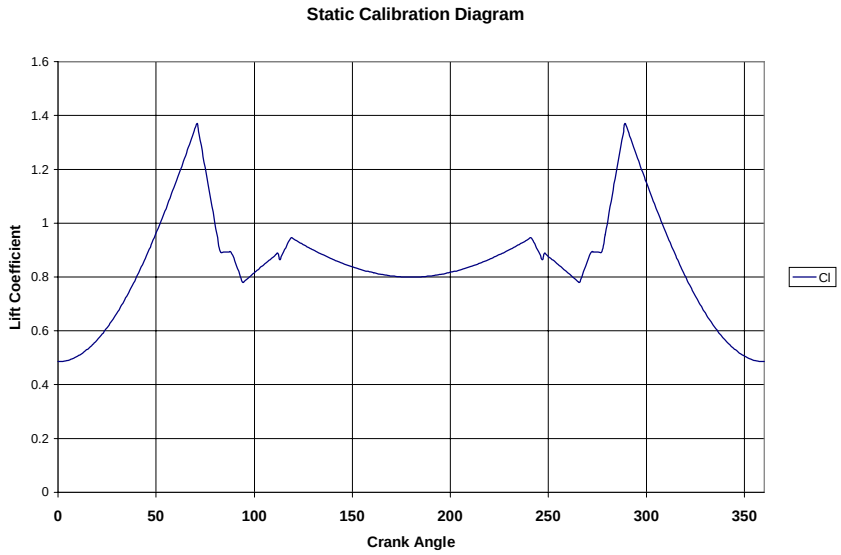

Figure 31, Lift Coefficient vs. Crank Angle generated from Piecewise Static Calibration Plot shown in figure 20.

The resulting average lift coefficient for this analysis was 0.8519. This value is probably too large.

The static test evaluation described above assumes that there is no hysteresis in the lift coefficient of an airfoil even at static or near static conditions. In reality the lift coefficient curve that is the result of increasing the airfoil AOA is not completely retraced as the AOA is decreased. Usually, with increasing AOA, once past the critical AOA the lift coefficient drops to a value that remains relatively constant. As AOA is then decreased the lift coefficient curve does not trace back over the peak again but straight back to the left until it intersects the initial positive slope portion of

the diagram. The degree of hysteresis is airfoil dependent. Some airfoils are much more tolerant to these conditions than others and will reattach at higher AOA values. The evaluation made of the static calibration data does not account for this hysteresis. In this sense it is optimistic and the value shown above is probably too large. The plots of the Calibration Crank angle Diagram are symmetrical about the x-axis at 180 degrees. Generally the peak at the right of the diagram would not exist for real data.

Comparison with McCroskey and McAlister

The work of McCroskey and McAlister examined the NACA 0012 airfoil at Reynolds numbers of approximately 2.5 x 10^6, reduced frequencies of 0.004 through 0.25 and an AOA trajectory of 15+10sin(wt). The dramatic increase in lift coefficient at high angles of attack that was so characteristic of McCroskey and McAlister's work was not apparent in the tests done herein at Reynolds numbers below 500,000. McCroskey and McAlister conducted three tests at a Reynolds number of 490,000 and AOA trajectory of 10+10sin(wt), and at reduced frequencies of k=0.104, k=0.151 and k=0.253. These tests did show a similar shape to the tests herein, however the tests herein did not reach the same lift coefficient values of McCroskey and McAlister. There are similarities in the two sets of data however a quantitative comparison does not seem possible. The lift coefficient vs. AOA diagrams of McCroskey and McAlister are similar to the data of the experiment herein primarily in that they exhibit significant hysteresis. The average AOA of McCroskey and McAlister's tests at Re =490,000 was 5 degrees less that the average AOA of the

experiment herein. This very likely had significant effects on the shape of the lift coefficient vs. AOA diagram. Significant similarities exist between the lift coefficient vs. angle data. Both sets of data have a similar shape that makes the same change in shape as the reduced frequency is increased. Examining the lift coefficient vs. angle diagram from McCroskey's data at k=0.104, see figure 32 below, two pronounced peaks are very noticeable.

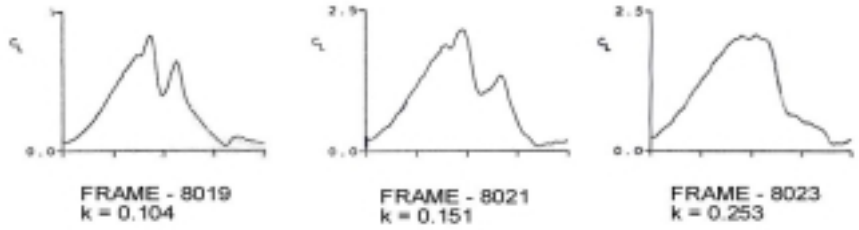

Figure 32, Lift Coefficient vs. Crank Angle, McCrosky, NASA

Examining the same diagram for the data taken at k=0.151 and k=0.253 it can be seen that the pronounced peaks become smaller and then combine to become one large hump. This same trend can be seen in the data from the experiment herein. Shown below in figure 33 are four lift coefficient vs crank angle diagrams.

Experiment

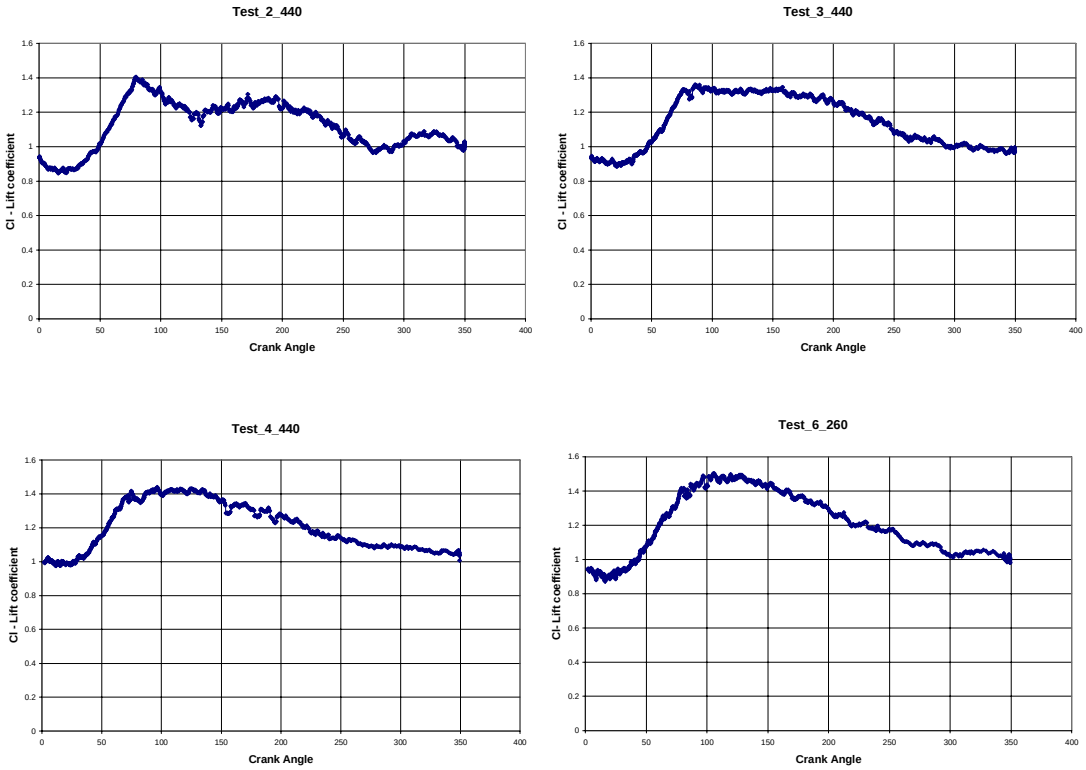

Figure 33, Tests 2-440, 3-440, 4-440, 6-260, showing coalescing of peaks in Lift Coefficient vs. Crank Angle diagrams

Test 2_440 at a Reynolds number of 440,000 and k=0.02 has the most pronounced pair of peaks. These peaks disappear as the reduced frequency and Reynolds number is increased. First the valley between the peaks disappears and the first peak becomes dominant. With further increasing Reynolds number and reduced frequency the curve becomes more rounded and becomes one large hump. This hump is best seen in test 6_260 and the data of McCroskey and McAlister for k=0.253. It is the belief of the writer that this behavior is primarily the result of the vortex shed from the leading edge of the airfoil and the manner in which it travels over the airfoil.

Experiment

Comparison with work of Weber

The work of Weber examined the dynamic characteristics of the NACA 4418 airfoil using an ultrasonic circulation-measuring device to determine the lift of the airfoil during dynamic testing. These tests were conducted in the same wind tunnel as the experiment herein however the standard tunnel test section was used and the airfoil was support from the tunnel walls rather than the roof and floor as in the experiment herein. These tests were conducted at Reynolds number between 500,000 and 800,000. The NACA 4418 airfoil is a cambered airfoil unlike the NACA 0012 symmetrical form. The chord of the airfoil was approximately 12 inches and the airfoil was pivoted at the 40% chord point. These conditions do not correspond to the conditions of the experiment herein. Further, Weber's experiment included angle of attack trajectories that encompassed a wider range of angle of attack, alpha=9+20sin(wt) compared with a trajectory of alpha=10+15sin(wt) for the experiment herein. There are some notable differences in the results of the two experiments. First the maximum dynamic lift coefficients found by Weber were significantly larger than those found in the experiment herein. Further the lift coefficient diagrams show a large peak at the highest angle of attack that sometimes extends to 2-3 times the static maximum lift coefficient. This form corresponds to data from the work of McAlister. In Weber's experiment the large peak in lift coefficient occurred at approximately 27-28 degrees AOA. The airfoil AOA of the experiment herein did not extend beyond 25 degrees. The NACA-4418 airfoil is a

cambered airfoil with a zero lift line of approximately –4 degrees. At an AOA of zero the lift coefficient of the NACA-4418 is roughly equivalent to the lift coefficient of the NACA-0012 airfoil at an AOA of 4 degrees. Making a rough comparison between the two experiments, the experiment by Weber is probably equivalent to an NACA-0012 AOA trajectory of alpha=13+20sin(wt) which exceeds the maximum AOA of the experiment herein by 8 degrees.

It is the belief of the writer that the 8-degree difference in maximum AOA and the effects of the unsteady and momentum terms likely accounts for the absence of the spike in dynamic lift coefficient seen in the data from Weber and McAlister. The effect of the unsteady term is to absorb the pressure spike within the flowfield rather than it being present at the control volume boundary.

Conclusions

Data for all tests conducted were plotted, average lift coefficient vs. reduced frequency, for each value of Reynolds number.

Average lift increased as a function of increased reduced frequency, although the increase was not monotonic. The average lift coefficient for every Reynolds number tested exceeded the average static lift for the NACA-0012 airfoil as reduced frequency was increased. A maximum average lift coefficient augmentation of 1.18 was achieved at Re=200,000 and k=0.2. The increase in average lift coefficient was a result of the lift coefficient remaining at the static lift maximum value far beyond the point in the cycle where the critical angle of attack was reached, before diminishing. A large peak in the lift coefficient was not observed. This determination should be viewed cautiously considering the influence of the unsteady and momentum terms and their effect on the measured lift coefficient.

The data suggest an optimum or local optimum value for reduced frequency. The summary data plot showed a peak in average lift coefficient for Re of 200,000 and 260,000. These two peaks were out of phase in a way that suggested some event took place at the same chordwise point along the airfoil during testing. This suggests that it may be possible to tune the reduced frequency to obtain a maximum average lift coefficient.

Experiment

The evaluation of the momentum theory in section 3 above, points to the importance of the time derivative term of the momentum equation. Examining the data, as the reduced frequency was increased, the slope of the lift curve remained constant and equal to the slope of the static lift curve until a rotational frequency of 23 Hz. was reached. From 23 Hz. to the maximum value measured of 28 Hz. the slope of the lift curve diminished by 13%. The AOA was measured with a rotary transducer and hence independently of any aerodynamic effects. The reduction in lift curve slope at frequencies above 23 Hz. must have been a result of a reduction in lift coefficient, likely due to the time derivative term of the momentum equation. Since the slope of the lift curve remained constant up to the frequency of 23 Hz., the data in this range was not effected by the derivative term of the momentum equation. Limitations in the oscillating mechanism prevented running at rotational frequencies in excess of 30 Hz., however, this observation brings into question the viability of making lift measurements at higher rotational frequencies.

The other term of the momentum equation that may have an effect on measurement accuracy is the term that describes momentum escaping the control volume. This is examined in section 3 above. The most noticeable flow structures escaping the control volume have been observed from the data of other investigators. Large vortices leave the airfoil after the vortex shedding phase of dynamic stall. These

structures seem to flow downstream with little movement orthogonal to the free stream flow. The flow within the structures is rotational and hence there is no net flow orthogonal to the free stream flow. The flow escaping the control volume should have little effect on the lift measurement.

The work of McCroskey and McAlister indicated that the effects of Reynolds number was small at low Mach numbers. The results of this experiment show that the effect of Reynolds number is significant at Reynolds numbers below 500,000. For a given value of reduced frequency, increasing Reynolds number has the effect of reducing the AOA where the critical AOA breakpoint occurs. As reduced frequency is increased for a given Reynolds number the value of the lift coefficient after the breakpoint increases. Increasing Reynolds number causes the critical AOA breakpoint to occur sooner in the cycle while increasing the reduced frequency causes the lift coefficient after the breakpoint to increase, in some cases the lift coefficient will continue to increase after the critical AOA breakpoint almost to the maximum AOA. The result is to increase the portion of the cycle during which a high lift coefficient is sustained. The final effect is to increase the overall average lift coefficient of the airfoil.

5 Future Work

Future work should include the testing of other airfoils in the NACA/NASA airfoil family. Comparisons should be made between airfoils with abrupt stall characteristics such as the NACA-0009 and airfoils with forgiving stall characteristics to determine if the static stall characteristics are an indicator of dynamic stall behavior.

Due to limitations in the maximum tunnel speed, tests were limited to a maximum Reynolds number of 500,000. Future work should include investigations at higher Reynolds numbers. This will require manufacturing a larger test airfoil and increasing the maximum tunnel speed.

With the manufacture of a new and larger airfoil model the transducers may be moved to the inside of the model for direct measurement of airfoils surface pressures. This will permit a direct comparison between the technique of lift measurement by measuring tunnel wall pressure and the more conventional method of measuring surface pressures on the model. Also comparisons may be made with the work of Weber by concurrently using an ultrasonic circulation meter.

Future Work

A new airfoil has recently been developed for quiet propellers. This airfoil has a double camber top surface. Testing this airfoil may provide further understanding of dynamic stall.

To date, all experiments for dynamic stall have rotated the airfoil at the ¼ chord point. Significant differences in dynamic airfoil behavior may exist as the point of rotation is moved toward or away from the leading edge. A systematic study of various rotation points could produce valuable information.

In future tests AOA trajectories with greater range should be done. In the experiment herein the AOA trajectory remained fixed at alpha=15+10sin(wt).

Before proceeding with further tests the turbulence spectrum of the WPI open tunnel should be measured. The effect of turbulence on models of the sizes used in this experiment should be investigated.

Most experiments have concentrated on varying the AOA over trajectories represented by some form of periodic function. Improved average lift performance may be obtained by using some form of control system with feedback to control the AOA. Success of this endeavor will depend upon the development of an appropriate control algorithm and a sensor that can detect the state of flow over the airfoil.

Future Work

Endnotes

---

[1] Farren, W.S. Air Ministry Aeronautical Research Committee Reports and Memoranda No. 1648 R&M 1648
[2] Graham G. M. and Islam, M Time Average Loading on a Two-Dimensional Airfoil in Large Amplitude Motion, AIAA, Journal of Aircraft, Vol. 29, No. 4
[3] McAlister, K.W., Carr, L.L. & McCroskey, W.J. "Dynamic Stall Experiments on the NACA-0012 Airfoil". NASA Tech Paper 1100[1978]
[4] Kuethe, A. M., Chow, CY, Foundations of Aerodynamics, John Wiley & Sons, New York 4th edition. Pg 85
[5] Kuethe, pg 85
[6] Keuthe, A. M., Schetzer, J. D., Foundations of Aerodynamics, John Wiley & Sons, 2nd edition pg 73
[7] McCroskey, L. W., Carr, L.W., McAlister, K.W., "Dynamic Stall Experiments on Oscillating Airfoils", AIAA Journal, Vol. 14, No. 1, January 1976
[8] McCroskey, K. W., McAlister, K. W., McAlister, K. W., Carr, L. W., & Pucci, S. L. "An Experimental Study of Dynamic Stall on Advanced Airfoil Sections" NASA-TM-84245[1982]
[9] Johnson, W. Helicopter Theory, Princeton University Press, Pg. 198-199
[10] McCroskey, W. J. "Unsteady Airfoils", Annual Review of Fluid Mechanics, 1982. 14:285-311
[11] Abbott, I. H., Von Doenhoff, A. Theory of Wing Selections, Dover, New York. Pg. 125
[12] Von Doenhoff, A., Abbott, F. T., "The Langley Two-Dimensional Low-Turbulence Pressure Tunnel", NACA-TN-1283, Washington, May 1947
[13] Witoszynski, C. & Thompson, M.J. "The Theory of Single Burbling" Aerodynamic Theory Vol. 3, Division F, W. F. Durand, Editor in Chief
[14] Sears, W. R., "Unsteady Motion of Airfoils with Boundary-Layer Separation", AIAA Journal, Vol. 14, No. 2 July 1976
[15] Sears, W.R., "Some Recent Developments in Airfoil Theory", Journal of the Aeronautical Sciences, May 1956
[16] McCullough, Gault, "Examples of Three Types of Airfoils-Section Stall at Low Speeds" NACA-TN-2502, Sept 1958
[17] Selig, M.S., Donovan J. F., Fraser D. B., Airfoils at Low Speeds, Soartech 8, H. A. Stokely 1989
[18] Rae, W. H., Pope, A., Low-Speed Wind Tunnel Testing, 2nd edition, John Wiley and Sons, New York, Pg. 354
[19] Rae, W. H., Pg. 356
[20] Rae, W. H., Pg. 360
[21] McCroskey, McAlister, Carr, "Experimental Study of Dynamic Stall on Advanced Airfoil Sections", NASA-TM-84245 Vol. I-III, Sept 1982
[22] Weber, F. J., "Ultrasonic Circulation Meter for Determining of Circulation About a Rapidly Pitching Airfoil, MS Thesis Worcester Polytechnic Institute, March 1994

Bibliography

Abbott, I.H., Von Doenhoff, A. Theory of Wing Sections, Dover, New York

Eskinazi, S. Vector Mechanics of Fluids and Magnetofluids, Academic Press, New York, 1967

Farren, W. S. Air Ministry Aeronautical Research Committee Reports and Memoranda No. 1648, R & M 1648

Graham, G.H. and Islam, M. "Time Average Loading on a Two Dimensional Airfoil in Large Amplitude Motion", AIAA Journal of Aircraft, Vol.29. No.4

Johnson, W. Helicopter Theory, Princeton University Press

Keuthe, A.M., Chow, CY, Foundations of Aerodynamics, John Wiley & Sons, New York 4th edition

Keuthe, A.M., Schetzer, J.D., Foundations of Aerodynamics, John Wiley & Sons, New York 2nd edition

McCroskey, K.W., Carr, L.W., McAlister, K.D., "Dynamic Stall Experimentson Oscillating Airfoils", AIAA Journal, Vol. 14. No. 1 January 1976

McAlister, K. W., Carr, L.W. McCroskey, K.W. "Dynamic Stall Experiments on the NACA-0012 Airfoil", NASA Tech Paper 1100 [1978]

McCroskey, K.W., McAlister, K.W., Carr, L.W., Pucci, S.L. "An Experimental Study of Dynamic Stall on Advanced Airfoil Sections", NASA-TM-84245 [1982]

McCroskey, K.W., "Unsteady Airfoils", Annual Review of Fluid Mechanics, 1982. 14:285-311

McCullough, Gault, "Examples of Three Types of Airfoils-Section Stall at Low Speeds", NACA-TN-2502, Sept 1958

Rae, W.H., Pope, A., Low Speed Wind Tunnel Testing, 2nd Edition, John Wiley and Sons, New York.

Sears, W. R. , "Unsteady Motion of Airfoils with Boundary-Layer Separation", AIAA Journal, Vol. 14, No. 2, July 1976

Selig, M.S., Donovan J.F., Fraser D.B., Airfoils at Low Speeds, Soartech 8, H.A. Stokely 1989

Von Doenhoff, A., Abbott, E.F., "The Langley Two-Dimensional Low-Turbulence Pressure Tunnel", NACA-TN-1283, Washington, May 1947

Weber, F. J. "Ultrasonic Circulation Meter for Determining of CirculationAbout a Rapidly Pitching Airfoil", MS Thesis, Worcester Polytechnic Institute, March 1994

Witoszynski, C. & Thompson, M. J. "The Theory of Single Burbling" Aerodynamic Theory Vol. 3, Division F, W. F. Durand, Editor in Chief

Zucrow, M. J., Hoffman, J. D., Gas Dynamics, Vol. 1, Vol. 2, John Wiley & Sons, New York 1976

6 Appendices

Appendix A: Summary Data Plots

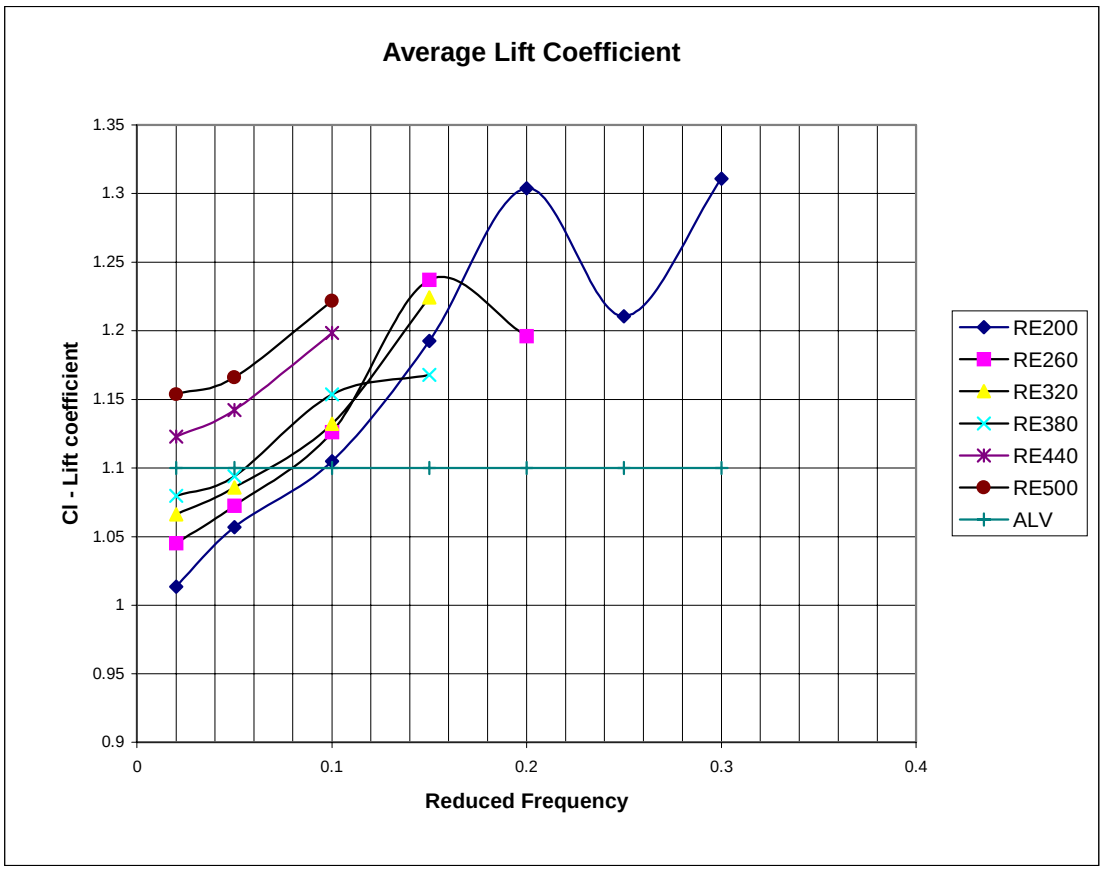

Above Lift Coefficient is plotted vs. Reduced Frequency. Lines are lines of constant Reynolds Number.

Appendices

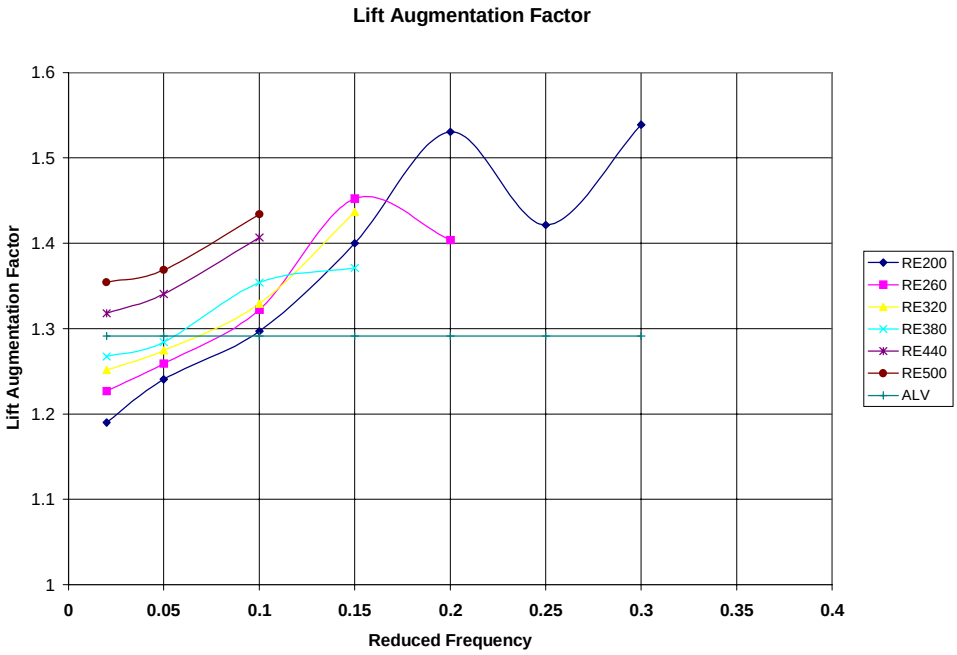

Above, Lift Augmentation Factor is plotted vs. Reduced Frequency. Lines are lines of equal Reynolds Number. The Average Static Lift Coefficient used is .8519.

Appendices

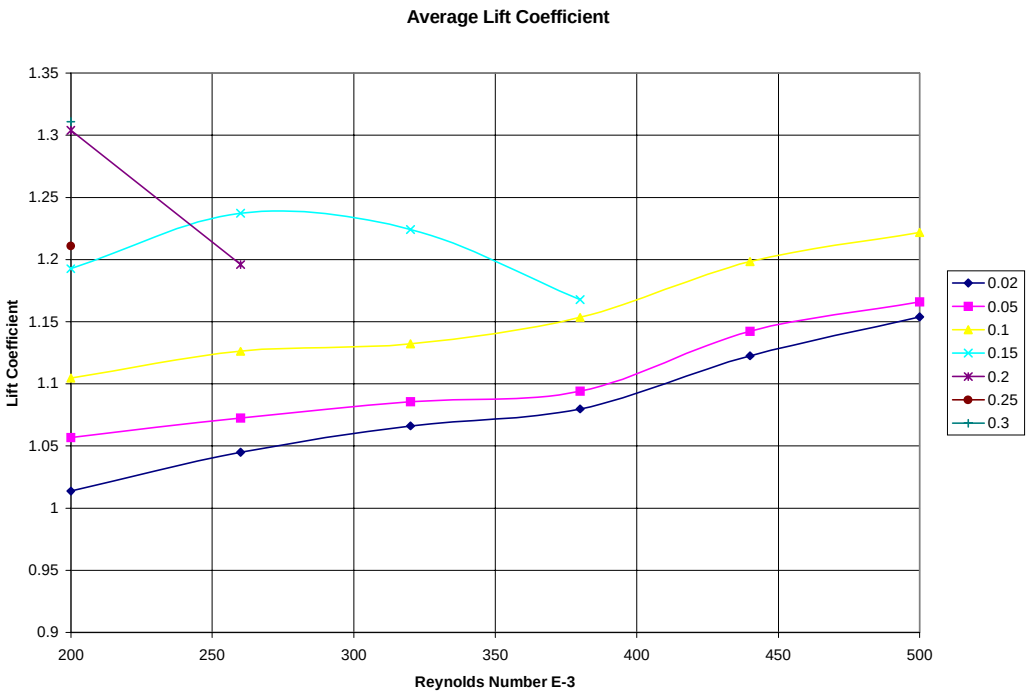

Above Average Lift Coefficient is plotted vs. Reynolds Number. Lines are lines of constant Reduced frequency.

Appendices

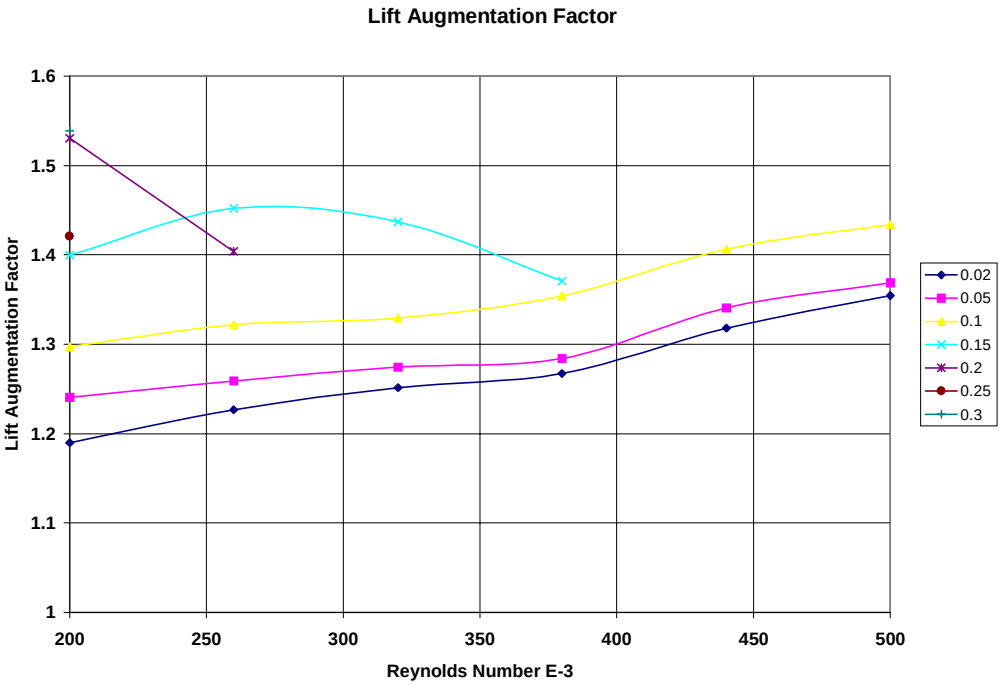

Above, Lift Augmentation Factor is plotted vs. Reynolds Number. Lines are lines of constant reduced frequency. The Average Static Lift Coefficient used is .8519.

Appendices

Appendix B: Data Plots

Test Summary Table

Airfoil NACA-0012
Trajectory 15+10sin(wt)

Test	Re	k	Hz.	Remarks
2_200	2.00E+05	0.02	1.88	Minimal dynamic effects
2_260	2.60E+05	0.02	2.44	Minimal dynamic effects
2_320	3.20E+05	0.02	3.00	Minimal dynamic effects
2_380	3.80E+05	0.02	3.57	Minimal dynamic effects
2_440	4.40E+05	0.02	4.14	Small lift increase beyond critical AOA
2_500	5.00E+05	0.02	4.70	Small lift increase beyond critical AOA
3_200	2.00E+05	0.05	4.70	Max Cl extends beyond critical AOA
3_260	2.60E+05	0.05	6.11	Max Cl extends beyond critical AOA
3_320	3.20E+05	0.05	7.52	Max Cl extends beyond critical AOA
3_380	3.80E+05	0.05	8.93	Max Cl extends beyond critical AOA
3_440	4.40E+05	0.05	10.34	Max Cl extends beyond critical AOA
3_500	5.00E+05	0.05	11.75	Max Cl extends beyond critical AOA
4_200	2.00E+05	0.1	9.40	Max Cl extended and higher after critcal AOA
4_260	2.60E+05	0.1	12.22	Max Cl extended and higher after critcal AOA
4_320	3.20E+05	0.1	15.04	Max Cl extended and higher after critcal AOA
4_380	3.80E+05	0.1	17.86	Max Cl extended and level after critcal AOA
4_440	4.40E+05	0.1	20.68	Max Cl extended and level after critcal AOA
4_500	5.00E+05	0.1	23.50	Max Cl extended. Large variations in Cl after critical AOA

Appendices

Test Summary Table Continued

Airfoil **NACA-0012**
Trajectory **15+10sin(wt)**

Test	Re	k	Hz.	Remarks
5_200	2.00E+05	0.15	14.10	Max Cl extended. Large variations in Cl after critical AOA
5_260	2.60E+05	0.15	18.33	Max Cl extended past critcal AOA, Cl curve more rounded at top
5_320	3.20E+05	0.15	22.56	Max Cl extended past critcal AOA, Cl curve
5_380	3.80E+05	0.15	26.79	Max Cl extended past critcal AOA, Cl curve breaks sharp at max Cl
6_200	2.00E+05	0.2	18.80	Max Cl past critcal AOA, slope rolls off, uneven after max Cl
6_260	2.60E+05	0.2	24.44	Max Cl past critcal AOA, slope rolls off, rolls down after max, uneven at top
7_200	2.00E+05	0.25	23.50	Max Cl past critical AOA, lower slope of Cl curve. Rounded up to max and past
8_200	2.00E+05	0.3	28.20	Max Cl past critcal AOA, lower slope of Cl curve, rounded up to max and past, uneven at top

Appendices

Test_2_200: Re=200,000, k=0.02

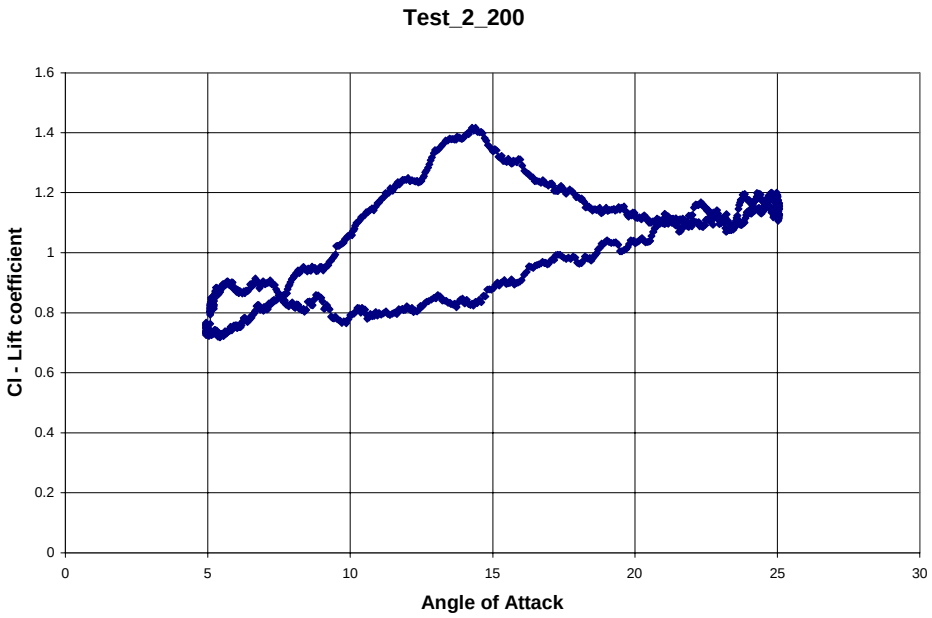

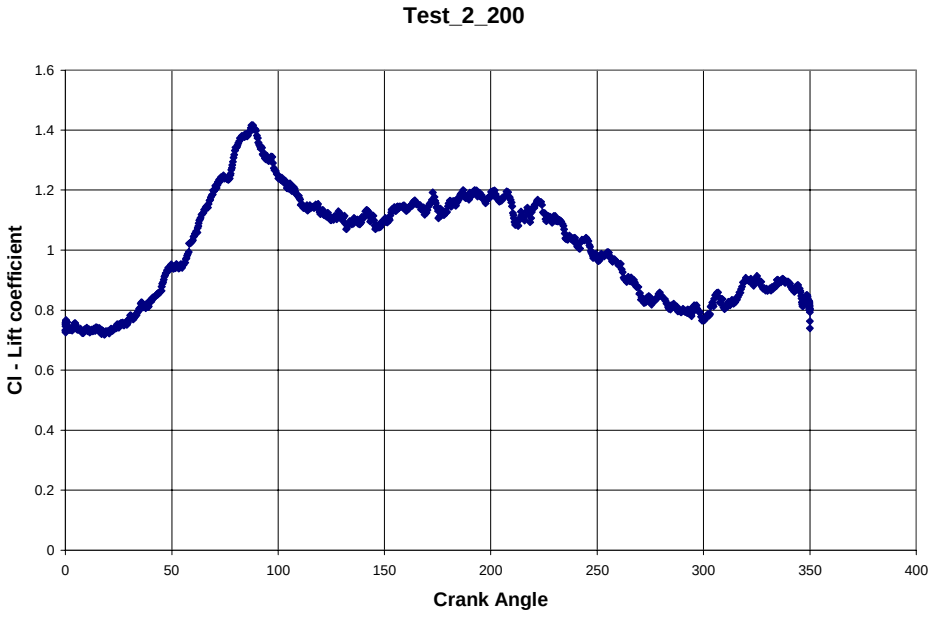

Appendices

Test_2_260: Re=260,000, k=0.02

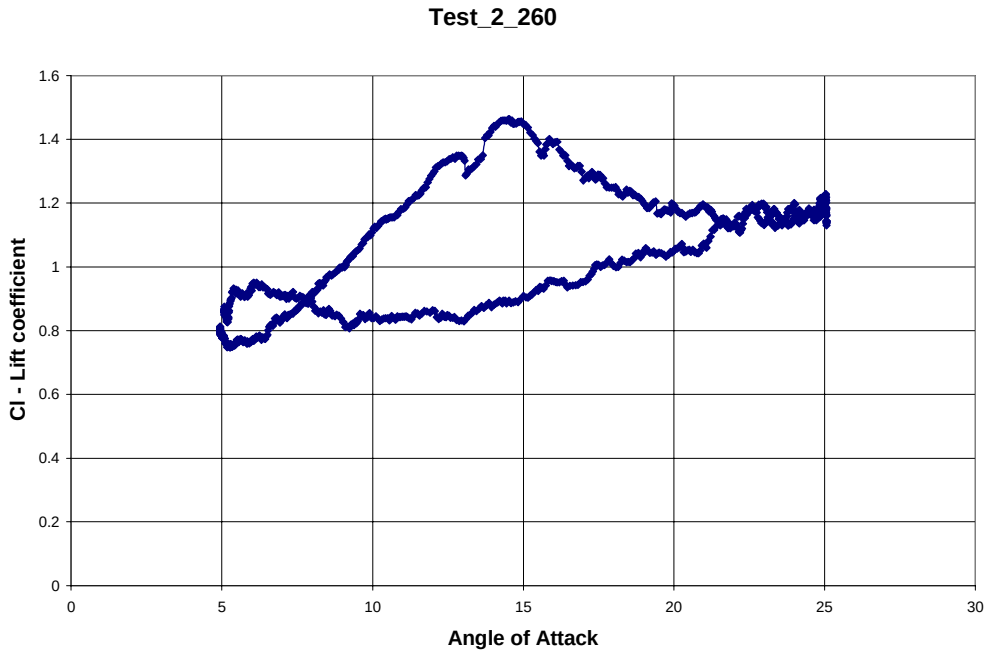

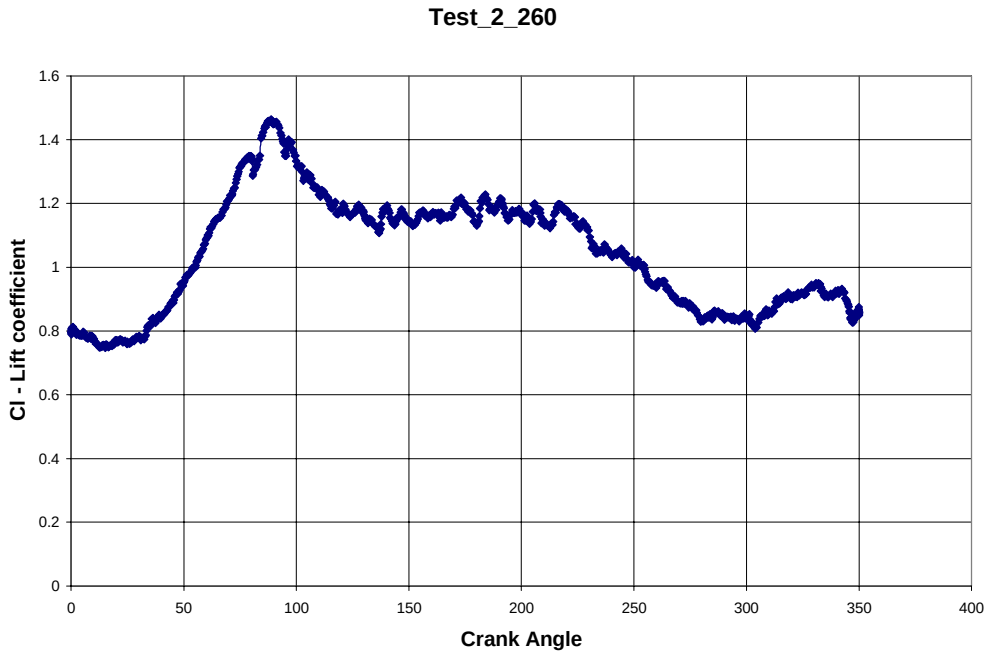

Appendices

Test_2_320: Re=320,000, k=0.02

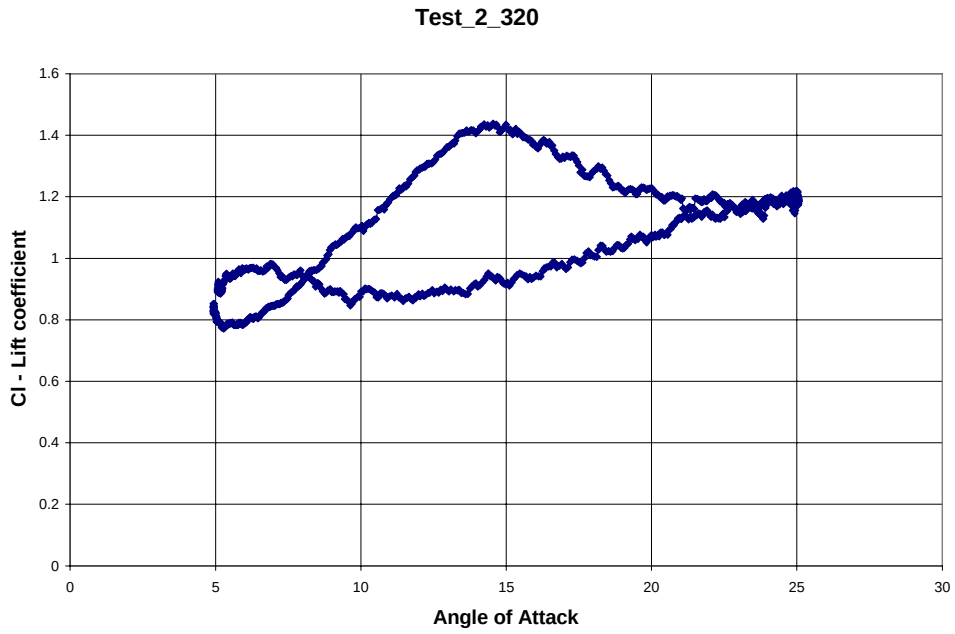

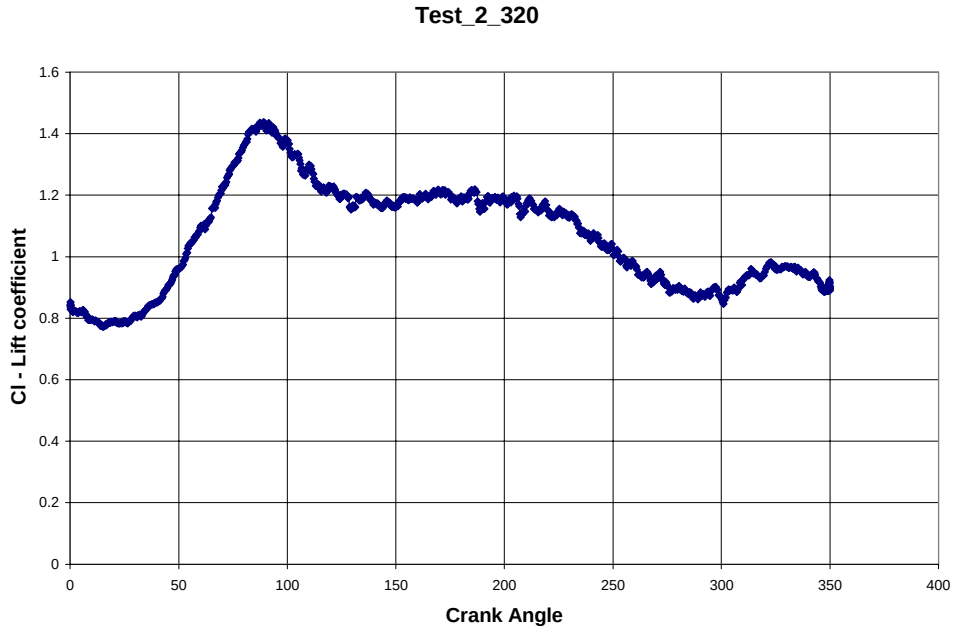

Appendices

Test_2_380: Re=380,000, k=0.02

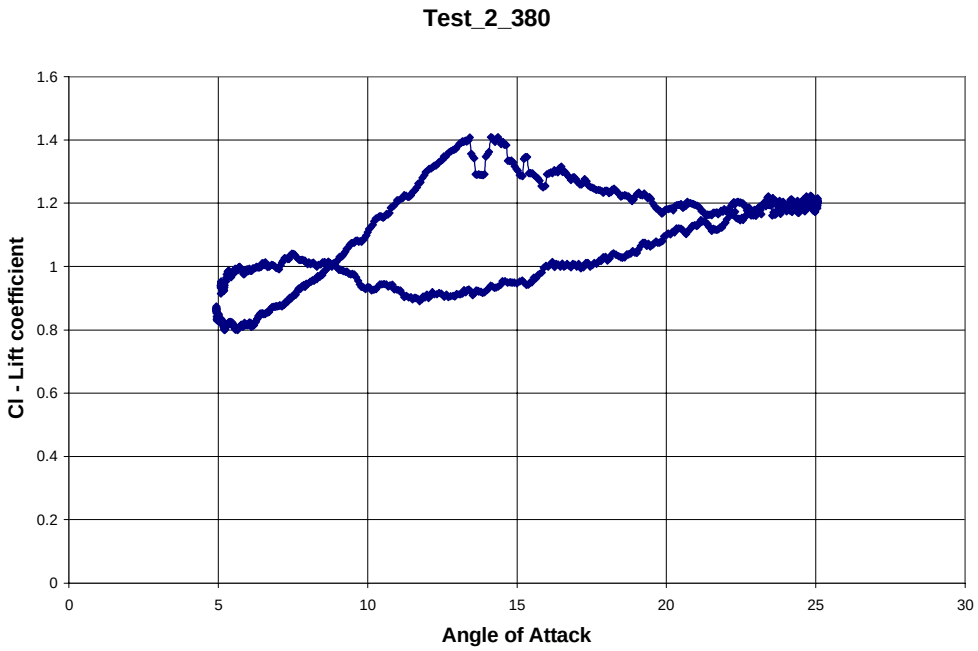

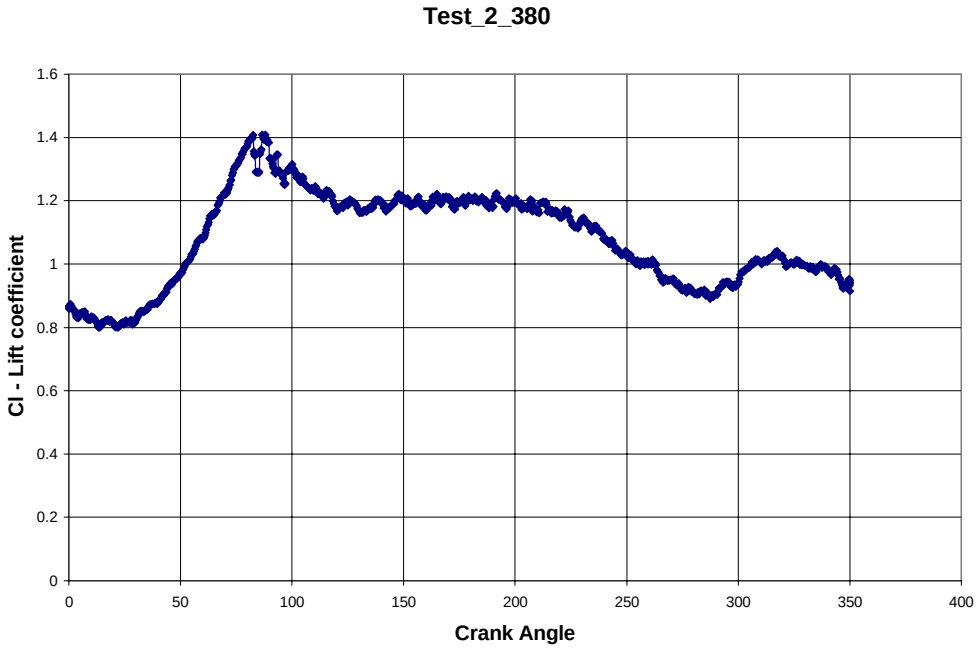

Appendices

Test_2_440: Re=440,000, k=0.02

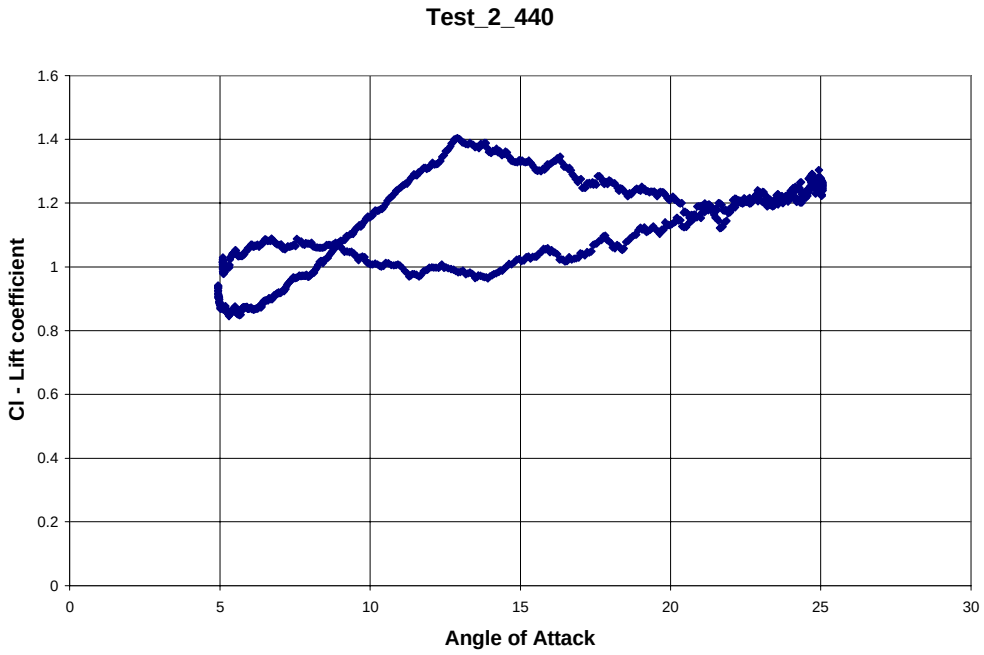

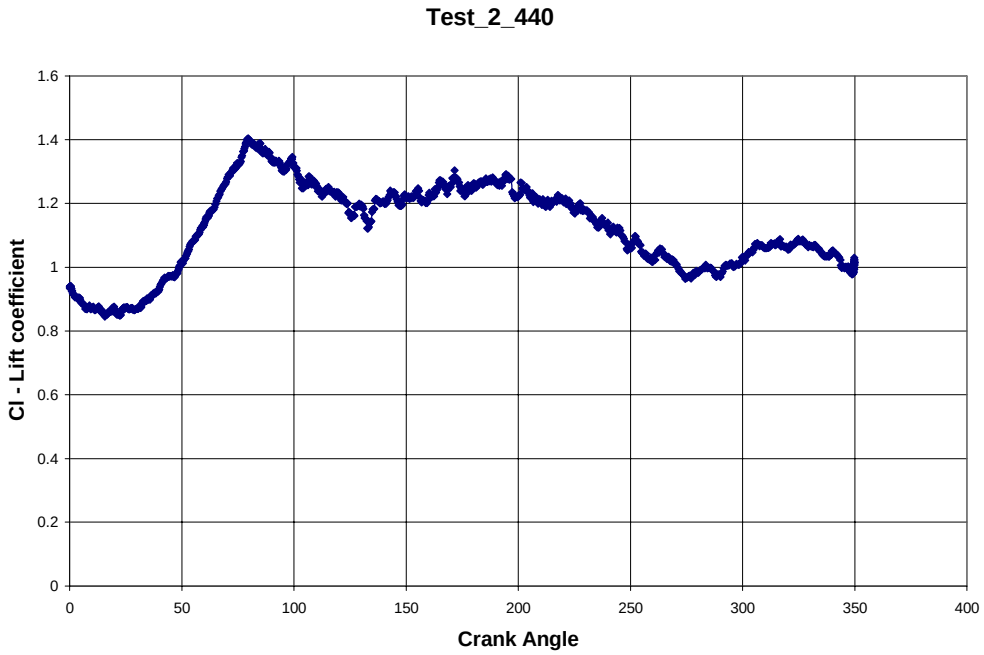

Appendices

Test_2_500: Re=500,000, k=0.02

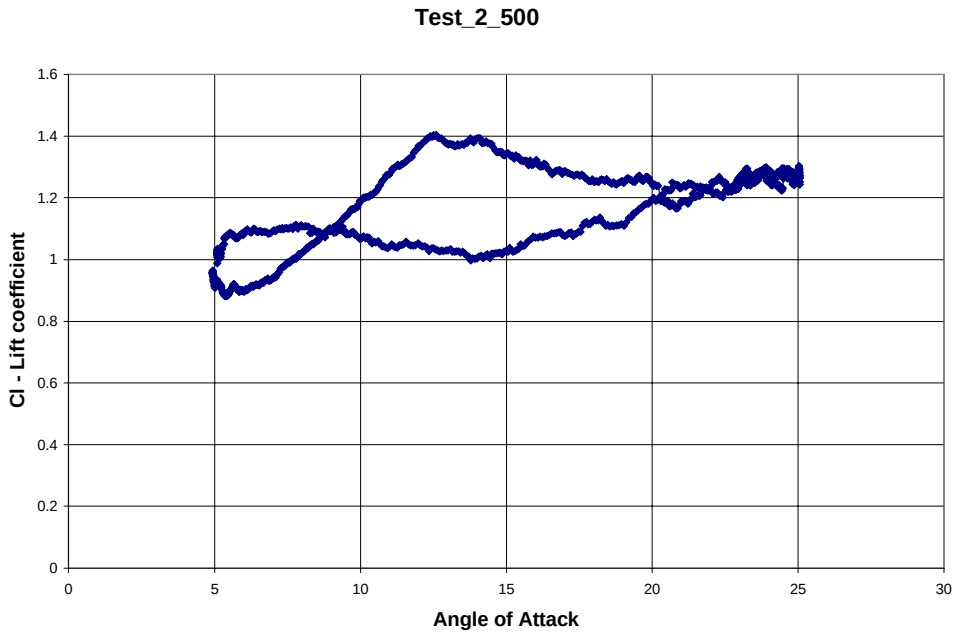

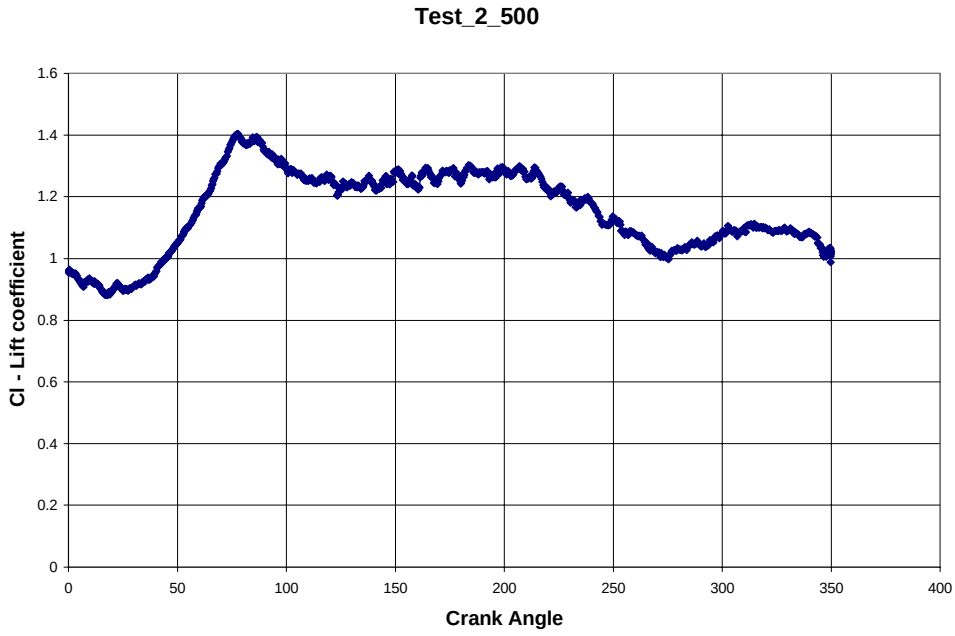

Appendices

Test_3_200: Re=200,000, k=0.05

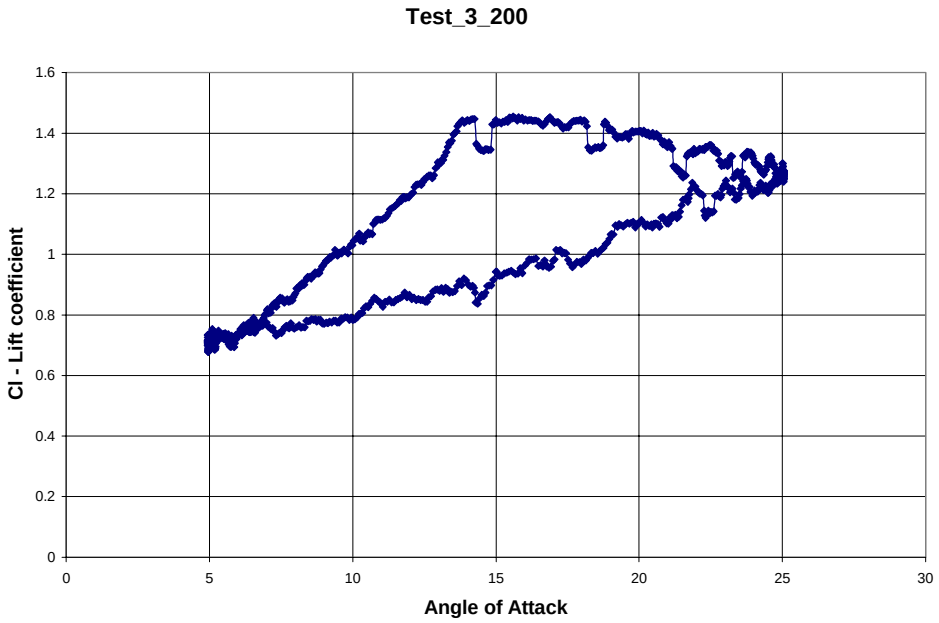

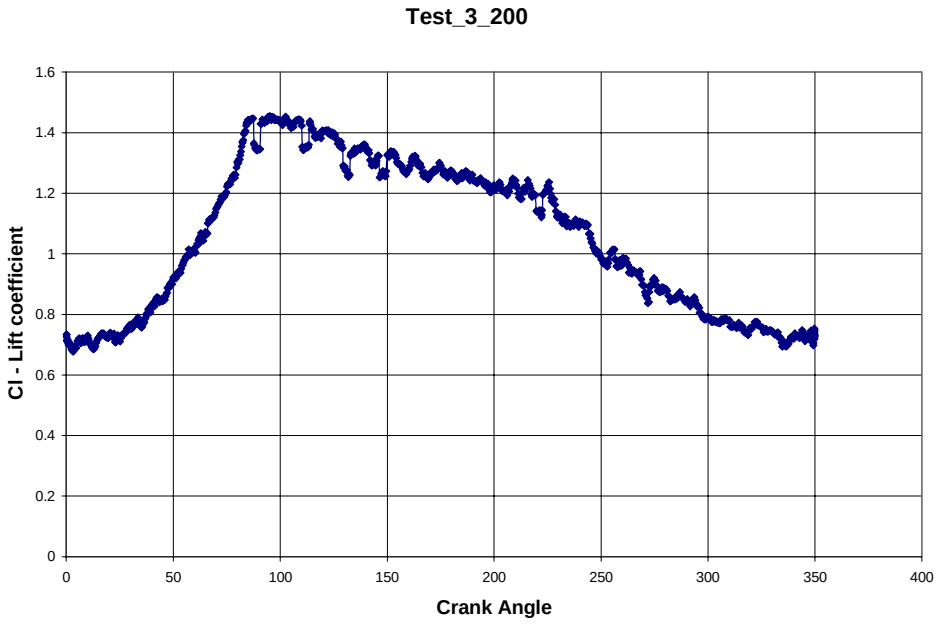

Appendices

Test_3_260: Re=260,000, k=0.05

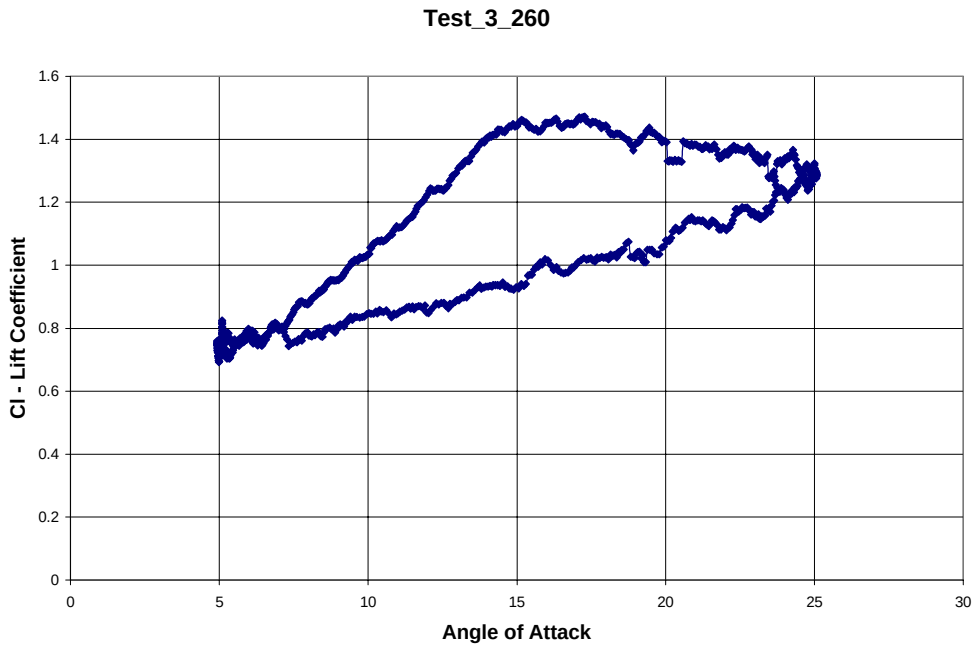

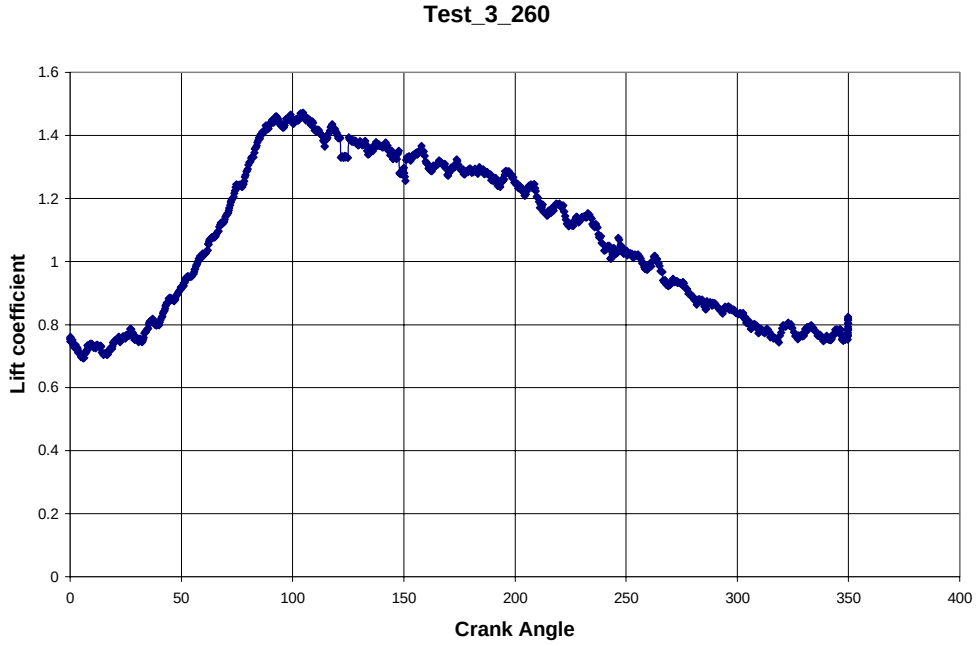

Appendices

Test_3_320: Re=320,000, k=0.05

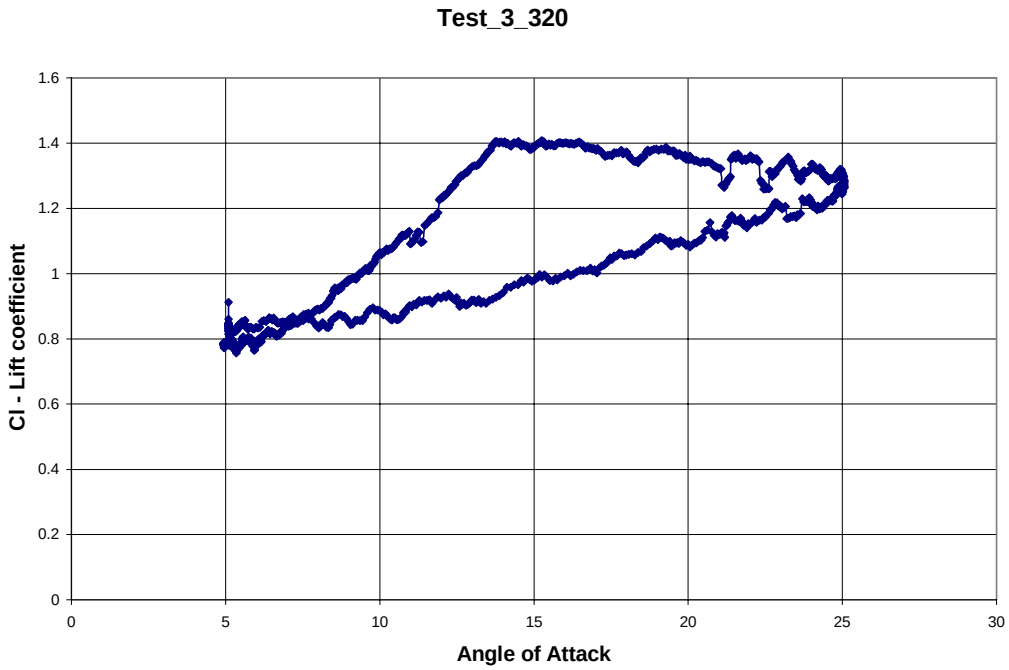

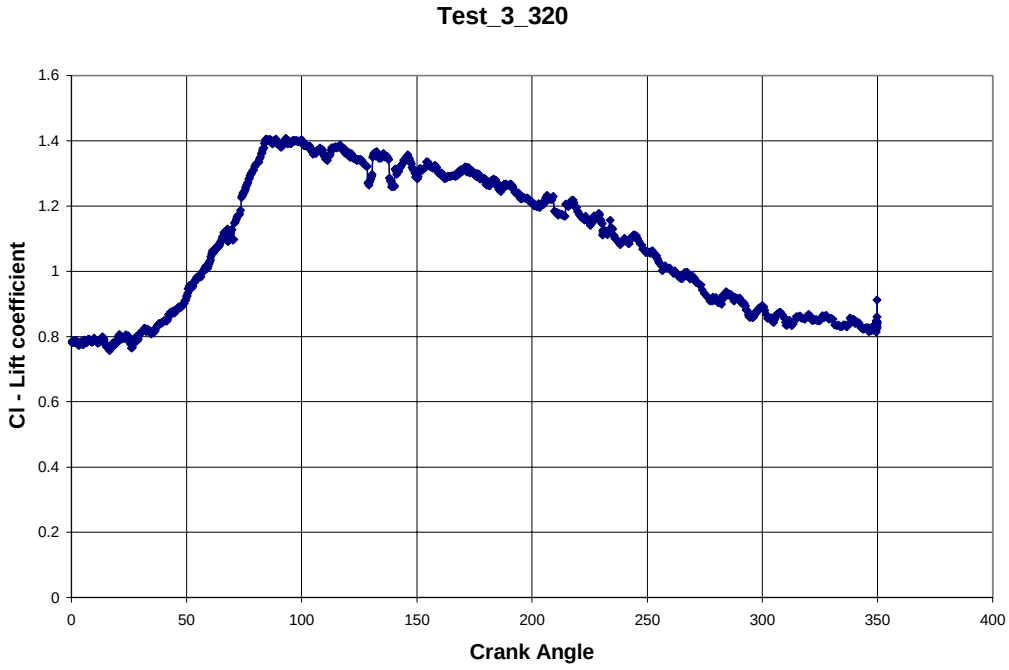

Appendices

Test_3_380: Re=380,000, k=0.05

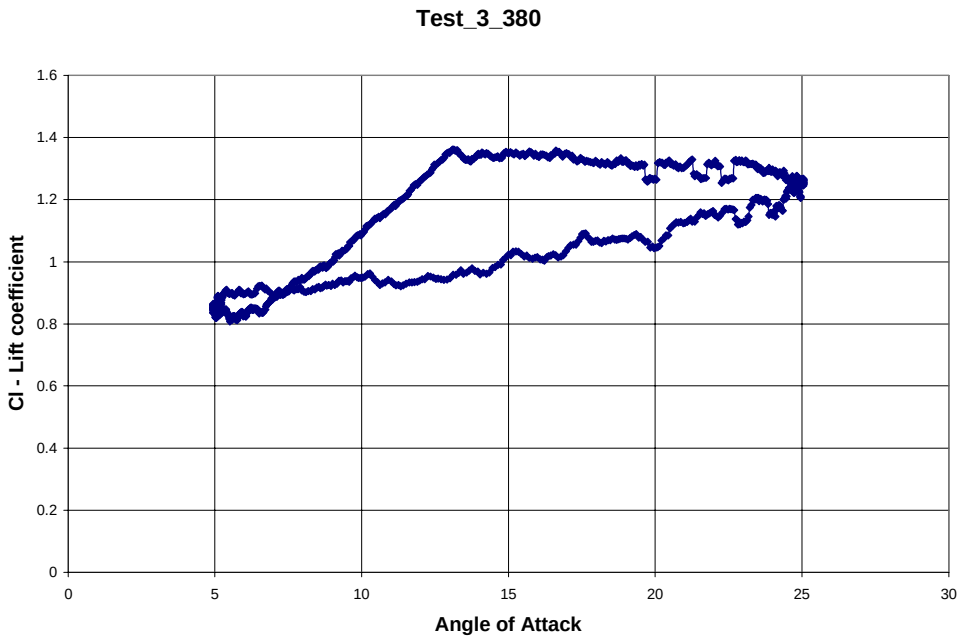

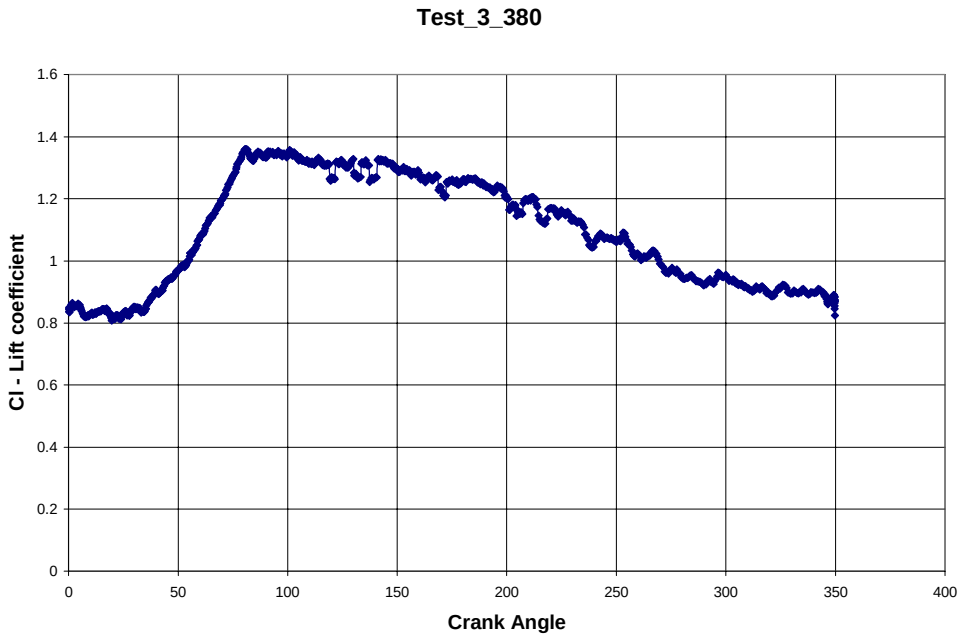

Appendices

Test_3_440: Re=440,000, k=0.05

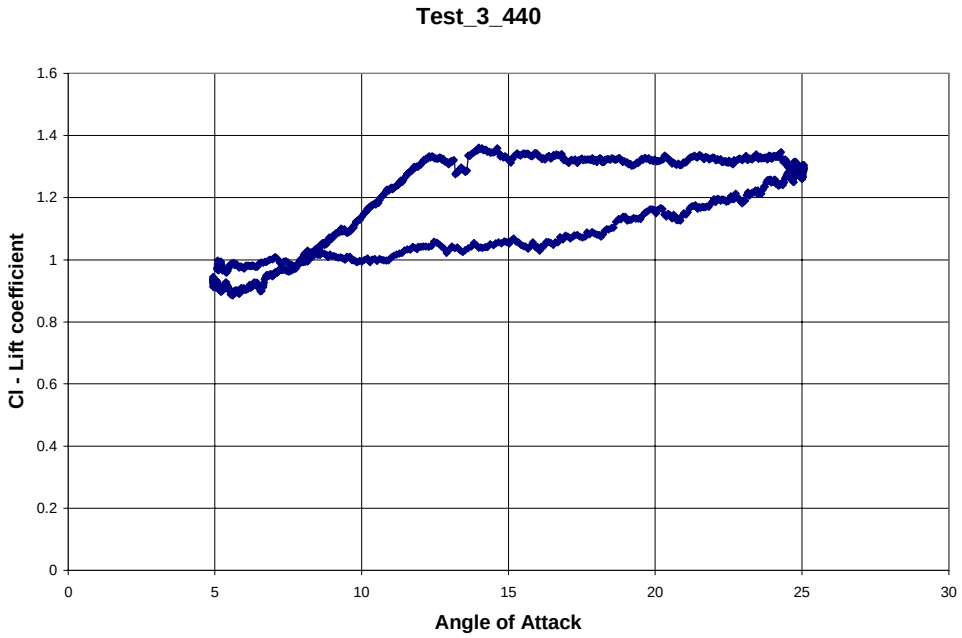

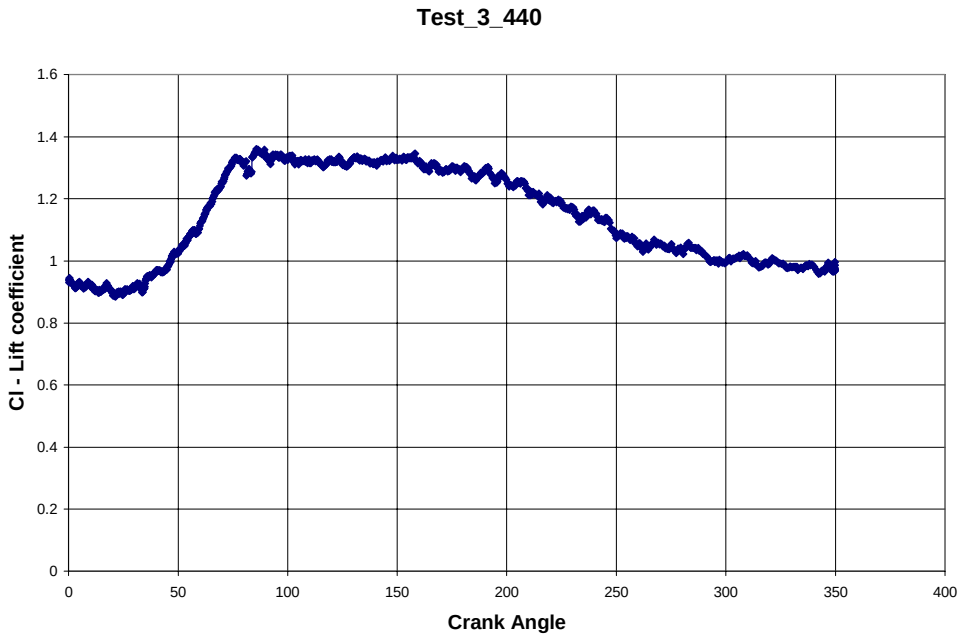

Appendices

Test_3_500: Re=500,000, k=0.05

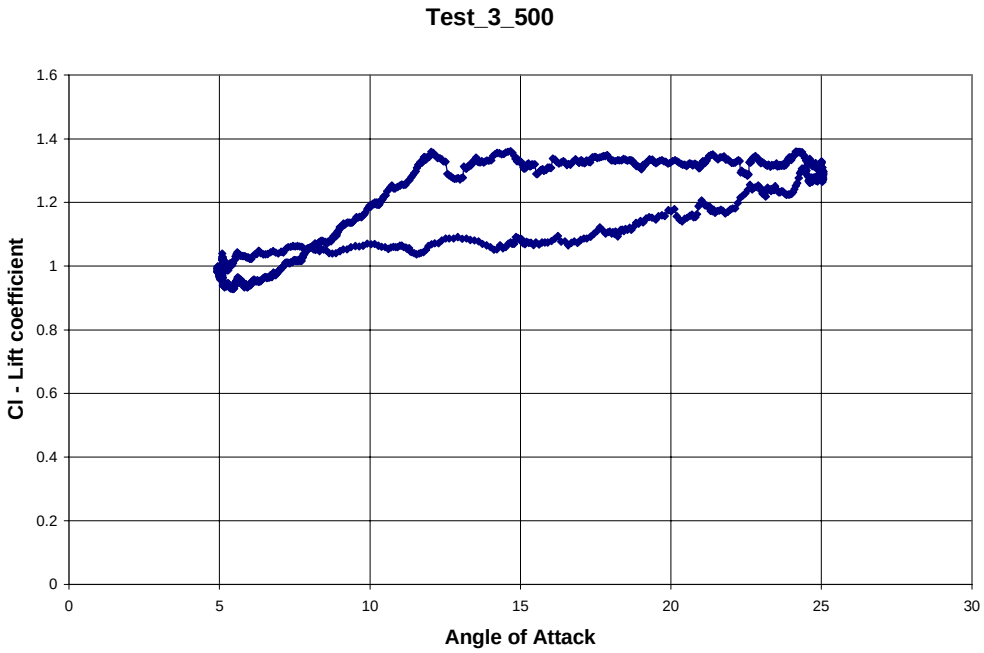

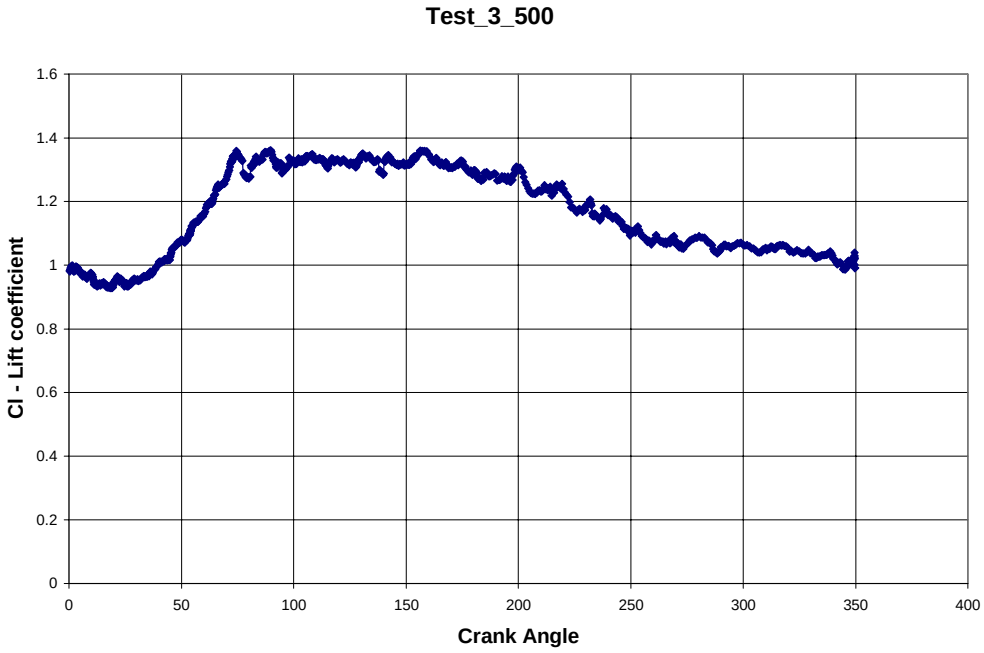

Appendices

Test_4_200: Re=200,000, k=0.1

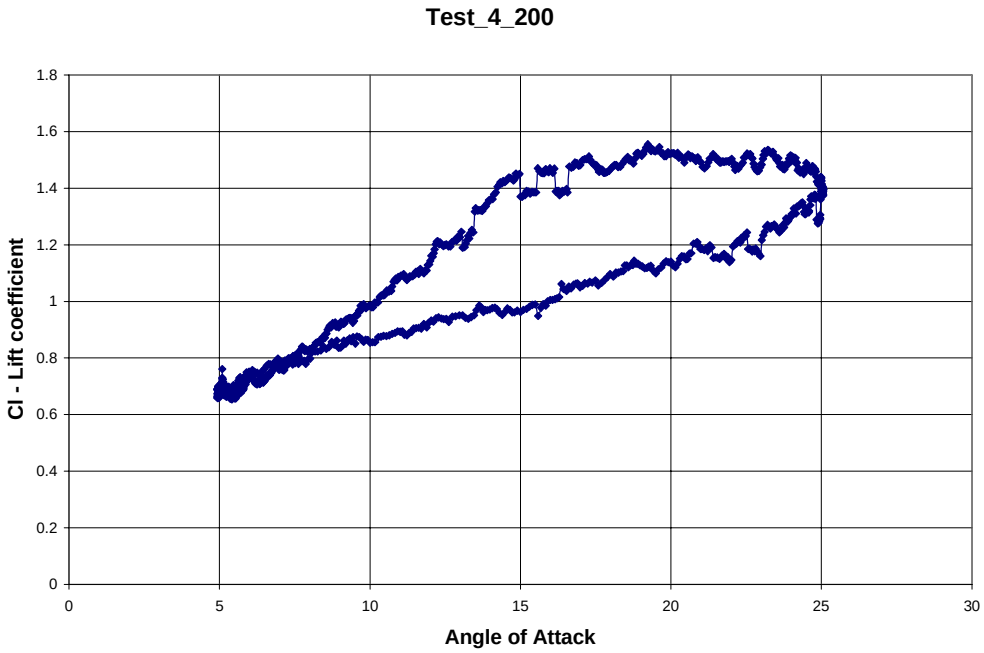

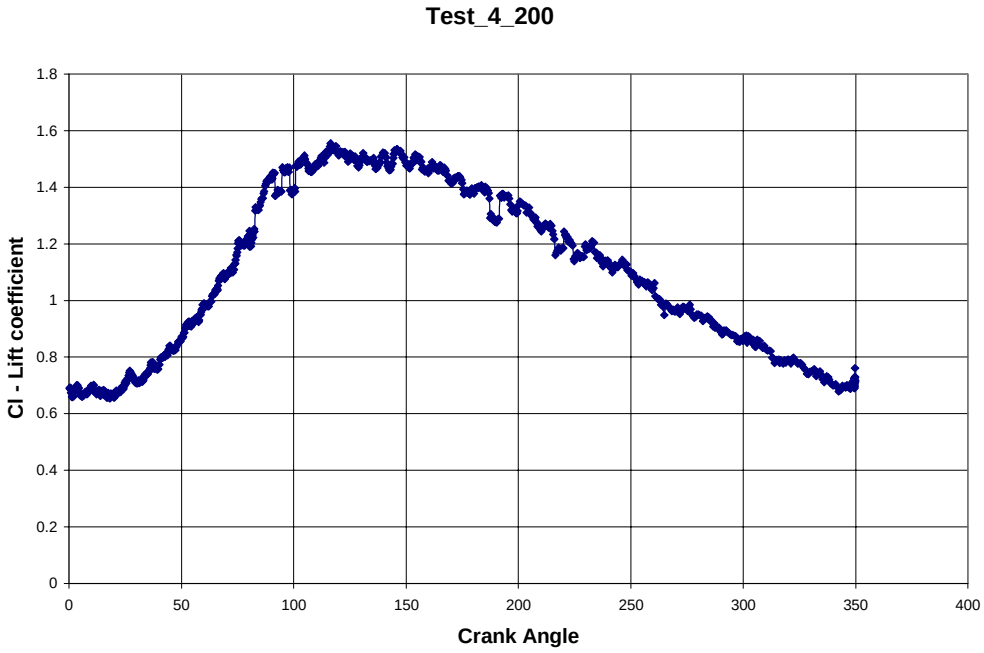

Appendices

Test_4_260: Re=260,000, k=0.1

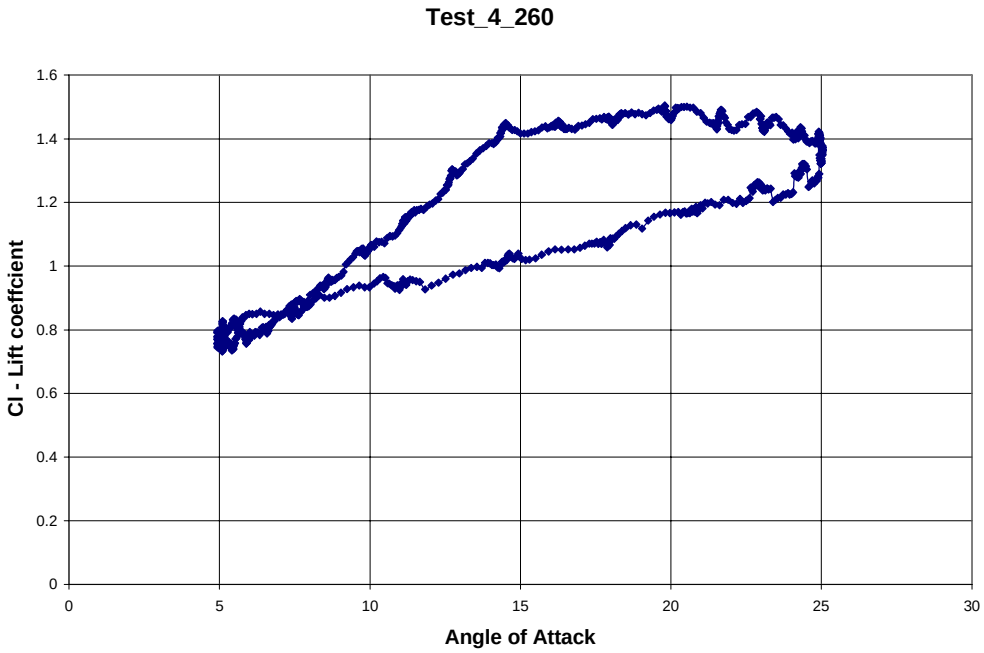

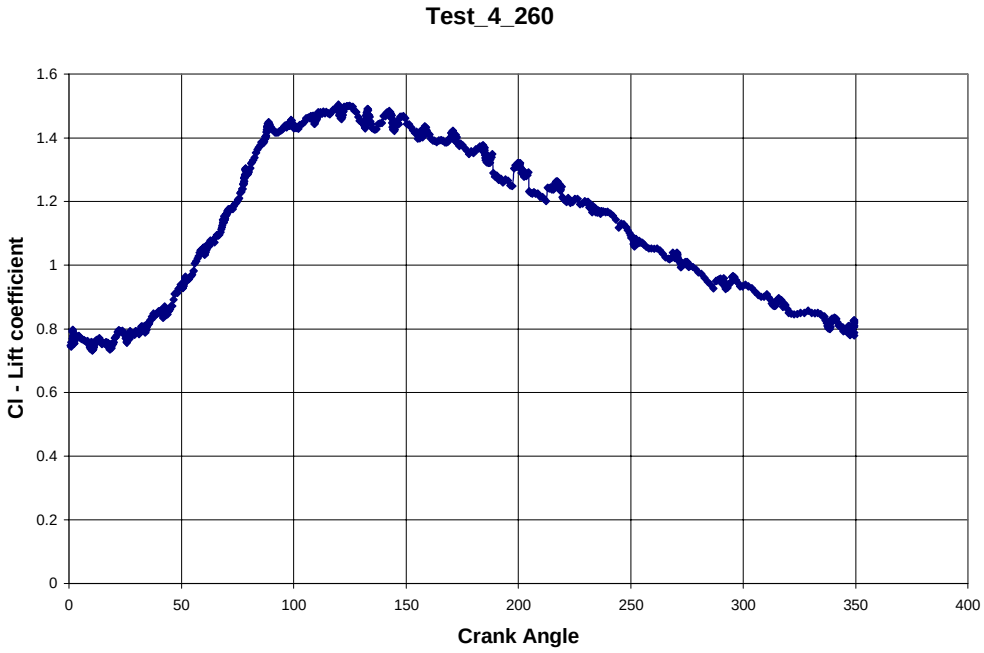

Appendices

Test_4_320: Re=320,000, k=0.1

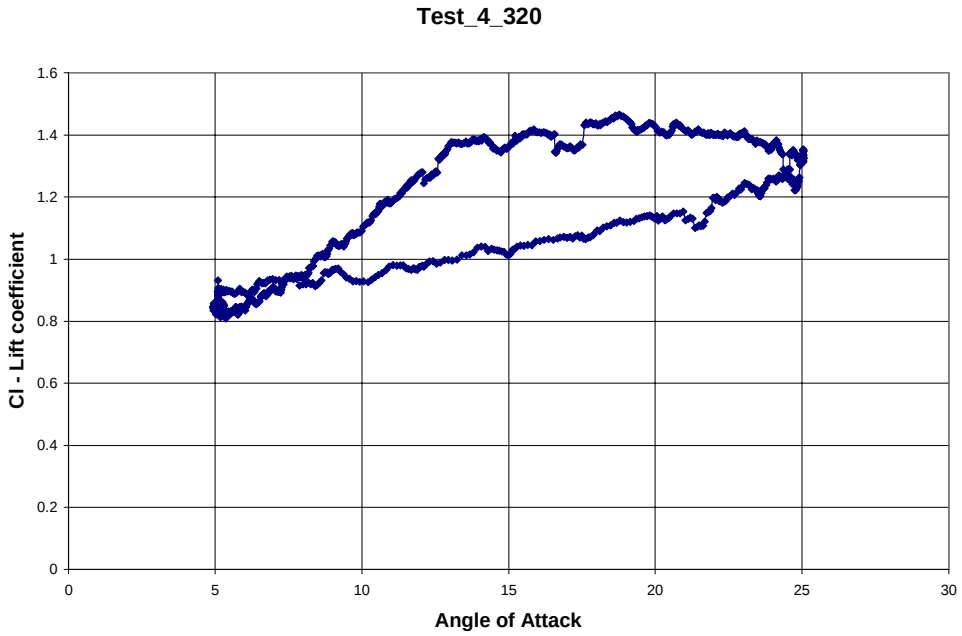

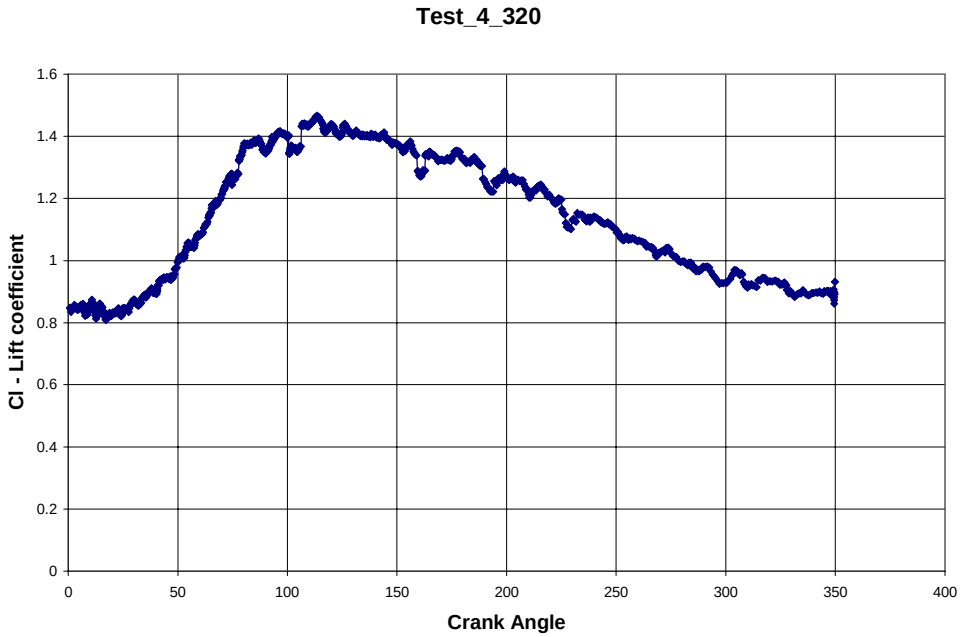

Appendices

Test_4_380: Re=380,000, k=0.1

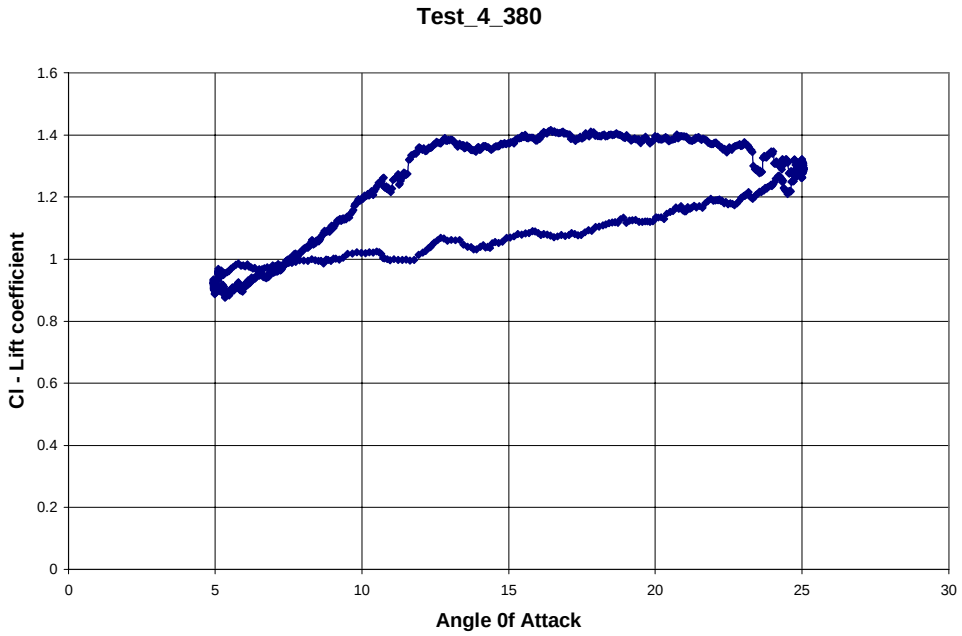

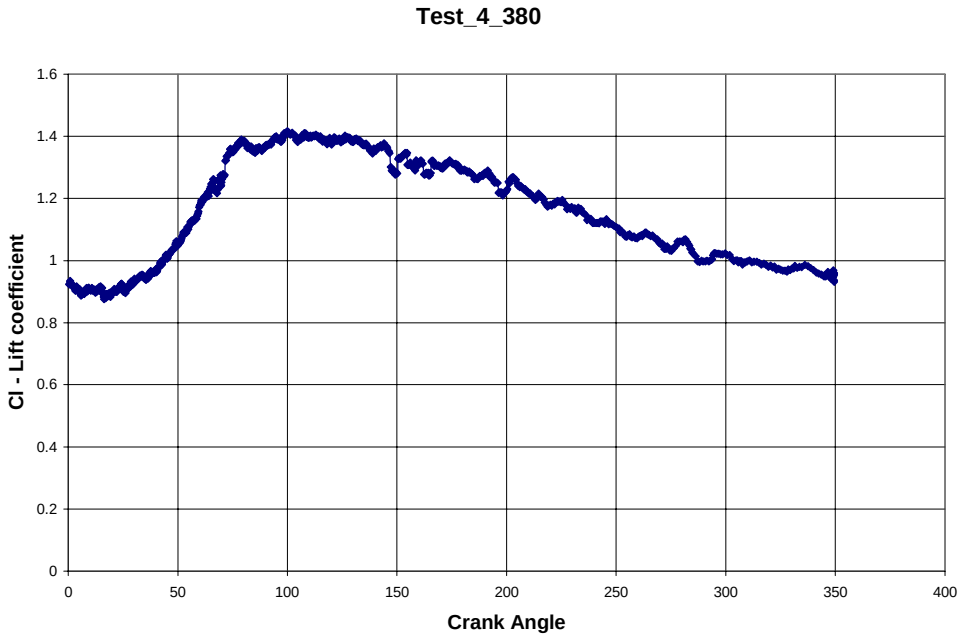

Appendices

Test_4_440: Re=440,000, k=0.1

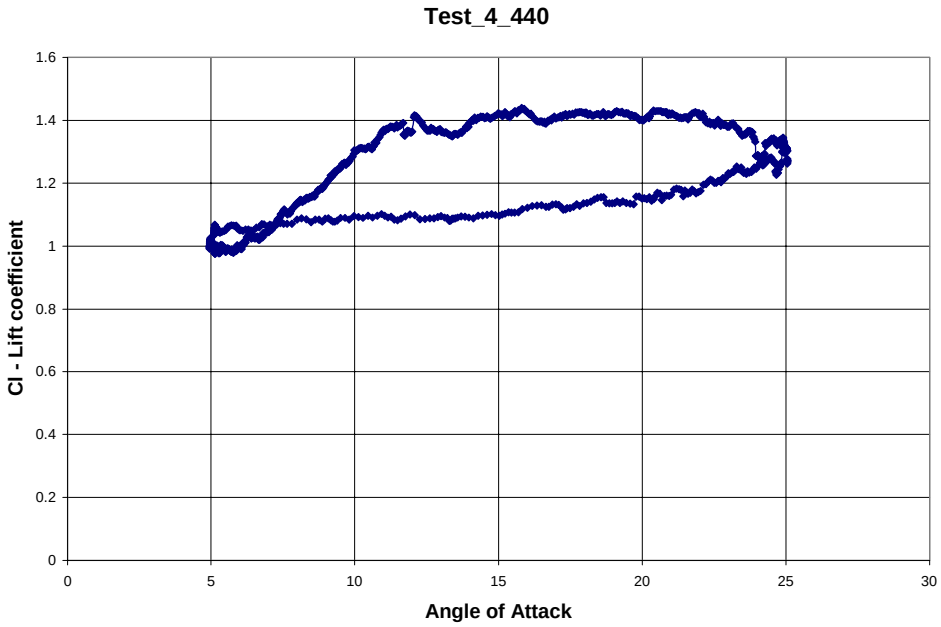

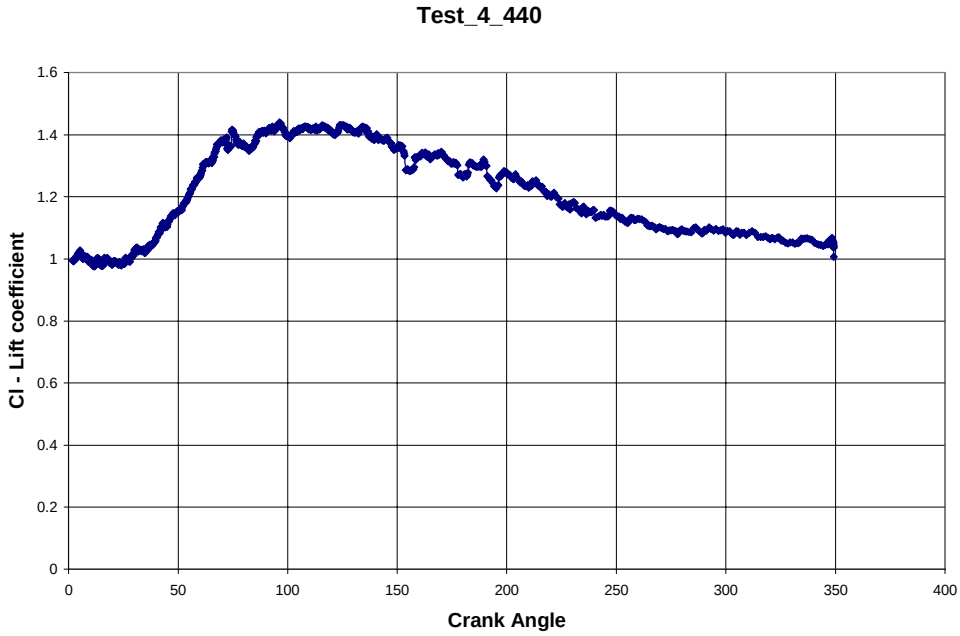

Appendices

Test_4_500: Re=500,000, k=0.1

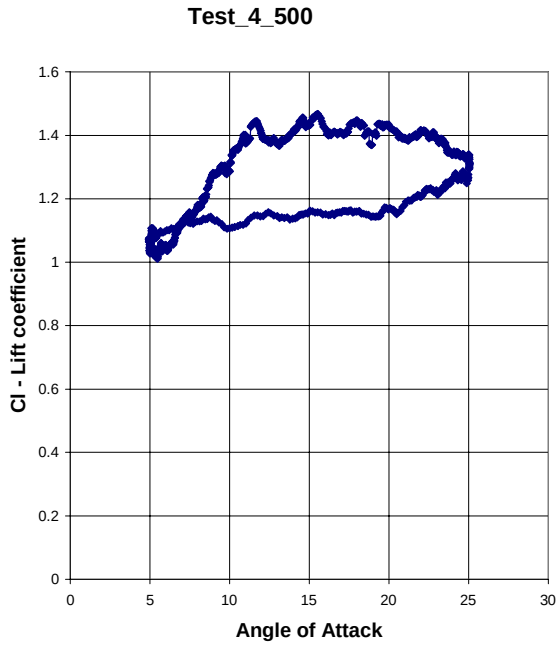

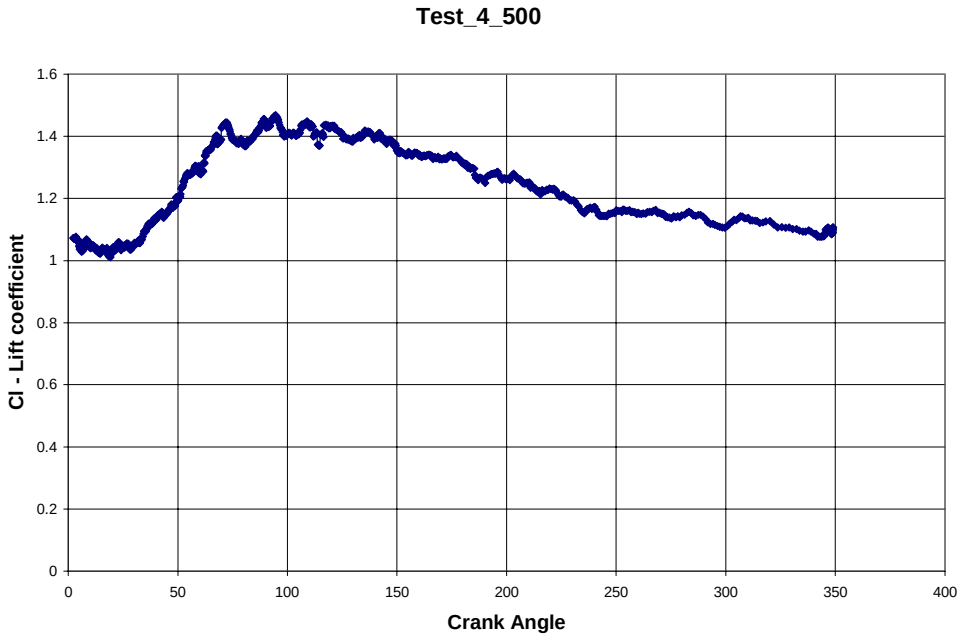

Appendices

Test_5_200: Re=200,000, k=0.15

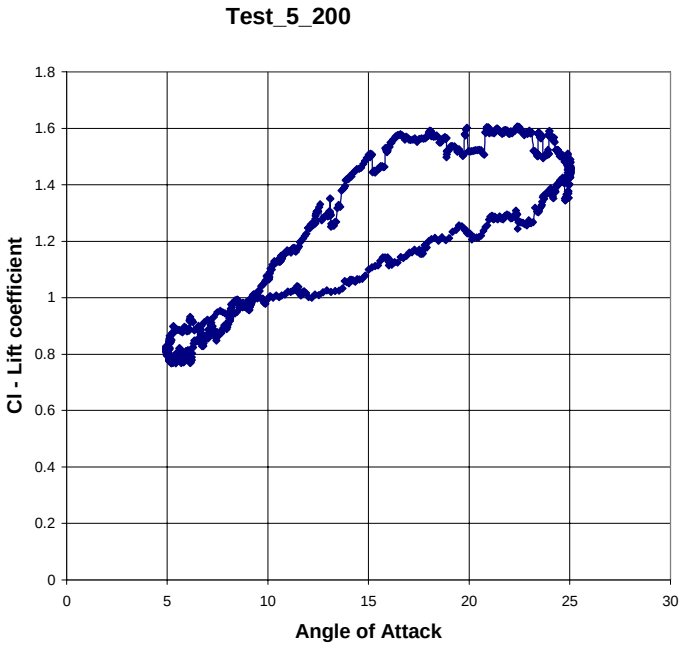

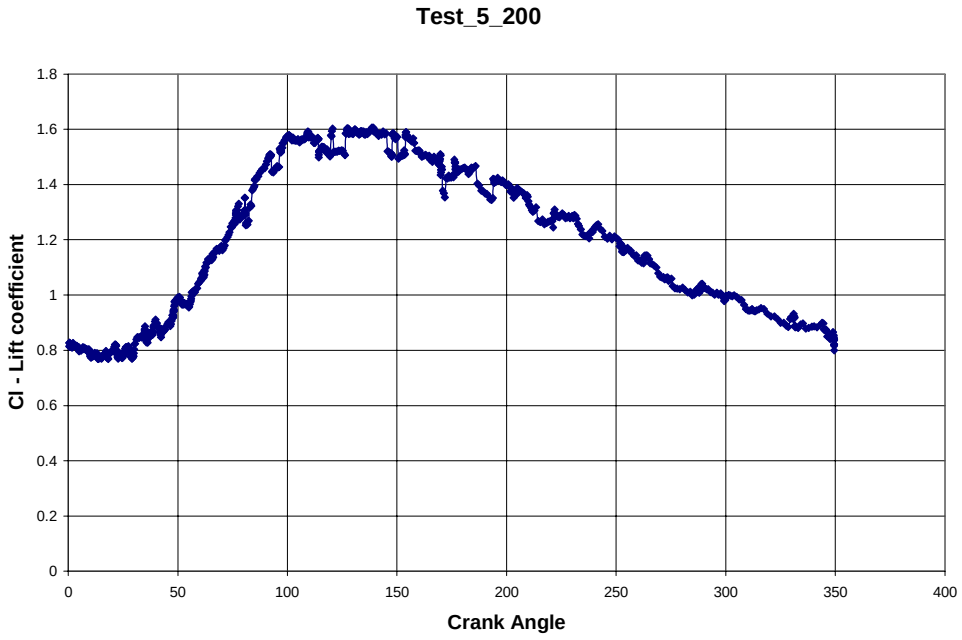

Appendices

Test_5_260: Re=260,000, k=0.15

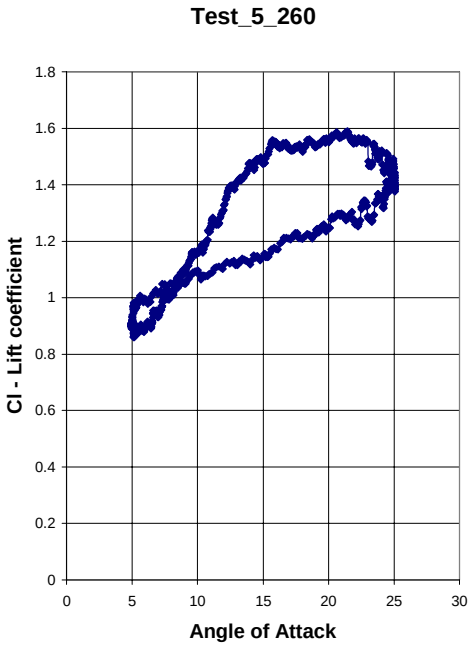

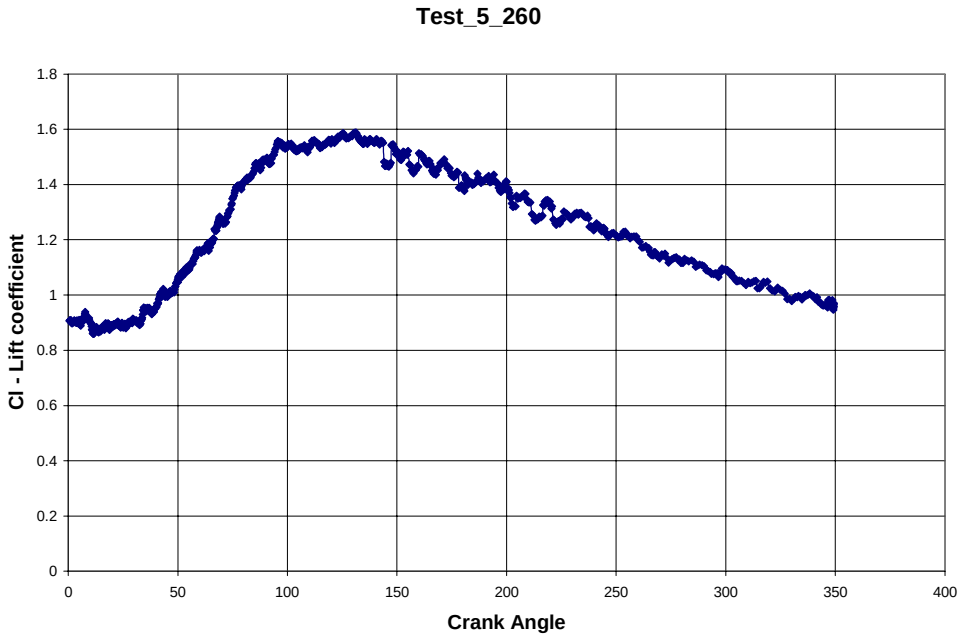

Appendices

Test_5_320: Re=320,000, k=0.15

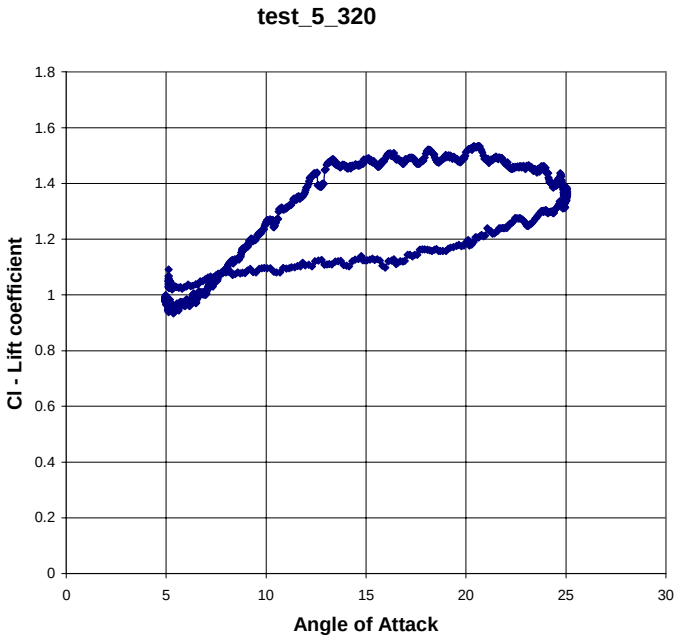

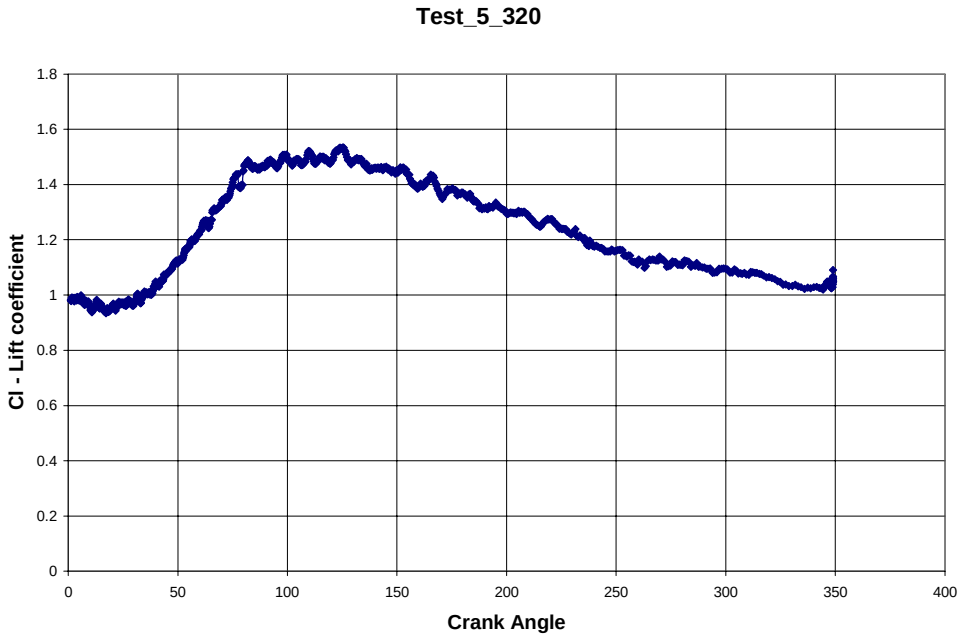

Appendices

Test_5_380: Re=380,000, k=0.15

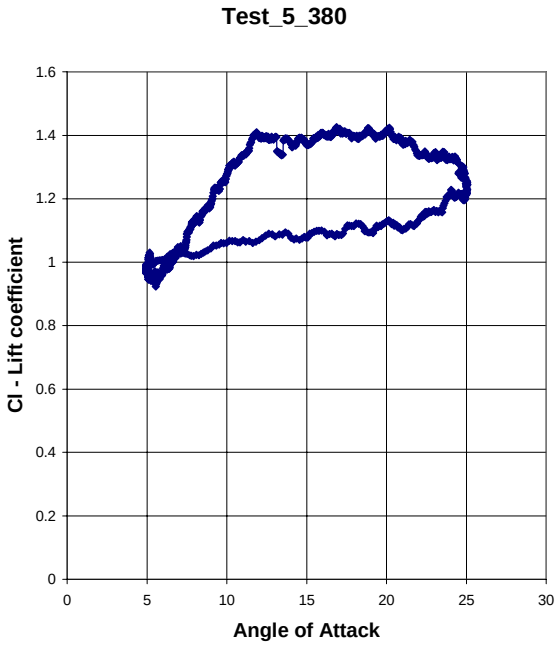

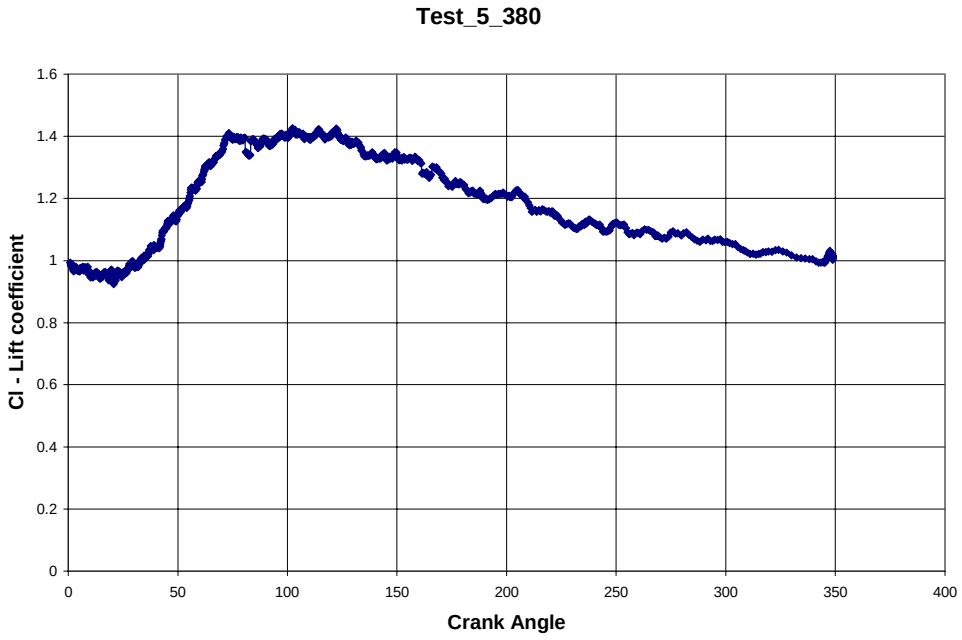

Appendices

Test_6_200: Re=200,000, k=0.2

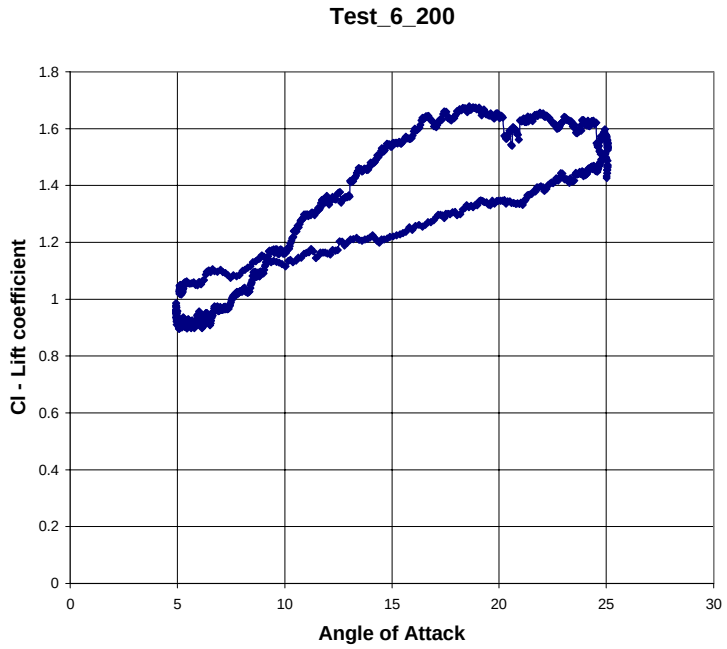

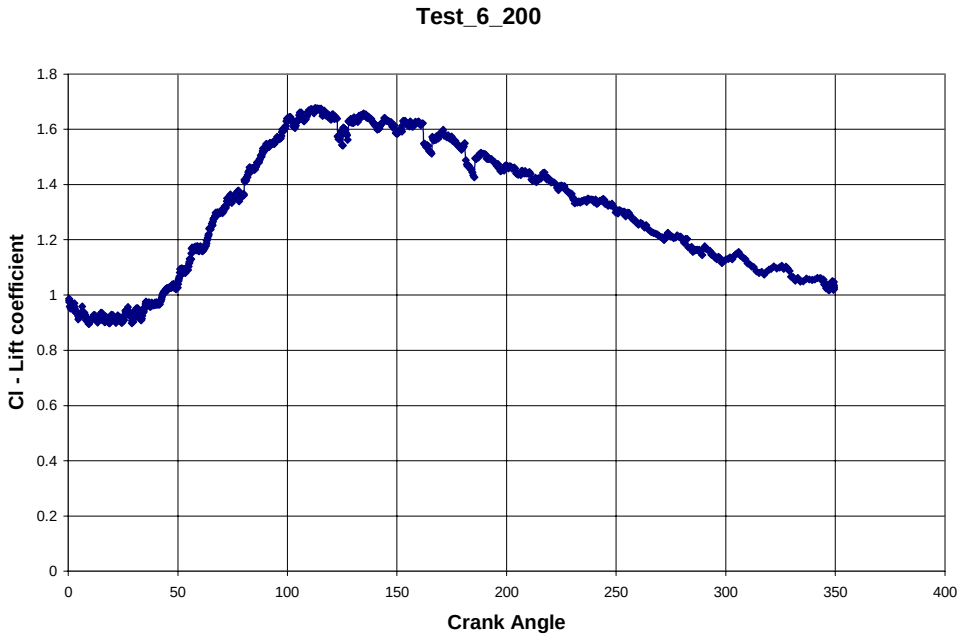

Appendices

Test_6_260: Re=260,000, K=0.2

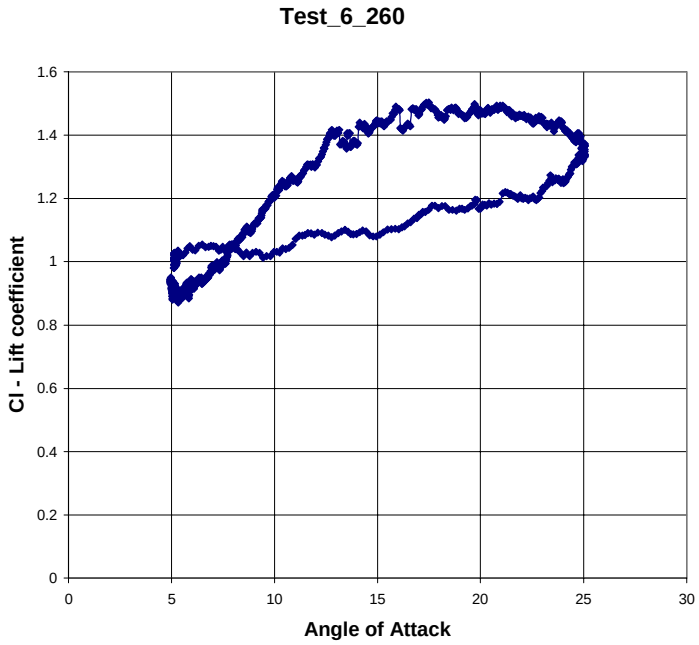

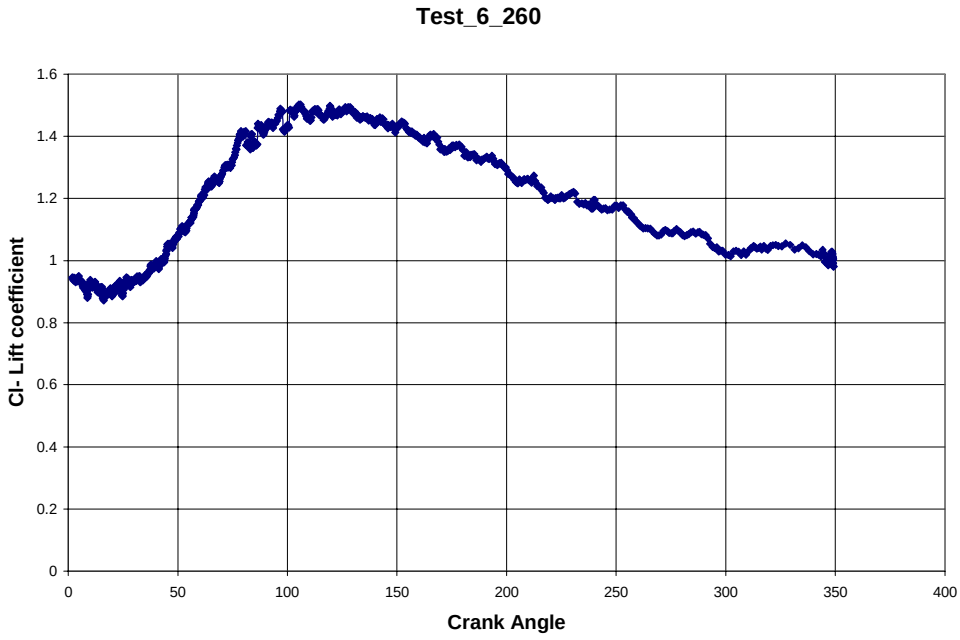

Appendices

Test_7_200: Re=200,000, k=0.25

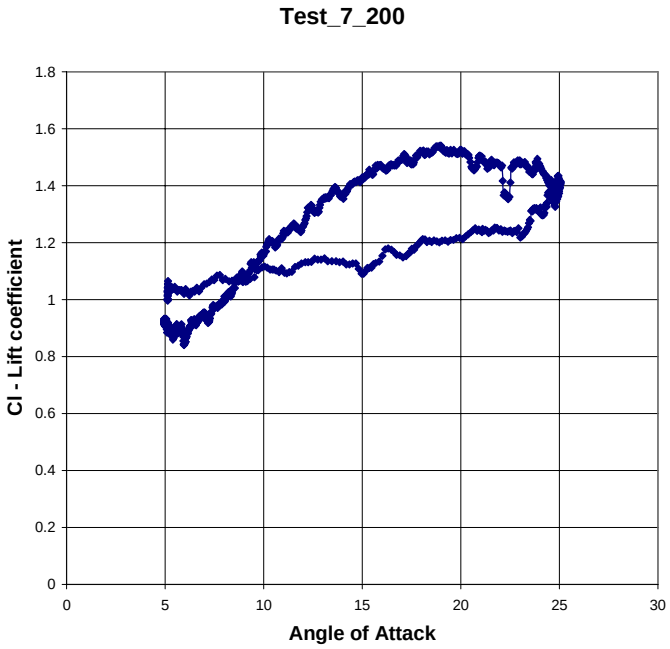

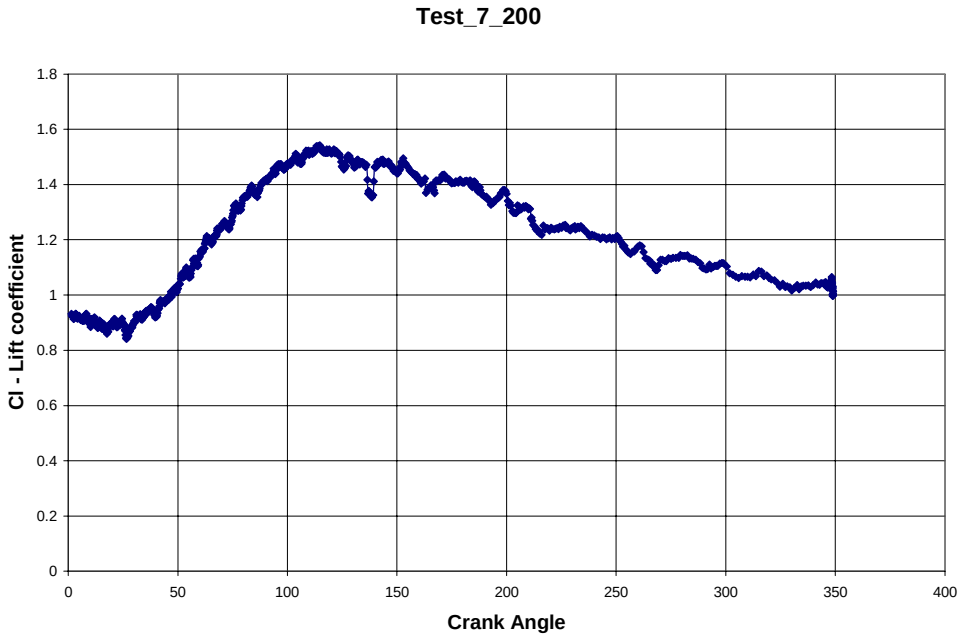

Appendices

Test_8_200: Re=200,000, k=0.3

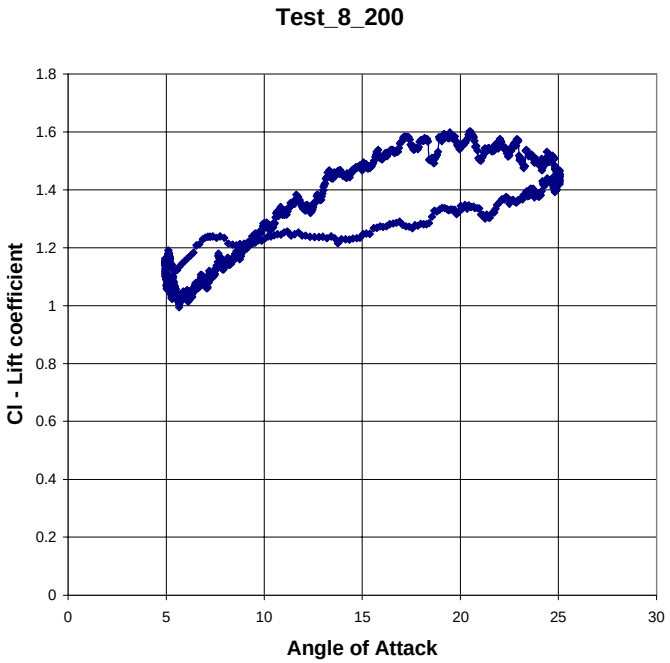

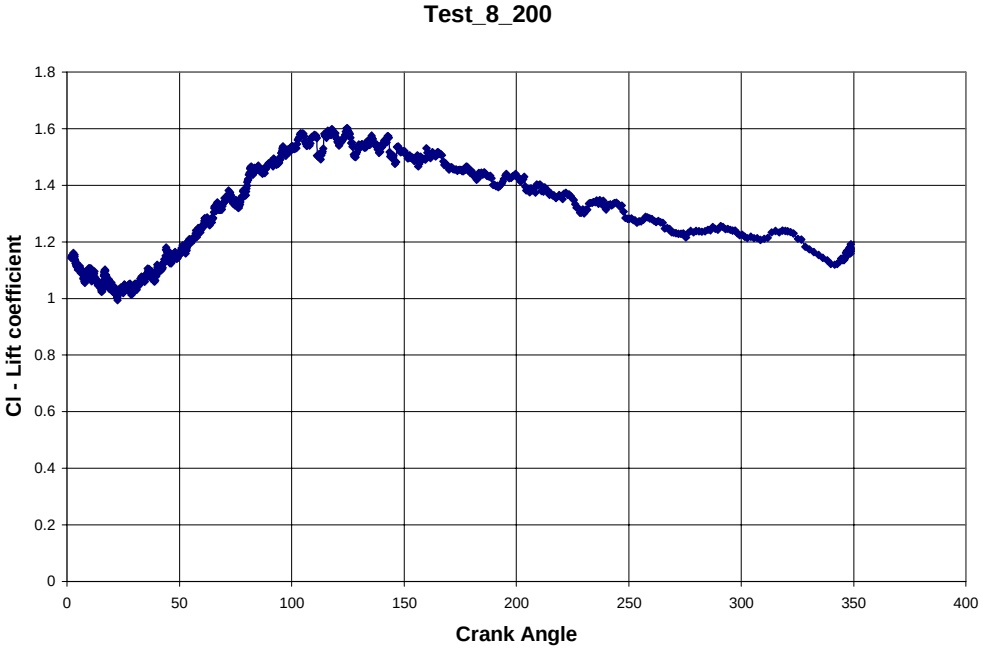

Appendices

Appendix C: Calibration Plot

Calibration Plot: NACA-0012

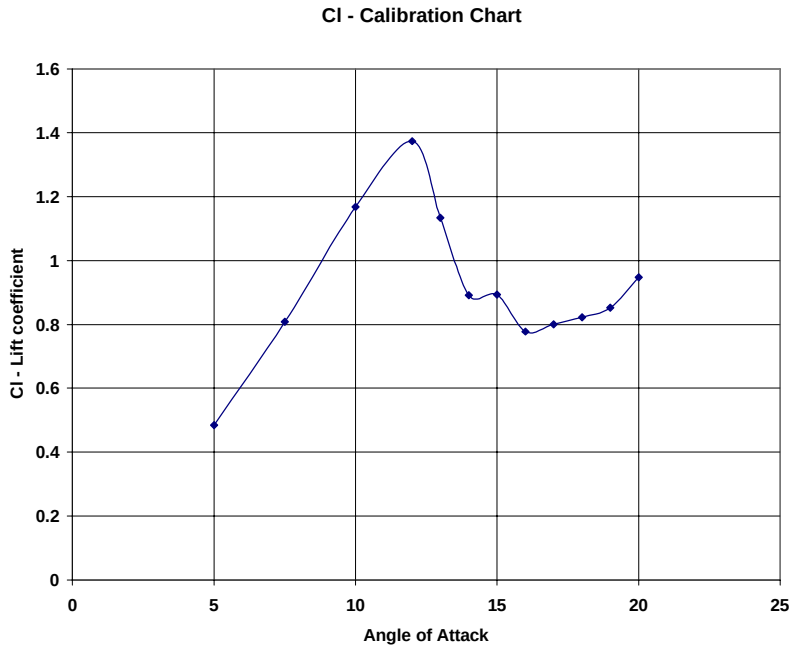

Appendices

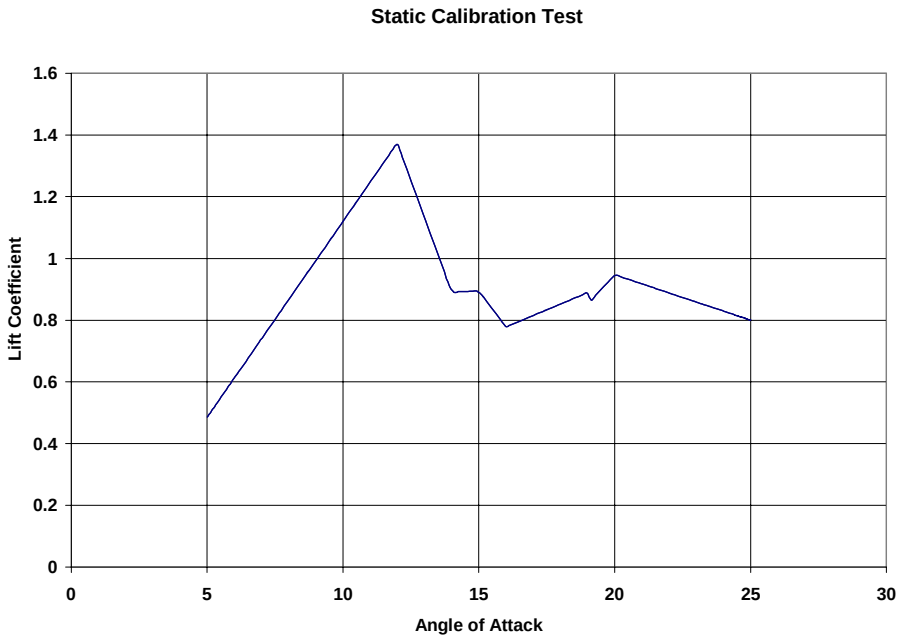

Piecewise Static Calibration Plot

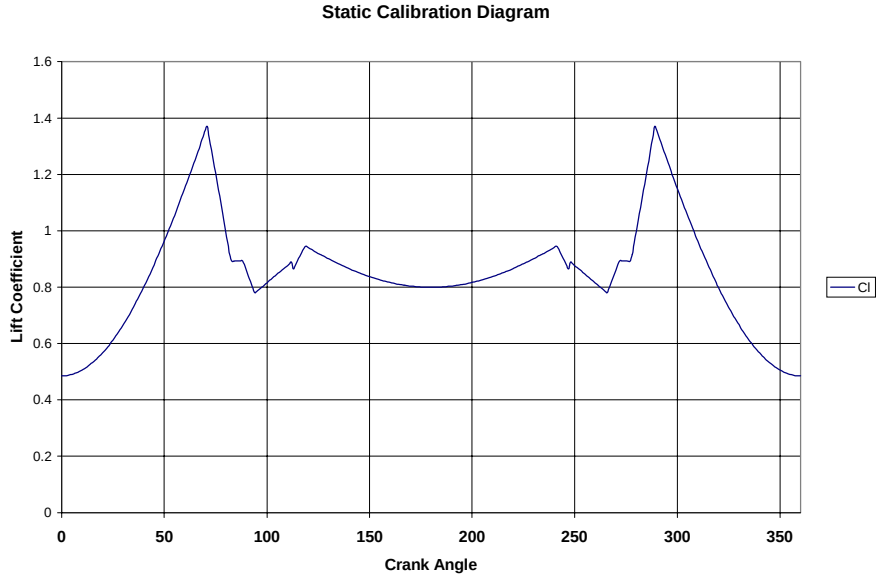

Lift Coefficient vs. Crank Angle generated from Piecewise Static Plot shown above.

Appendices

Appendix D: Table of Test Values

Reduced Frequencies

$$k = \frac{wc}{2V_\infty}$$

chord (ft)	0.333333										
density, rho	0.002242										
viscosity, mu	3.67E-07		1	2	3	4	5	6	7	8	Test #
mph	ft/sec	Re	0.004	0.02	0.05	0.1	0.15	0.2	0.25	0.3	K
67.13027	98.45772	2.00E+06	2.3630	11.8150	29.5376	59.0752	88.6128	118.1504	147.6881	177.2257	
87.28935	127.9525	2.60E+06	3.0719	15.3596	38.3989	76.7978	115.1967	153.5956	191.9945	230.3934	
107.4084	157.5223	3.20E+06	3.7808	18.9041	47.2602	94.5204	141.7805	189.0407	236.3009	283.5611	
127.5475	187.0686	3.80E+06	4.4897	22.4486	56.1215	112.2429	168.3644	224.4858	280.6073	336.7288	
147.6865	216.6083	4.40E+06	5.1986	25.9831	64.9827	129.9655	194.9482	259.9310	324.9137	389.8965	
167.8256	246.1480	5.00E+06	5.9075	29.5376	73.8440	147.6881	221.5321	295.3761	369.2201	443.0642	

Frequency, Rad/sec

	98.45772	2.00E+06	0.3761	1.8804	4.7010	9.4021	14.1031	18.8042	23.5052	28.2063
	127.9525	2.60E+06	0.4889	2.4445	6.1114	12.2227	18.3341	24.4454	30.5568	36.6682
	157.5223	3.20E+06	0.6017	3.0087	7.5217	15.0433	22.5650	30.0867	37.6084	45.1300
	187.0686	3.80E+06	0.7146	3.5728	8.9320	17.8640	26.7960	35.7279	44.6599	53.5919
	216.6083	4.40E+06	0.8274	4.1369	10.3423	20.6846	31.0269	41.3692	51.7115	62.0538
	246.1480	5.00E+06	0.9402	4.7010	11.7526	23.5052	35.2578	47.0105	58.7631	70.5157

Frequency, Rev/sec

Tests conducted at values in shaded cells

Appendices

Appendix E: LabView Program

Labview Program

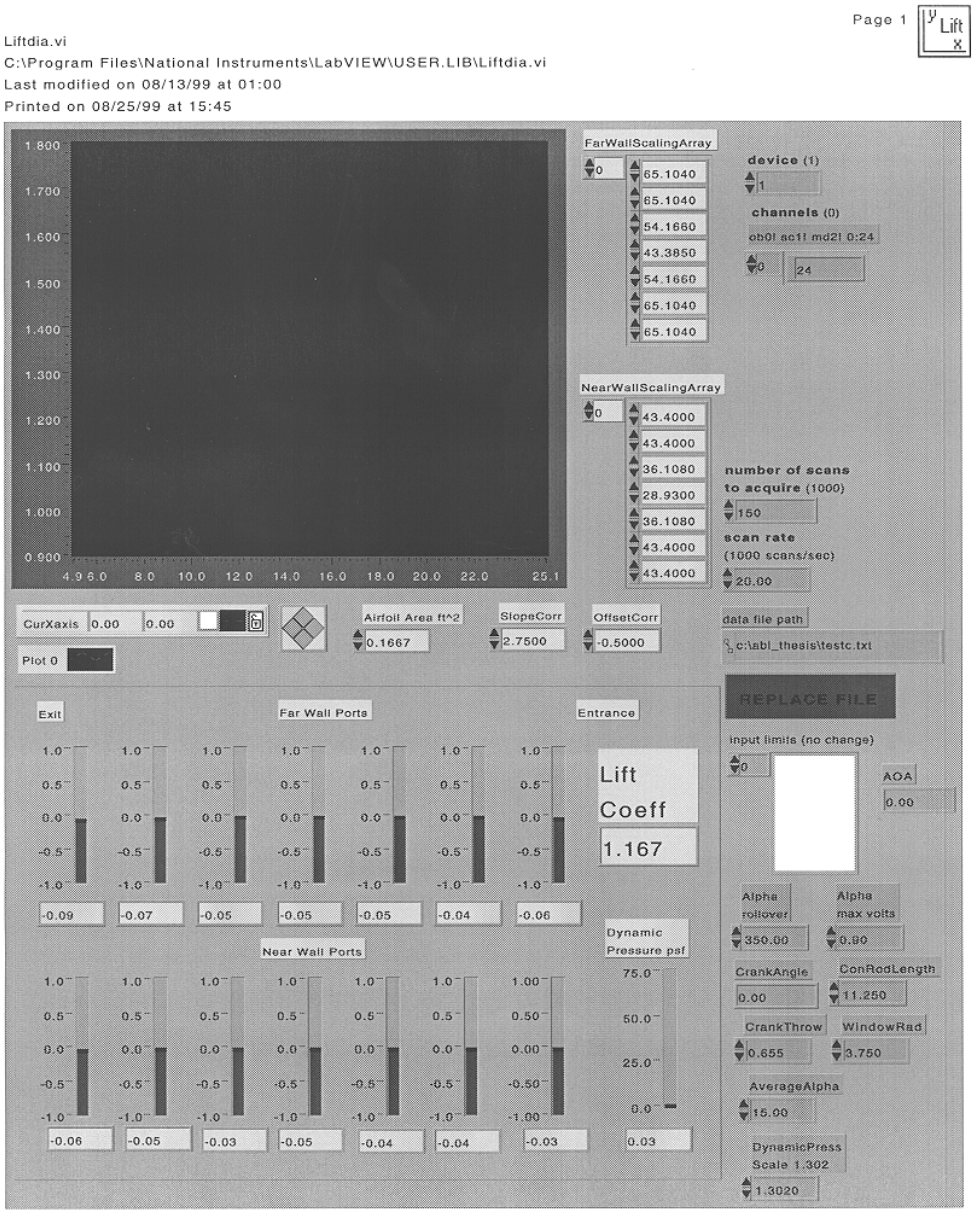

Data acquisition system front panel, Labview virtual instrument.

Appendices

Labview Program

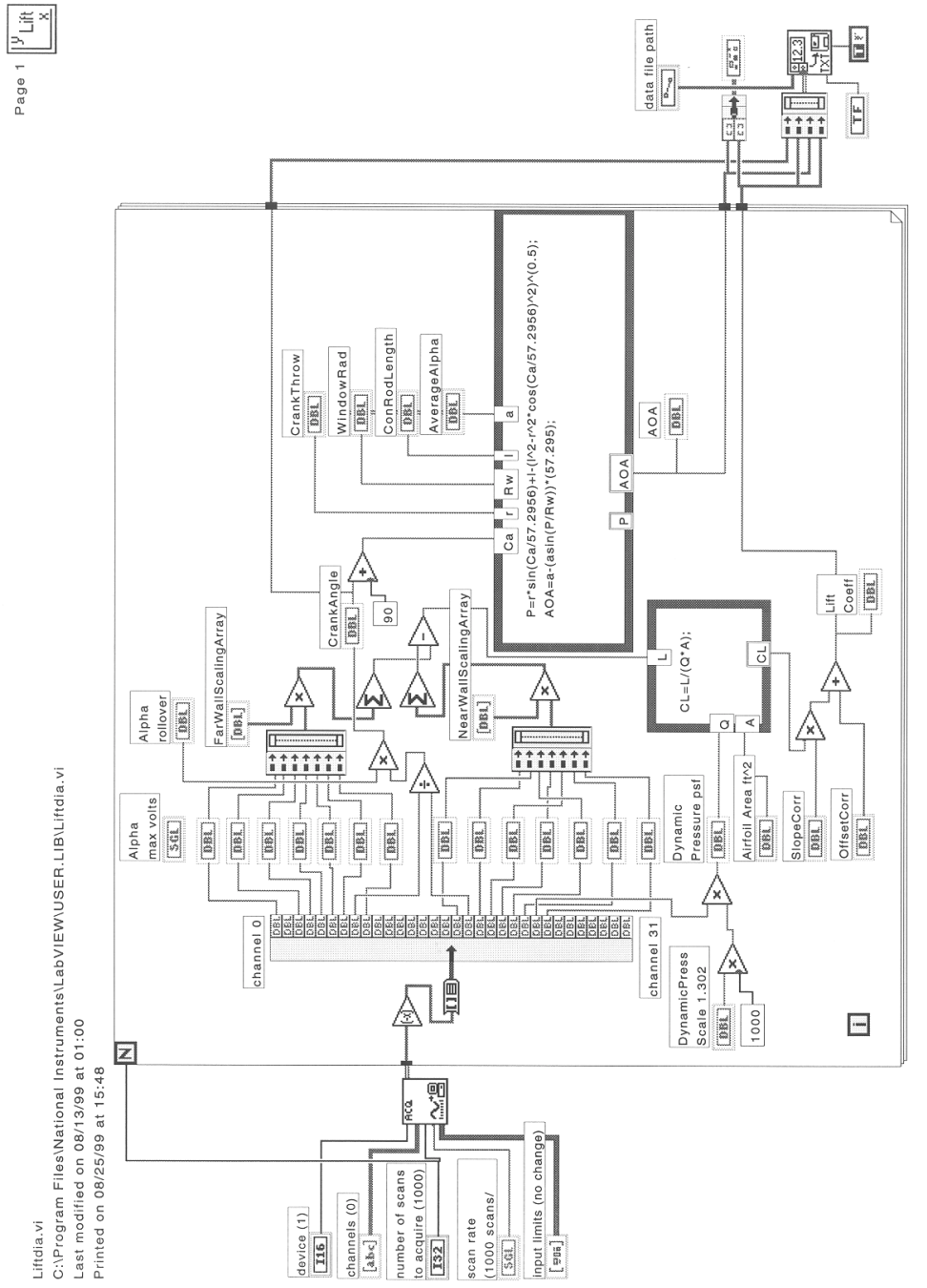

Data acquisition diagram, Labview Virtual Instrument

Appendices

Appendix F: Instrument Interconnect Diagram

Instrument Interconnect Diagram

Electrical Interconnect diagram

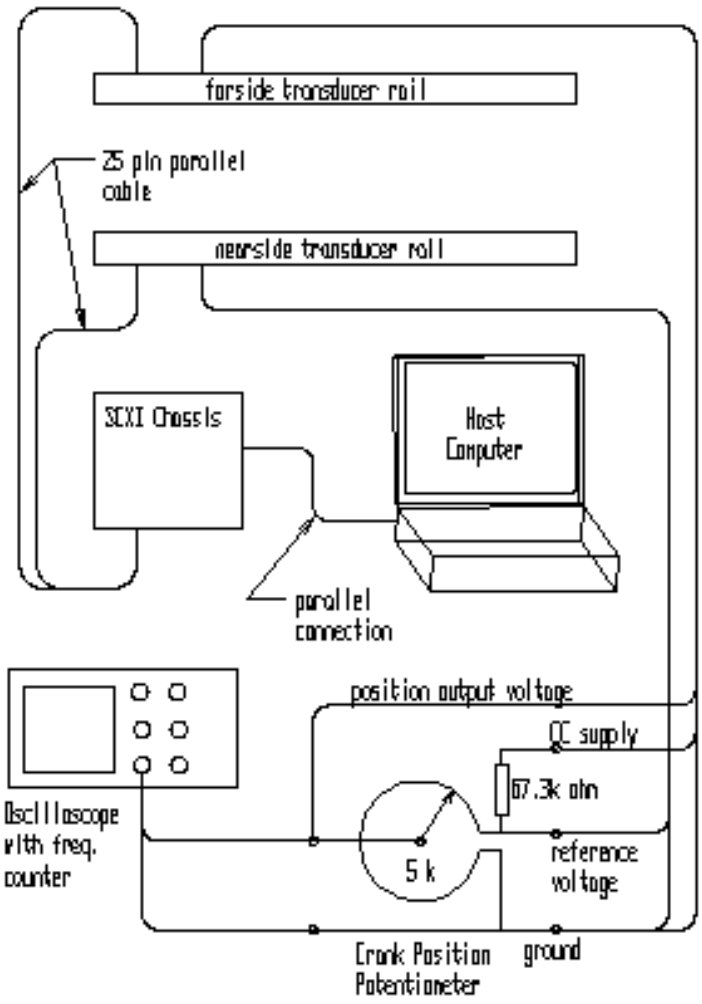

Transducer rails contained the transducers and their power supplies. The SCXI chassis contained the scanner/parallel communication module and the 32 channel instrument amplifier.

Appendices

Instrument Interconnect Diagram continued:

Pneumatic Interconnect Diagram

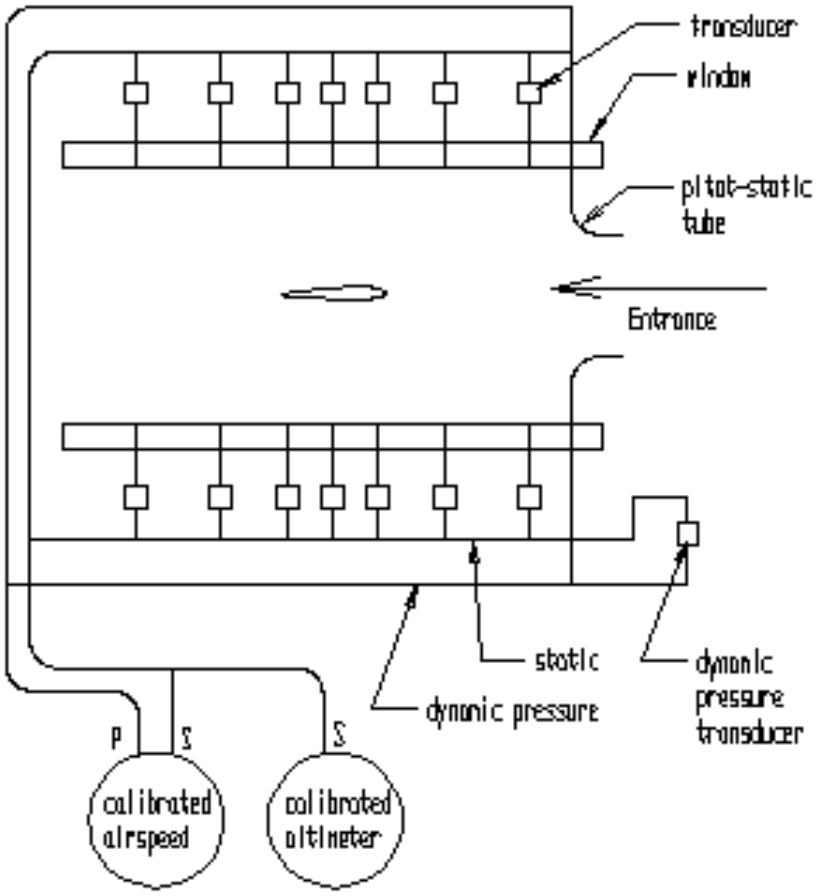

Pressure transducers were mounted in the instrument rail. Calibrated airspeed indictor provided tunnel free stream velocity. Calibrated altimeter provided test section pressure altitude.

Appendices

Appendix G: Constant Current Supply

Constant Current Power Supply

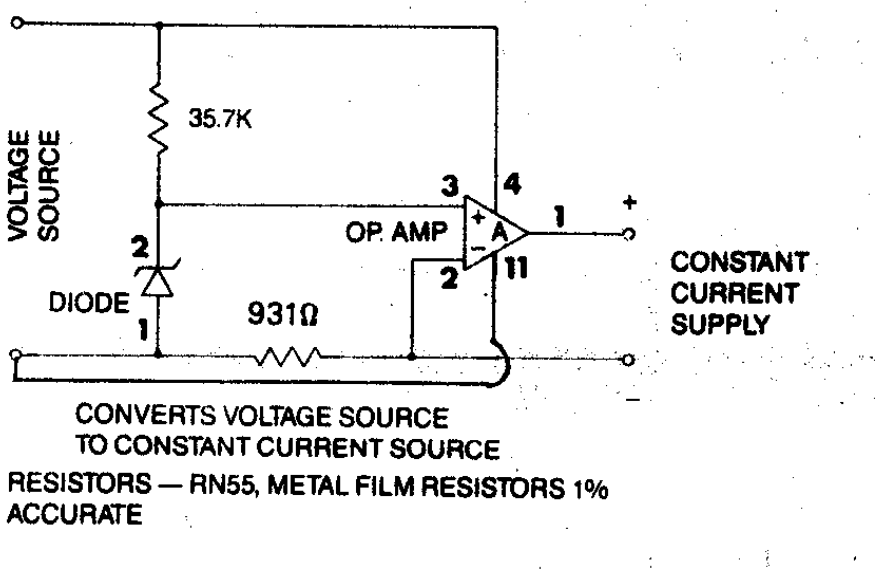

Appendices

Appendix H: Constant Current Supply Circuit Board

Constant Current Power Supply Circuit Board

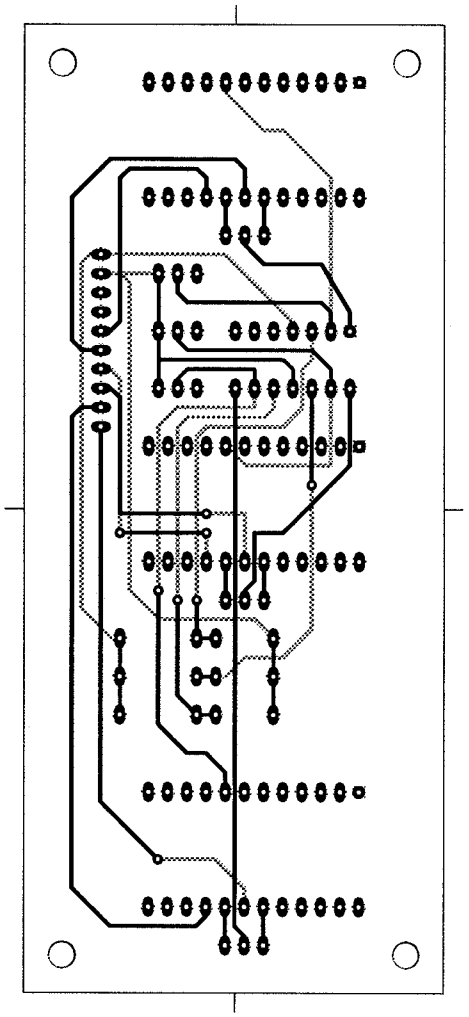

Appendices

Appendix I: Transducer Specification Sheet

Transducer Specification Sheet

Dimensions

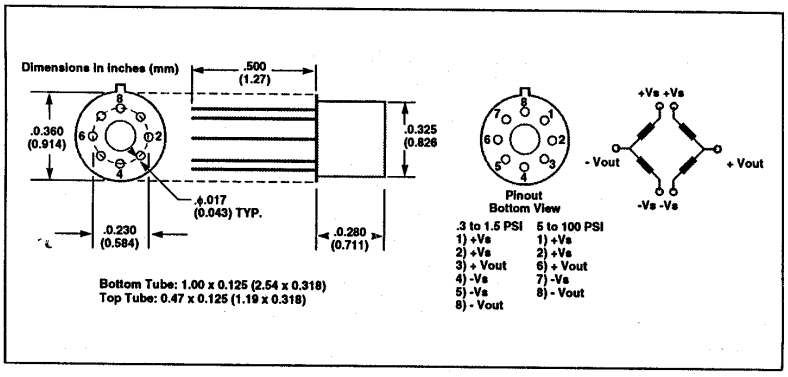

Specifications

Linearity:	±0.5% FS
Excitation Current:	1.5 mA
Storage Temp. Range:	-40 to 125°C
Compensated Temp. Range:	-15 to 85°C
Zero Temp. Coefficient:	0.07% FS/C
Span Temp. Coefficient:	0.05% FS/C
Bridge Impedance:	3300 ±500 ohms
Proof Pressure:	>3X Full scale
Burst Pressure:	>5X Full scale
Sensitivity (@ 1.5 mA excitation):	
0.0 to 0.3 PSI:	165 mV/PSI
0.0 to 0.8 PSI:	65 mV/PSI
0.0 to 1.5 PSI:	35 mV/PSI
0.0 to 5.0 PSI:	20 mV/PSI
0 to 15 PSI:	9.5 mV/PSI
0 to 30 PSI:	5.5 mV/PSI
0 to 60 PSI:	3.0 mV/PSI
0 to 100 PSI:	2.0 mV/PSI

Appendices

Appendix J: Integrating Manometer

Integrating Manometer

NACA TN No. 1283 Fig. 24

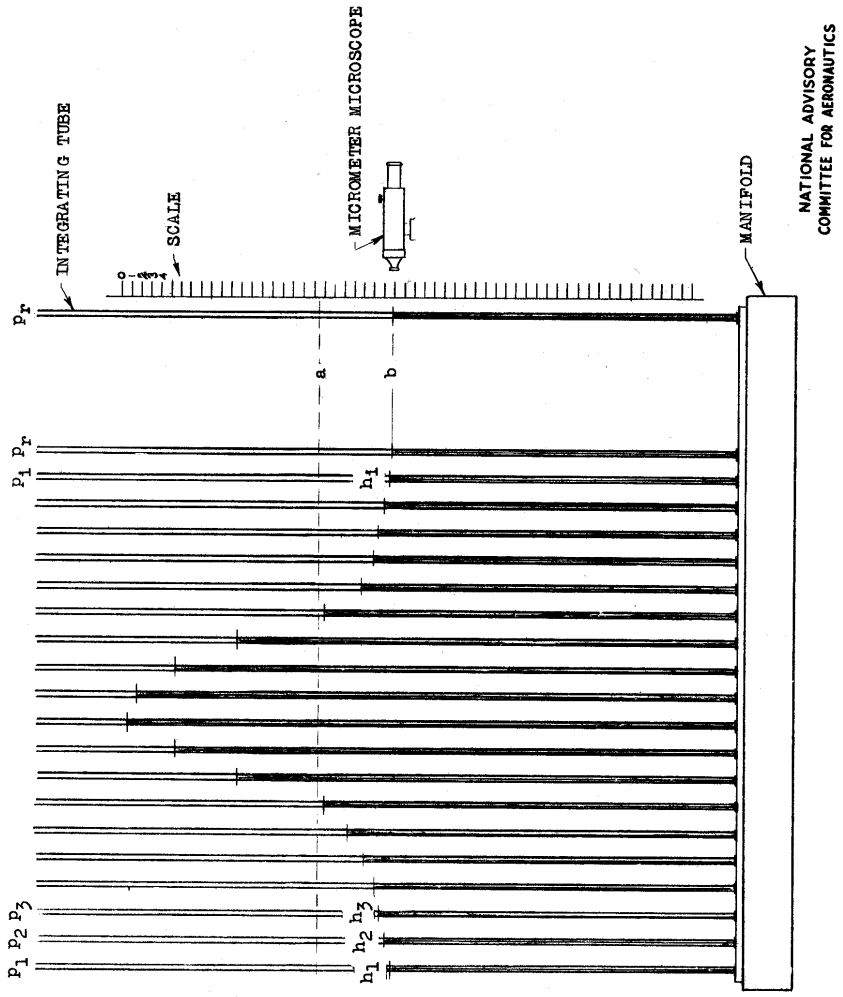

Figure 24.- Schematic drawing of an integrating manometer.

Operating description is on next page.

Appendices

The integrating manometer was used to make rapid lift measurements from tunnel floor and ceiling pressure measurements. The principle of operation is very simple. The internal area of the cross section of the individual tubes numbered p1 through pr was constant and a known value. The integrating tube also had a known internal area. The manifold was kept full and free of voids or bubbles. The integrating tube was pressurized with a convenient reference pressure and the p tubes were connected to floor and ceiling ports within the tunnel test section. The total volume of fluid displaced by the p tubes was measured by observing the change in level of the integrating tube. A measuring microscope was included in the apparatus to enable very accurate measurements.

This device was originally incorporated into the test section of the NACA Two Dimensional Low-Turbulence Pressure Tunnel[12] at Langley, Va. This device permitted extremely accurate measurements of airfoil section lift without introducing mechanical devices into the tunnel such as model supports. This technique also allowed the models to be supported by their ends with moment balances within the tunnel walls .

Appendices

Appendix K: NACA-0012 Airfoil, Static Test Data

NACA-0012 Airfoil, Static Test Data[11]

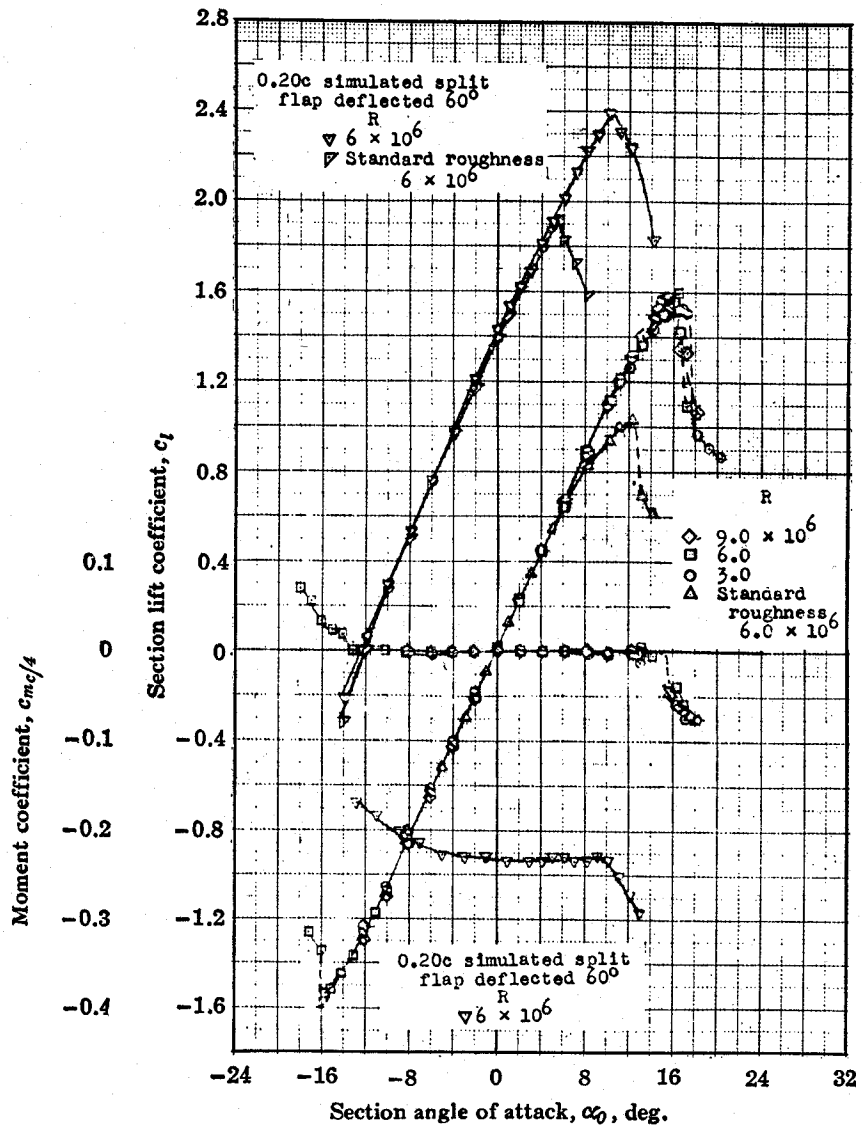

NACA 0012 Wing Section

Appendices

NACA-0012 Airfoil, Static Test Data

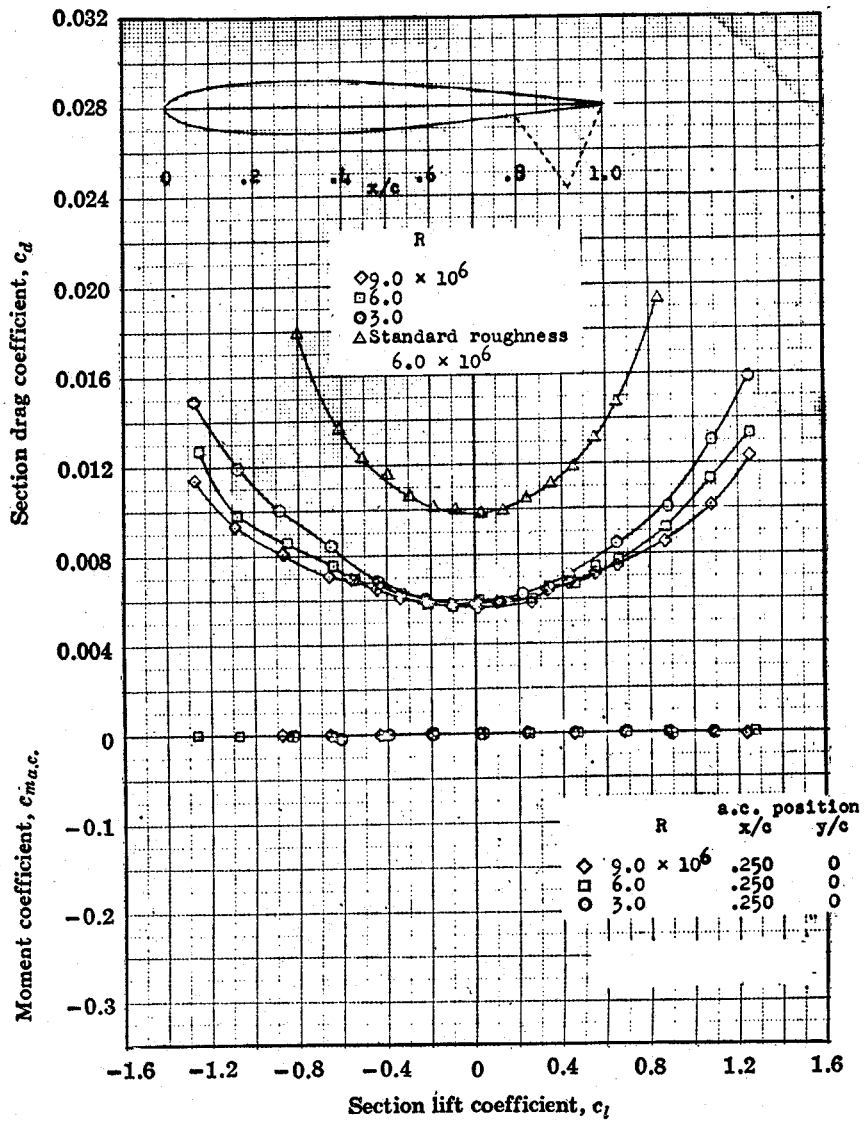

NACA 0012 Wing Section (*Continued*)

Appendices

Appendix L: Derivation of Crank Angle Algorithm

Derivation of Crank Angle Algorithm

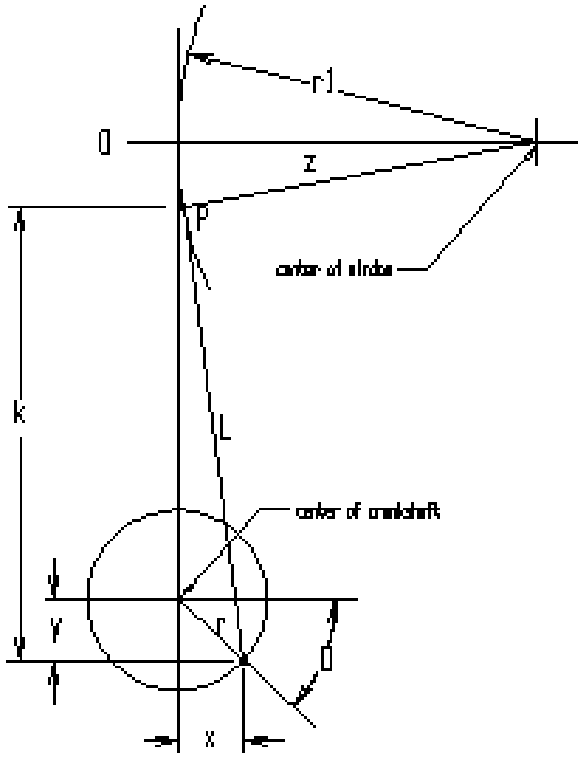

The window position and AOA of the airfoil were determined from the position of the crankshaft.

$$z = \sin^{-1}\frac{P}{r1}$$
$$y = r\sin O$$
$$x = r\cos O$$
$$L = \sqrt{x^2 + k^2}$$
$$k = \sqrt{L^2 + x^2}$$
$$P = y + k$$
$$P = r\sin O + L - \sqrt{L^2 - (r\cos O)^2}$$

Appendices

The crank position was determined from the potentiometer used as a position transducer.

$$O = a\frac{V_I}{V_R}$$

$$AOA = \alpha + \sin^{-1}\frac{P}{r1}$$

Where:

V_I = input voltage
V_R = reference voltage
$R_W = r1$ = window radius
L = connecting rod length
r = crank throw
α = average angle of attack

Appendices

Appendix M: Photo Images

Photo Images:

Image 3; WPI wind tunnel, contraction entrance

Shown is honeycomb, turbulence screens, contraction and test section.

Appendices

Photo Images:

Image 4; tunnel contraction, test section and instrumented window

Appendices

Photo Images:

Image 5; tunnel diffuser

Appendices

Photo Images:

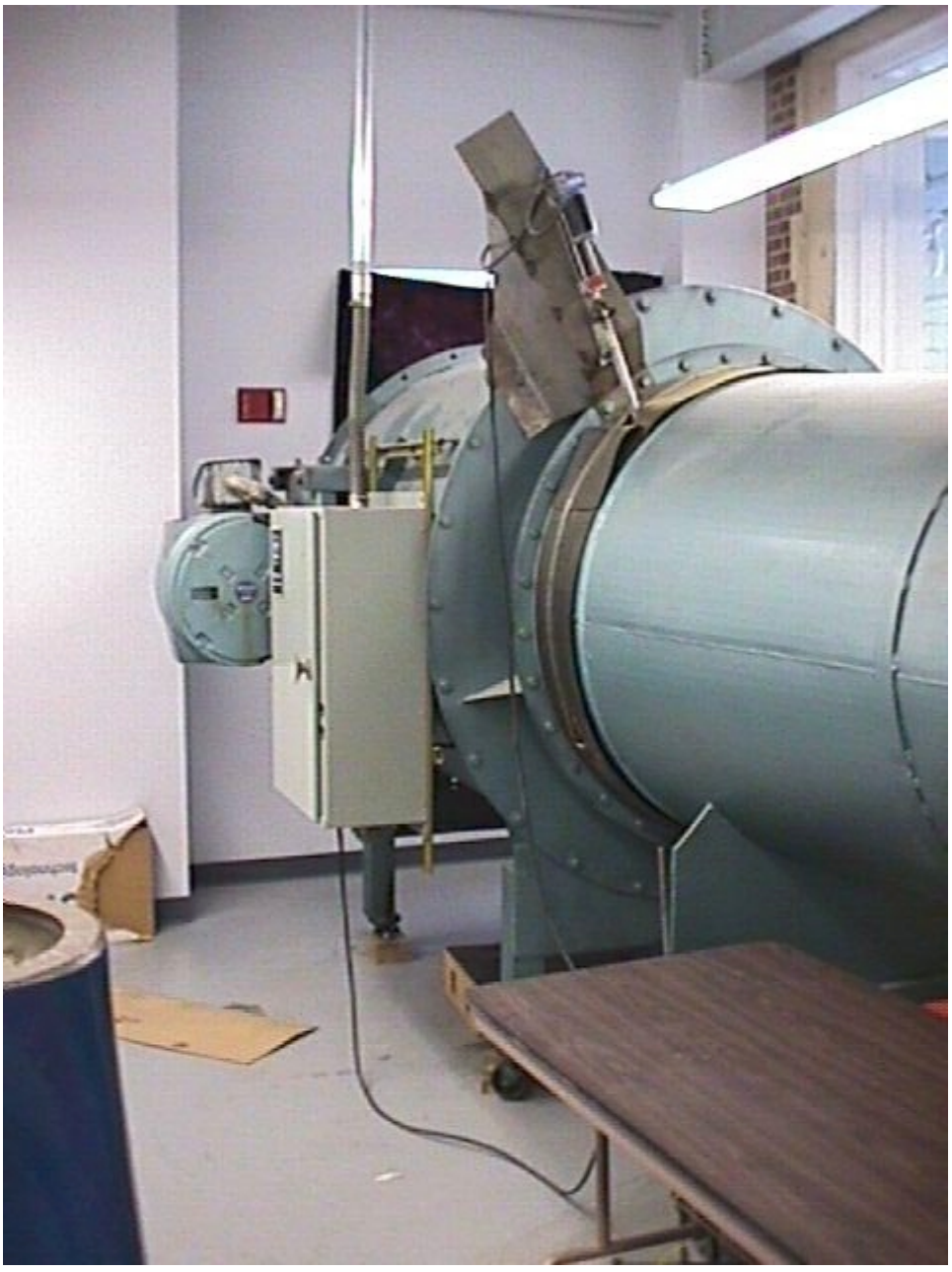

Image 6; tunnel drive section

Tunnel drive with 75hp motor, airfoil fan, and damper speed controls.

Appendices

Photo Images:

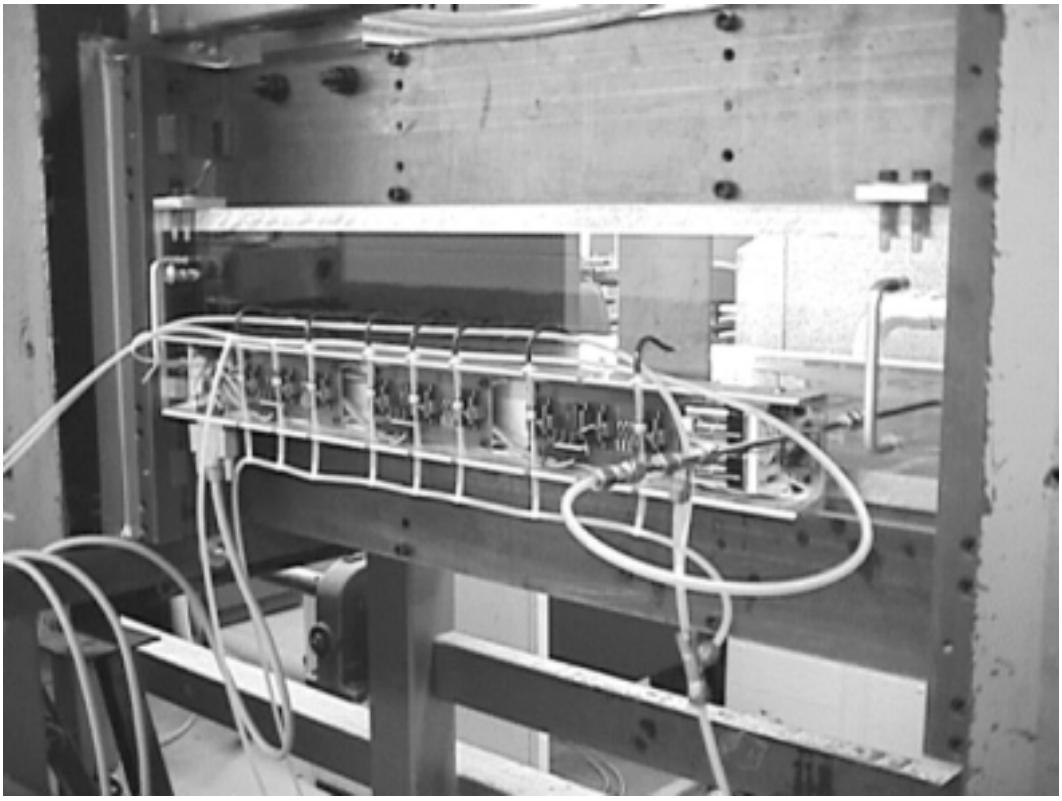

Image 7; instrumented window

Instrumented window with transducer rail, circuit boards and transducers.

Appendices

Photo Images:

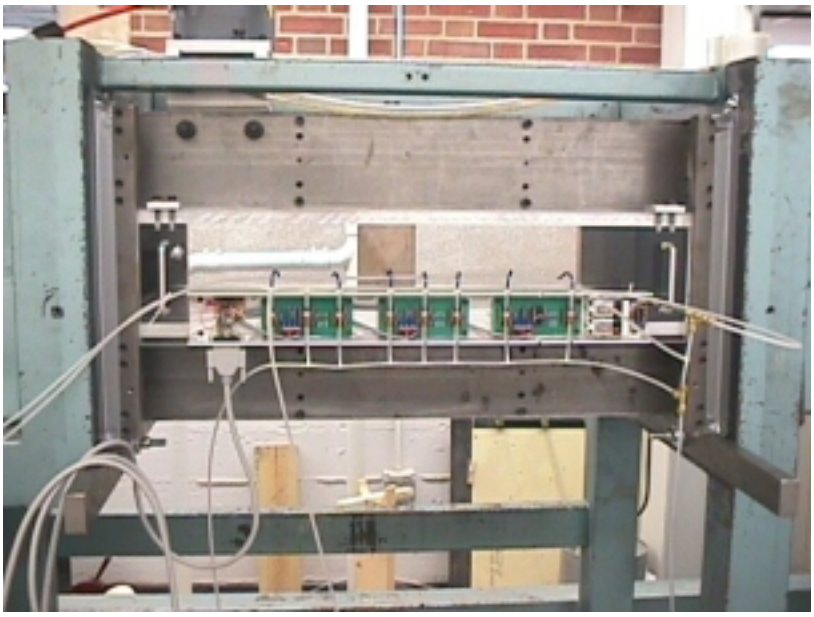

Image 8; instrumented window

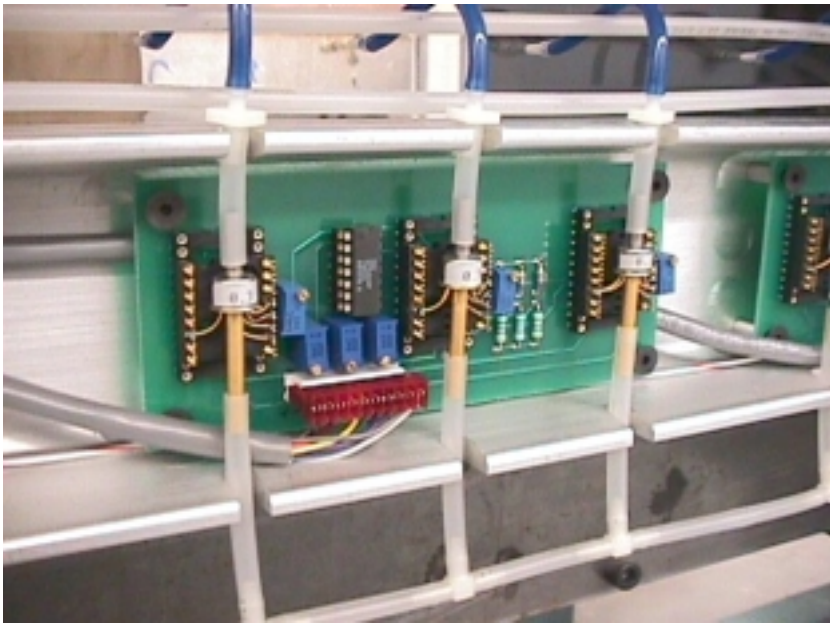

Image 9; transducer circuit board

Appendices

Photo Image:

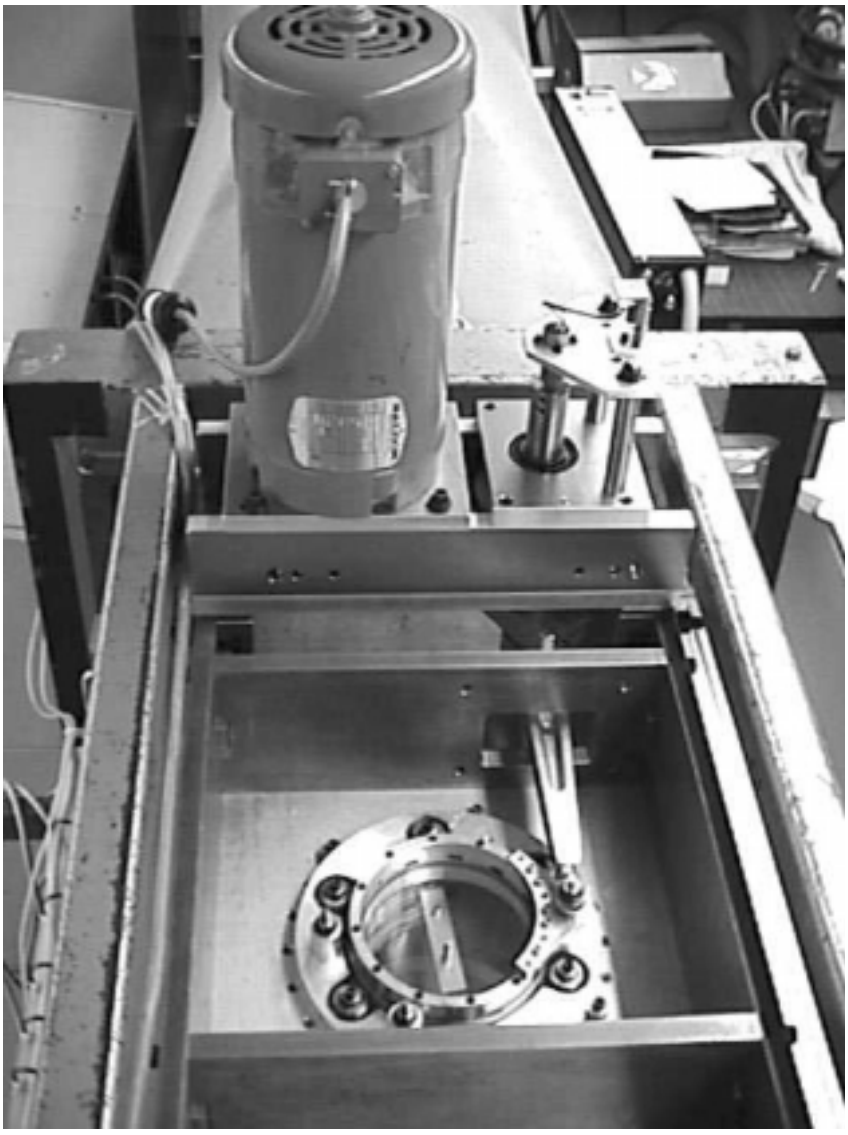

Image 10; top view of test section

Shown is drive motor, crankshaft, crank position transducer, connecting rod, crank block and rotating window.

Appendices

Photo Image:

Image 11; crank position transducer

Crank position transducer, crankshaft, crank block shown at bottom.

Appendices

Appendices

Photo Image:

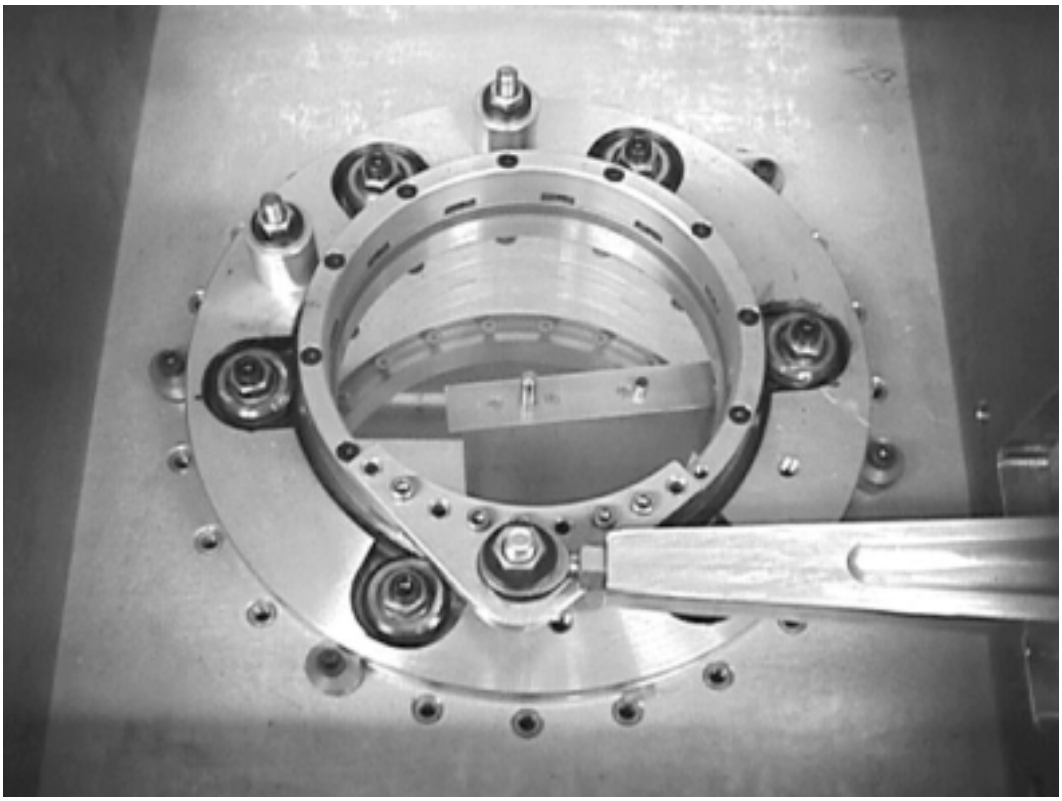

Image 12; rotating window

Rotating window shown with support bearings, connecting rod, rod end, and airfoil shown through glass.

Appendices

Photo Image:

Image 13; airfoil in tunnel

Airfoil shown supported by tunnel bottom fixed window and upper rotating window.

Appendices

Appendix N: Test section CAD drawings

Test section CAD drawings

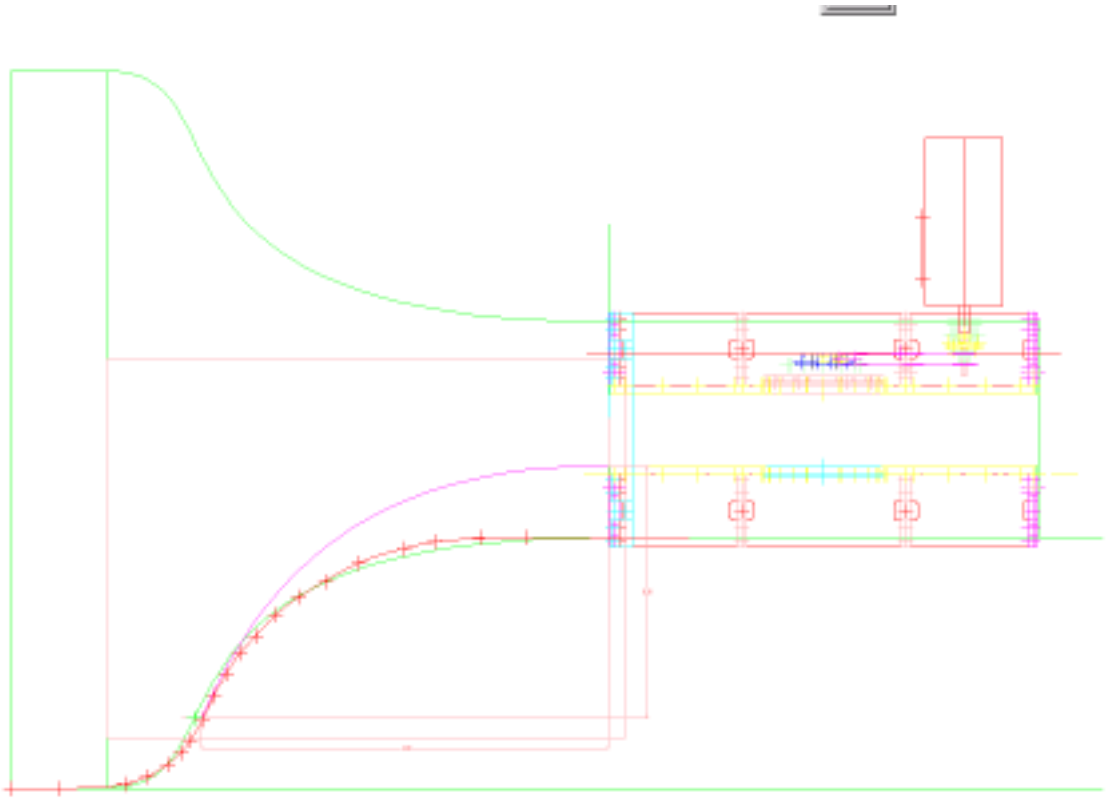

Side view of tunnel contraction and test section, note spline curve blending contraction bottom surface up to bottom of test section insert.

Appendices

Test Section CAD Drawings:

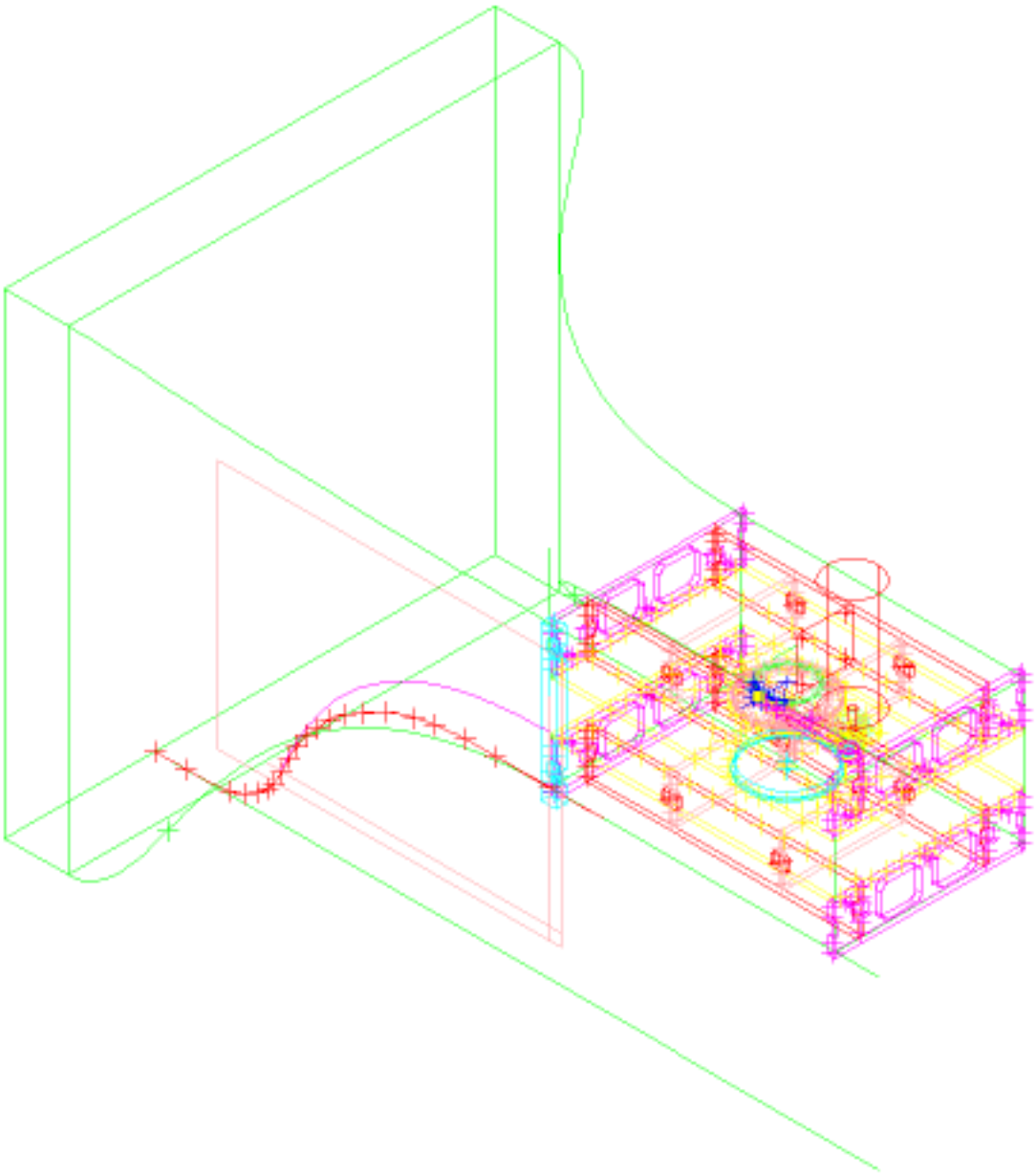

Isometric view of contraction and tunnel test section.

Appendices

Appendix O: Test Data, NASA, McAlister, NACA-0012

TABLE 19.- MISCELLANEOUS DYNAMIC DATA

Airfoil	Frame	M_∞	α_o	α_1	k	Remarks
N-0012	✓8019	0.035	10.0	10.0	0.10	Low Reynolds number, 0.5×10^6
	✓8021	.035	10.0	10.0	.15	
	✓8023	.035	10.0	10.0	.25	
	✓8104	.035	15.0	10.0	.15	
	✓8106	.035	15.0	14.0	.10	
	8116	.07	15.0	10.0	.15	Match reference 3
	8118	.07	15.0	10.0	.25	
	8123	.07	15.0	14.0	.10	Match reference 3
	8203	.07	10.0	10.0	.25	
	8210	.11	10.0	10.0	.25	
	8222	.18	15.0	10.0	.15	Match reference 3
	8306	.18	15.0	14.0	.10	Match reference 3
	9022	.18	15.0	6.0	.24	Match reference 3
	9101	.18	15.0	5.0	.29	
	9106	.18	10.0	10.0	.25	
	7108	.30	8.0	5.0	.025	Variable α_o
	7110		8.0		.10	
	7111		8.0		.20	
	7216		8.8		.05	
	7214		8.8		.10	
	7212		8.8		.15	
	7104		9.0		.025	
	7019		9.0		.05	
	7021		9.0		.10	
	7101		9.0		.15	
	7023		9.0		.20	
			10.0		See table 17	
	7117		11.0		.025	
	7118		11.0		.05	
	7119		11.0		.10	
	7120		11.0		.15	
	7121		11.0		.20	
	7200		12.0		.025	
	7202		12.0		.05	
	7205		12.0		.10	
	7305		12.0		.15	
	7207		12.0		.20	
			15.0		See table 16	
	10309		2.8	10.0	.10	
	10305		3.8			
	10303		5.0			
	9302		10.0			
	10022		12.0			
	9217	.29	15.0			
	14220	.29	15.0			
	10101	.27	20.0			
	10104	.30	12.0	8.0	.05	Match reference 17
	10105	.30	12.0	8.0	.10	Match reference 17
	10108	.30	12.0	8.0	.13	Match reference 17
	15218	.29	15.0	10.0	.10	Pressure orifices closed

38

Appendices

This table identifies parameters for the tests shown in the following pages.

SYMBOLS

c	airfoil chord, m
C_D	drag coefficient derived from surface pressures, drag/qcs
C_L	lift coefficient derived from surface pressures, lift/qcs
C_M	moment coefficient derived from surface pressures, moment/qc^2s
C_p	pressure coefficient, $(p - p_\infty)/q$
k	reduced frequency, $\omega c/2U_\infty$
M	Mach number
p	surface pressure, N/m^2
p_∞	free-stream static pressure, N/m^2
p_T	free-stream total pressure, N/m^2
q	free-stream dynamic pressure, N/m^2
Re	Reynolds number based on chord and free-stream conditions
s	airfoil span, m
t	time, sec
U_∞	free-stream velocity, m/sec
x	chordwise coordinate, m
y	normal coordinate, m
α	airfoil incidence, deg
α_o	mean angle of oscillation, deg
α_1	amplitude of oscillation, deg
ζ	aerodynamic pitch damping coefficient, $-\frac{1}{4\alpha_1^2}\oint C_M \, d\alpha$
ω	circular frequency, rad/sec

Appendices

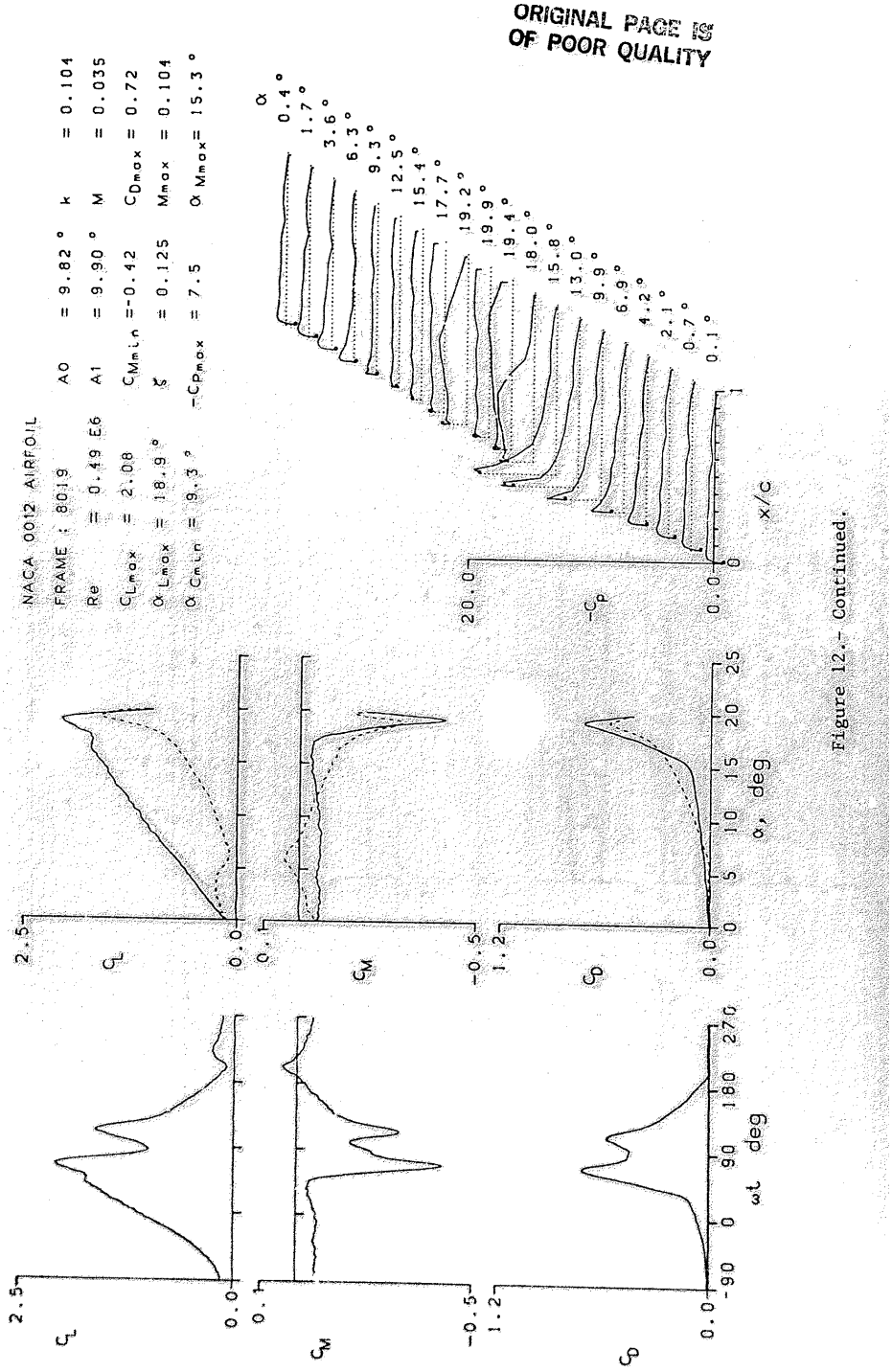

Figure 12.- Continued.

Appendices

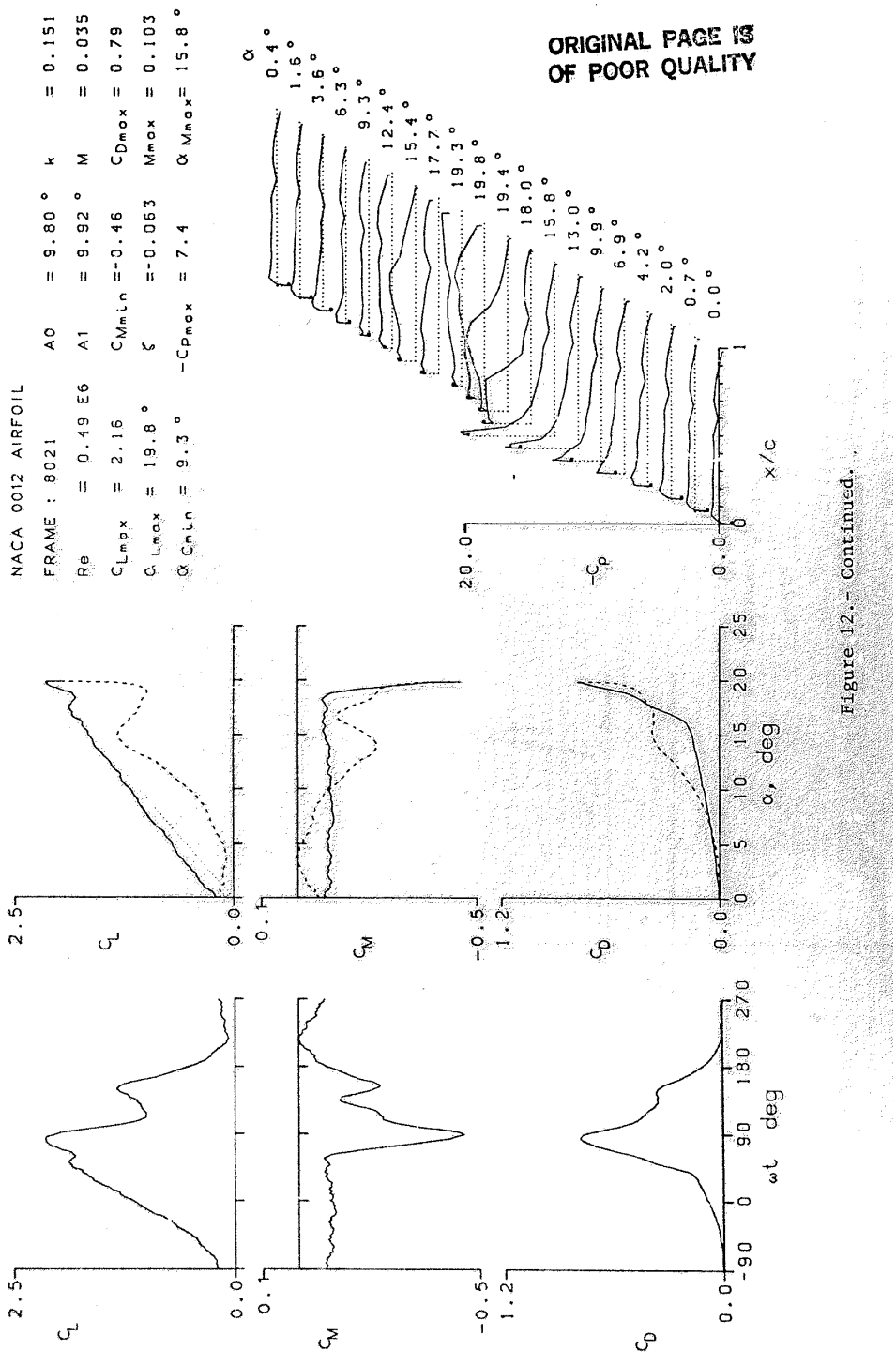

Figure 12.- Continued.

Appendices

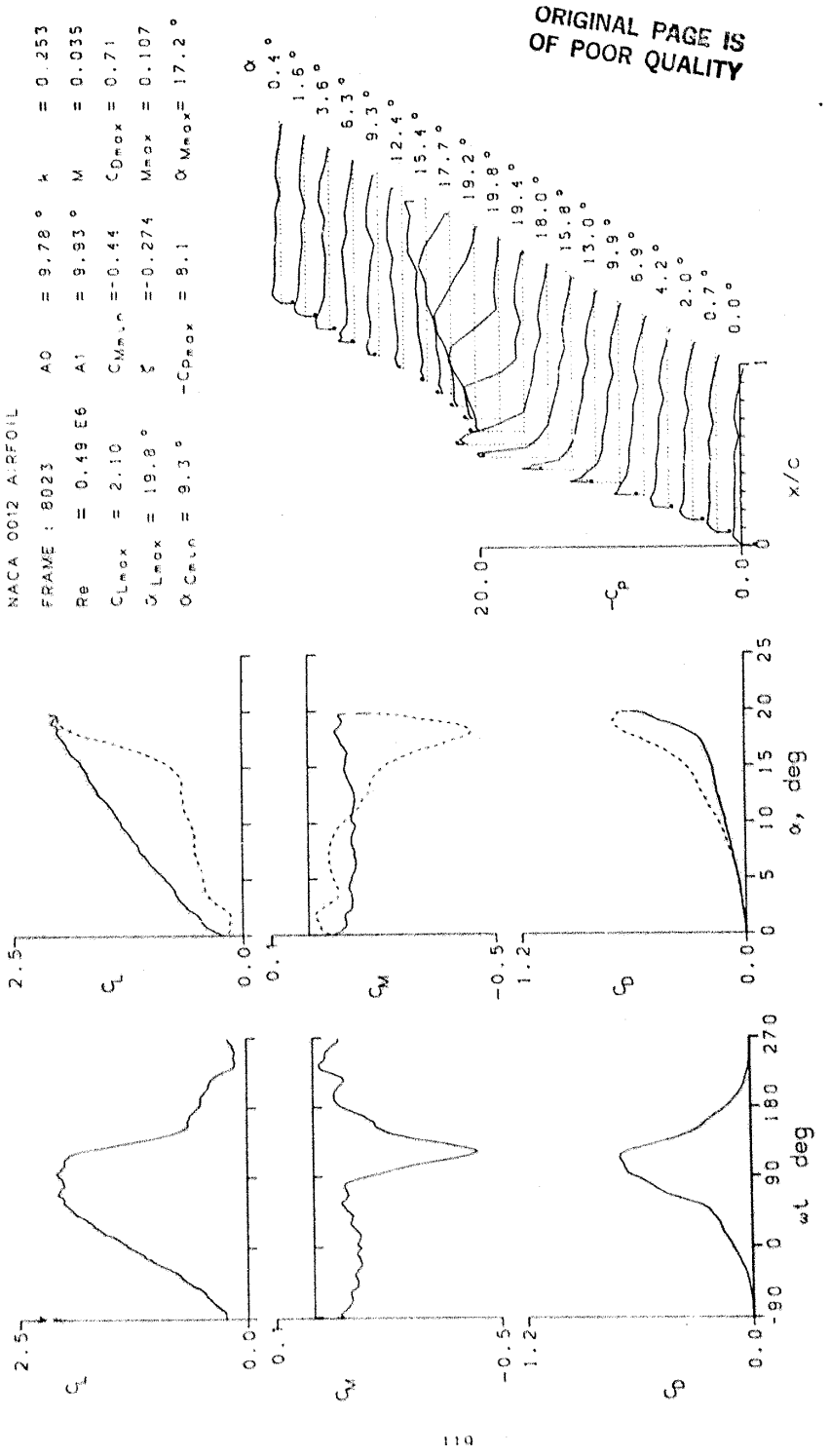

Figure 12.- Continued.

Appendices

Appendix P: Assembly and Installation Instructions

Apparatus assembly and installation instructions:

All other devices and components must be removed from the tunnel test section. A support rail is bolted to each side of the tunnel support structure. The motor drive and transmission must be removed from the insertable test section before it will fit into the tunnel. A hydraulic lift truck is used to lift the insert assembly off of its dolly and onto the support rails. Once on the support rails the insert section will slide into position in the center of the tunnel. Once in position the upper and lower contraction inserts may be installed. Remove the honeycomb frame at the contraction entrance. Remove the four screens behind the honeycomb. Set the lower contraction insert in place. Attach the leading edge of the insert with the nine 5/16” bolts, but do not tighten. Attach the trailing edge to the entrance of the test section with three ½” bolts, but do not tighten. Align the joint between the contraction insert and the entrance of the insert test section, then tighten the ½” bolts. Repeat for the upper contraction insert. Tighten the nine upper and lower bolts at the insert leading edge.

Appendices

The joints between the contraction inserts and the sides of the contraction must be sealed with non-porous tape. The seams between the contraction insert and the test section insert must be sealed with smooth thin packing tape. Screw holes in the ceiling and floor of the test section must be sealed with tape. The perimeter of the insert test section must be sealed with tape. The access holes for attaching the contraction inserts and the diffuser inserts must be sealed with a cover and taped in place.

The screens and honeycomb may be replaced at the entrance of the contraction.

The motor drive system and transmission is reassembled on the top of the test section insert.

The side windows are placed on the sides of the test section. Pitot static connections are made between the two pitot tubes. Connections between the transducer array rails and the SCXI-1100 front connector are made with standard 25 pin printer cables. The angular position potentiometer is connected to the transducer array rail with a special cable.

The host computer is attached to the SCXI-1200 module with a 25 pin printer cable.

Appendices

Power connections are made to the variable speed motor drive. The variable speed drive is electrically connected to the motor.

Connect a frequency counter to the angular position transducer output.

Connect a calibrated sensitive airspeed indicator and altimeter to the pitot static tubing.

Running the experiment:

The experiment is repeated for each of the values of free steam velocity and reduced frequency in the array shown in appendix D.

Assemble the drive transmission with the correct ratio for the rotational frequency to be tested. Adjust the crank mechanism for the desired angular movement of the window. Adjust the connecting rod, rod end, for the desired average angle

Start the host computer and start Labview. Turn on the SCXI chassis. Turn on power on each transducer array rail. Turn on power to DC motor drive.

Appendices

Start the wind tunnel main drive motor. When motor has reached operating speed, adjust the speed control damper to get the desired free stream velocity, using the calibrated sensitive airspeed indicator as a reference. Start the DC motor and adjust the rotational frequency using the frequency counter as a reference.

Select the desired rate of sampling and number of samples. Start the test. The program will place the data in a text file. Repeat the test until the required amount of data is acquired.